



Simulation Based Optimization Of Spray Absorption Process Parameters Using OpenFOAM

Thesis to get the degree of a Master of Sciences

by

Thomas Kerschl

UNIVERSITY OF APPLIED SCIENCES MUNICH
Department of Applied Sciences and Mechatronics
Laboratory for Modeling and Simulation
Study course Micro- and Nanotechnology

Examiner and Supervisor: Prof. Dr. Alfred Kersch
Second Examiner: Prof. Dr.-Ing. Datong Wu
Date of Admittance:

Munich 2016

Abstract English

Heat pumps offer a great opportunity of heating buildings on renewable energy sources. A small, cost-efficient and environment-friendly implementation are ammonia-water absorption heat pumps. One of its critical components in terms of efficiency, size and cost is the absorber. In this thesis the physical processes inside an ammonia-water spray absorber chamber were analyzed, modeled and simulated with the objective of optimizing the absorber efficiency by determining the influence of spray and nozzle properties on the absorption process. Effects of drop diameter and velocity were estimated analytically by simple approximations and by calculations in LibreOffice spreadsheets. The joint distribution of drop diameter velocity in a spray produced by a certain nozzle was modeled using both empirical equations and ab-initio methods like the maximum entropy formalism (MEF) by the current state of scientific and engineering knowledge. The model of a swirl nozzle thus obtained was implemented in C++ as a part of an OpenFOAM solver. Using an existing, specifically built absorption library, the author was provided with, several simulations were conducted varying the absorption chamber geometries and the nozzle types. The results of these simulation showed that the heat transfer from the drops to the ammonia vapor atmosphere in the absorption chamber and subsequently from the chamber atmosphere to the chamber walls is the crucial parameter determining the absorption rate and the final ammonia concentration.

In literature, several approaches can be found to determine the absorption rate of a single, representative drop in a spray, either by analytical or numerical methods. However, so far no study considered the effects of the whole spray consisting of a huge number of drops with varying size and velocity. By the model and setup developed in this work, effects like heating up of the absorber chamber or flow induced by momentum transfer from the drops to the fluid, can be taken into account for the first time.

Abstract Deutsch

Wärmepumpen bieten die Möglichkeit, Gebäude mit erneuerbaren Energien zu heizen. Als besonders platzsparend, rentable und umweltfreundlich gelten Ammoniak-Wasser Absorptionswärmepumpen. Dabei hängt der Gesamtwirkungsgrad der Wärmepumpe hauptsächlich von der Effizienz des Absorbers ab. In dieser Arbeit wurden die physikalischen Vorgänge innerhalb der Absorberkammer analysiert, modelliert und simuliert, um die jeweiligen Einflüsse des Sprühs und der Düse zu ermitteln, welche die Effizienz eines Absorbers bestimmen. Dabei wurden die Auswirkungen von Tropfendurchmesser und -geschwindigkeit zunächst durch einfache analytische Näherungen und mithilfe von LibreOffice-Tabellen abgeschätzt. Die Verteilung von Durchmesser und Geschwindigkeit der einzelnen Tropfen in einem Sprüh, der von einer bestimmten Düse erzeugt wird, wurde durch empirische Formeln und mithilfe des Maximum Entropie Formalismus (MEF) nach aktuellem Stand der Forschung ermittelt. Das so gewonnene Modell einer Wirbeldüse wurde anschließend in C++ als Teil eines OpenFOAM Solvers implementiert. Mithilfe einer vorhandenen, eigens dafür entwickelten Bibliothek zur Simulation der Wärme- und Massentransfervorgänge, wurden erste Simulationen mit verschiedenen Düsentypen und Kammergeometrien durchgeführt. Die Auswertung der Simulationsdaten hat ergeben, dass vor allem der Wärmeübergang zwischen den Tropfen und der umgebenden Ammoniakatmosphäre und zwischen Ammoniak und Kammerwand die Absorptionsrate und erreichte Konzentration bestimmen.

Obwohl sich in der Literatur einige Arbeiten finden, die mit analytischen oder numerischen Methoden die Absorptionsrate eines einzelnen, für den Sprüh repräsentativen Tropfen bestimmen, wurden bisher jedoch nie die Auswirkungen des gesamten Sprühs, der aus vielen Tropfen unterschiedlicher Größe und Geschwindigkeit besteht, auf die Absorptionsrate in der Kammer betrachtet. Mit dem hier entwickelten Modell können erstmals Effekte wie das Aufheizen der Absorptionskammer oder die Erzeugung von Strömungen durch den Impulsübertrag der Tropfen auf das umgebende Fluid in die Betrachtung miteinbezogen werden.

Contents

Nomenclature	iv
List of Figures	xii
Introduction	1
Objective and Guidelines	2
1. Heat Pumps	3
1.1. Compression Heat Pumps	4
1.2. Absorption Heat Pumps	5
1.3. COP of an Absorption Heat Pump	7
2. Ammonia Absorption	9
2.1. Mass Transfer Theories	9
2.1.1. Diffusive Mass Transfer	9
2.1.2. Film Theory	10
2.1.3. Boundary Layer Theory	11
2.1.4. Penetration Theory	11
2.1.5. Surface Renewal Theory	12
2.2. Types of Absorber	12
2.2.1. Falling Film Absorbers	12
2.2.2. Bubble Absorbers	13
2.2.3. Spray Absorbers	14
2.3. Prior Estimations of the Absorption Process	15
2.3.1. Saturation Concentration vs. Enthalpy of Solution	15
2.3.2. Estimation of Absorption Rate according to ELPERIN	17
2.3.3. Estimation of Heat Dissipation	21
2.3.4. Estimation of Absorption Rate according to FENTON	23
2.3.5. Estimation of Heat Flux through the Chamber Walls	28

2.3.6.	Conclusions on Requirements for the Spray	31
3.	Sprays	32
3.1.	Nozzle Types	32
3.1.1.	Plain Orifice Nozzles	32
3.1.2.	Twin-Fluid Nozzles	32
3.1.3.	Pressure Swirl Nozzles	33
3.2.	Mechanism of Atomization	34
3.2.1.	Atomization of a Liquid Sheet	34
3.2.2.	Satellite Droplets	37
3.3.	Mean Drop Diameters	38
3.4.	Drop Size and Velocity Distribution	39
3.4.1.	ROSIN-RAMMLER Distribution	40
3.4.2.	Maximum Entropy Formalism (MEF)	40
4.	Modeling the Nozzle	47
4.1.	About OpenFOAM	47
4.2.	Available Injection Models in OpenFOAM	47
4.3.	Required Extensions for the Injection Model	48
4.4.	Implementation in OpenFOAM	49
4.4.1.	Generating random variables with a specific probability distribution	49
4.4.2.	Creating the Parcels	50
4.5.	Parameters for the Injection Model	55
4.5.1.	Selection of Proper Nozzles	55
4.5.2.	Conversion of Manufacturer's Data to the Designed Operating Point for p and θ	56
4.5.3.	Sheet Thickness	58
4.5.4.	Sheet and Swirl velocity	58
4.5.5.	Breakup Length	58
4.5.6.	Reynolds and Weber Number	59
4.5.7.	Mean Droplet Diameter	60
4.5.8.	Source Terms for the MEF	60
4.5.9.	Lagrangian Multipliers	61
4.5.10.	Results for the Joint Diameter-Velocity Distribution	63
4.5.11.	Validation	63

5. Conduction of Simulation Experiments	64
5.1. Simulation Setup and Boundary Conditions	64
5.1.1. Dimension of Absorber Chamber	64
5.1.2. Interaction of Drops with Fluid	65
5.1.3. Cell Size	65
5.1.4. Laminar or Turbulent Flow	66
5.1.5. Boundary Conditions and Simplifications	66
5.1.6. Design of Simulation Experiments	67
5.2. Analysis and Discussion of Simulation Data	68
5.2.1. Mass Fraction of an Average Drop	68
5.2.2. Mass Fraction of an Individual Drop	69
5.2.3. Absorber Output	72
5.2.4. Lifetime and Mass Fraction of Different Drops	73
5.2.5. Fraction of Total Volume as a Function of Drop Diameter	75
5.2.6. Balance of Energy and Achievable COP	76
5.3. Conclusions	79
5.4. Open Issues	80
5.5. Outlook	81
6. Summary	82
A. Description of Class SwirlNozzleInjection	84
A.1. Differences compared to ConeNozzleInjection	84
A.2. Description of Parameters	85
A.3. C++ source code	87
A.4. Parameters for the Selected Nozzles	94
B. MEF Implementation in Sciab	96
C. Results of Simulated Scenarios	101
C.1. Scenario 1	101
C.2. Scenario 2	104
C.3. Scenario 3	107
C.4. Scenario 4	110
C.5. Scenario 5	113
Bibliography	117

Nomenclature

Roman Symbols

A Surface area [m²]

a Subscript variable

A₀ Swirl velocity [1/s]

B Substitution variable for energy source term

b Subscript variable

c Concentration [mol/m³]

c_A Concentration of species A [mol/m³]

C_d Drag coefficient

c_{p,g} Specific heat capacity of gas [J/(K kg)]

c_{p,l} Specific heat capacity of liquid [J/(K kg)]

c_p Specific heat capacity [J/(kg K)]

COP Coefficient of performance of an heat pump

D Drop diameter [m]

d Orifice diameter of the nozzle [m]

D₁₀ Average diameter of a drop [m]

D₂₀ Surface mean diameter of a drop [m]

D₃₀ Mean volume drop diameter [m]

- D_c Cut-off diameter [m]
- F Force [N]
- f Probability distribution function
- F_d Drag force [N]
- FEM Finite Element Method
- FVM Finite Volume Method
- G Fraction of total volume in Rosin-Rammler distribution
- g Gravity acceleration $g = 9.81 \text{ m/s}^2$
- h Height of absorber chamber [m]
- h Probability distribution function
- $H_{\text{sol,g}}$ Enthalpy of solution of the gas [J/mol]
- $H_{\text{vap,g}}$ Enthalpy of vaporization of the gas [J/mol]
- I Bayesian entropy [J/K]
- j Mass flow density [mol/(m² s)]
- K Parameter in Rosin-Rammler distribution [m]
- k Wavenumber [1/m]
- k_b Boltzmann constant $k_B = 1.38 \cdot 10^{-23} \frac{\text{J}}{\text{K}}$
- k_m Mass transfer coefficient [m/s]
- L Characteristic length in boundary layer theory [m]
- l Random number in Monte Carlo algorithm
- L_b breakup length (point where drops evolve from liquid sheet) [m]
- M Molar mass [kg/mol]

m Mass [kg]

M_g Molar mass of gas [kg/mol]

N Number of drops

n Molar amount of a substance [mol]

Nu Nusselt number

p Pressure [Pa]

P Power [W]

p_0 Target injection pressure [Pa]

p_{Data} Injection pressure from data sheet [Pa]

p_{ij} Discrete probability

p_{inj} Injection pressure [Pa]

P_{rad} Radiation power [W]

Pe Peclet number

Pr Prandtl number

q Exponent in Rosin-Rammler distribution

Q Heat energy [J]

Q_{AB} Absorber energy [J]

Q_{CO} Condenser energy [J]

Q_{EV} Evaporator Energy [J]

Q_{GE} Generator energy [J]

R Drop radius [m]

r Radius [m]

r_0	Orifice radius [m]
R_{th}	Thermal resistance [K/W]
Re	Reynolds number
S	Entropy [J/K]
S_0	Swirl strength [m]
S_e	Source term of energy [J]
S_{mv}	Source term of momentum [kg m /s]
S_m	Source term of mass [kg]
Sc	Schmidt number
Sh	Sherwood number
SPF	Seasonal Performance Factor of an heat pump
T	Temperature [K]
t	Time [s]
T_{AB}	Absorber temperature [K]
T_{CO}	Condenser temperature [K]
T_{EV}	Evaporator temperature [K]
T_{GE}	Generator Temperature [K]
T_{soil}	Soil temperature [K]
t_s	Sheet thickness [m]
U	Drop velocity [m/s]
U_0	Initial drop velocity [m/s]
U_1	Velocity of liquid sheet [m/s]

V	Volume [m ³]
w	Parameter for nondimensional time
W	Mechanical or electrical work [J]
We	Weber number
X	Dimensionless weight fraction of an absorbate
x	weight fraction of an absorbate [kg/kg]
x_0	Initial weight fraction [kg/kg]
X_B	dimensionless weight fraction in the bulk
x_B	Weight fraction in the bulk [kg/kg]
x_s	Weight fraction of saturated concentration [kg/kg]
x'	Equilibrium weight fraction of an absorbate [kg/kg]
y	Nozzle flow exponent
z	Displacement of the liquid sheet surface [m]
\bar{S}_e	Dimensionless source term of energy
\bar{S}_{mv}	Dimensionless source term of momentum
\bar{S}_m	Dimensionless source term of mass
\dot{m}_g	Mass flow of gas [kg/s]
\dot{m}_l	Mass flow of liquid [kg/s]
\dot{V}	Volume flow rate [m ³ /s]
\dot{V}_{Data}	Volume flow rate from data sheet [m ³ /s]
\hat{h}	Maximum value of a probability distribution function in Monte Carlo algorithm
\hat{l}	Ceiling Value in Monte Carlo algorithm

- \mathcal{A} Amplitude of the liquid sheet disturbance [m]
- \mathcal{D}_{AW} Diffusion coefficient between ammonia and water
- \mathcal{L} Lagrange function
- \bar{D} Dimensionless drop diameter
- \bar{D}_{cr} Dimensionless critical drop diameter
- \bar{U} Dimensionless drop velocity
- \vec{u}_l Velocity vector of liquid sheet
- \vec{a} Axial vector of the nozzle
- \vec{b} Vector perpendicular to orifice radial vector
- \vec{c} Vector perpendicular to orifice radial vector
- \vec{r} Orifice radial vector
- \vec{s} Position vector of a drop
- \vec{x} Random vector
- \vec{z} Orifice position
- \widehat{m} Mass all the drops impinging the absorption chamber wall within a simulation time step [kg]
- \widehat{xm} Mass of ammonia contained by all the drops impinging the absorption chamber wall within a simulation time step [kg]
- \widehat{x} Total mass fraction of ammonia in the liquid leaving the absorber within a simulation time step [kg/kg]
- \widetilde{V}_l Resulting injection flow rate for simulated nozzle [m³/s]
- f_{max} Maximum value of MEF distribution function
- P_{esc} Time derivative of accumulated heat energy of the drops escaping from the absorber [W]

U_l^* Dimensionless velocity of liquid sheet

Greek Symbols

α Position along the spray cone circle of a drop

χ Parameter in linear equation for saturation concentration [1/K]

Δ Difference

δ Layer thickness (in diffusion model) [m]

ϵ Radiation coefficient

η Thermal conductivity [W/m²]

κ Parameter in MEF (prior distribution function)

λ Length of waves on the liquid sheet [m]

λ_b Dominant wavelength on the liquid sheet [m]

λ_c Cut-off wavelength on the liquid sheet [m]

$\Lambda_{0,1,2,3}$ Lagrangian multiplier

μ_g Dynamic viscosity of gas [kg/(s m)]

ν Atomic diffusion volume [m³/mol]

ν Mean drop diameter index

Ω Number of configurations in a thermodynamic system

ω Growth rate of waves on the liquid sheet [1/s]

$\bar{\omega}$ dimensionless growth rate

Φ Heat flux through the chamber walls [W]

π Circle constant

ρ Mass density [kg/m³]

ρ_g	Mass density of gas [kg/m ³]
ρ_l	Mass density of liquid [kg/m ³]
σ	Surface tension [J/m ²]
τ	Dimensionless time
θ	Spray angle [rad]
ϱ	Ratio of gas density to liquid density
ς	Stefan-Boltzman constant $\varsigma = 5.57 \cdot 10^{-8} \frac{W}{m^2 K^4}$
ϑ	Exposition time in Penetration Theory [s]
ξ	Parameter in linear equation for saturation concentration
ζ	Constant factor in growth rate equation

List of Figures

1.1.	Compression heat pump cycle for residential heater [37]	4
1.2.	Schematic diagram of a compression cooling cycle [17]	5
1.3.	Schematic diagram of an absorption cooling cycle [17]	6
2.1.	The film theory assumes diffusion is taking place only in a thin film (of thickness δ) between two regions A and B of constant concentration c_A and c_B	11
2.2.	Falling film absorber configurations: (a) horizontal bank tube and (b) vertical tube [17]	13
2.3.	Schematics of (a) bubble absorber and (b) spray absorber [17]	14
2.4.	Saturation concentration of ammonia in water and actual concentration when solving ammonia in water starting at 300K as a function of temperature	16
2.5.	Dimensionless weight fraction X_B of an absorbate in the bulk of a drop as a function of dimensionless time τ [11]	18
2.6.	Ammonia concentration in a moving water drop as a function of time for different diameters and initial velocities (applied to the results of [11])	20
2.7.	Ammonia concentration as a function of the distance covered by a drop. 21	
2.8.	A water drop falling with initial velocity $U_0 = 23 \frac{m}{s}$ and diameter $D = 100 \mu m$ in ammonia atmosphere. The curves for temperature and ammonia concentration in the drop were calculated using the boundary layer theory like in [12] for the absorption rate and considering convective heat dissipation.	27

2.9. Set of $X(s)$ curves for different diameters and initial velocities.	27
2.10. Heat flux Φ as a function of the final drop temperature T . The thin line in red shows the linearized approximation of Φ within the range of $310 K < T < 340 K$	29
2.11. Simplified model of the absorber chamber: The source of the heat flux Φ , i.e. drops of higher temperature has the shape of a sphere of radius r_i . The chamber is also spheric with radius r_o	29
2.12. Φ and T plotted as a function of r_o , assuming $r_i = 0.2 m$	31
3.1. Schematic of a twin-fluid nozzle [4]	33
3.2. Schematic of a hollow cone nozzle (a) and a full cone nozzle (b) [4] . .	34
3.3. Schematic of (a) antisymmetric (sinuous) disturbance and (b) symmetric disturbance [4]	35
3.4. Schematic of the breakup process from a liquid sheet. The drop diameters are of the same dimension as the sheet thickness [30]	35
3.5. Simulated breakoff of a drop from the bulk. A small satellite droplet develops in the middle of the breakoff-thread [35].	37
3.6. Joint diameter-velocity distribution function calculated by the MEF for a 1-8-Ax-5-5W nozzle from Spraying Systems Co..	44
3.7. Prior distribution function f_0 according to eqn. 3.32, calculated for $We = 9.24$, $t_s = 2.93 \cdot 10^{-4} m$, $D_{30} = 5.84 \cdot 10^{-5} m$. The two regions are connected at $\bar{D}_{cr} = 0.626$ and $\kappa = 0.597$	45
4.1. Flow chart of acceptance-rejection algorithm applied to joint diameter-velocity probability distribution $f(\bar{D}, \bar{U})$	50
4.2. The initial position of the parcels representing the drops is at the breakup point, L_b away from the nozzle exit along the spray cone with spray angle θ	51
4.3. The radius vector \vec{r} can be constructed by two vectors \vec{b} and \vec{c} , perpendicular to the axial vector \vec{a} and perpendicular to each other. The radial component α of the initial position of the liquid sheet is determined by a random number $0 \leq \alpha < 2\pi$	52

4.4.	The initial velocity \vec{u}_l is the result of the velocity component in axial direction \vec{u}_{ax} and the tangential component \vec{u}_{tan} which is caused by the swirl of the liquid. (Its magnitude U_l is specified in the setup parameters).	52
4.5.	Flow chart of class “SwirlNozzleInjection”. The boxes with the red frame denote the code that is different to the standard class “ConeNozzleInjection”.	54
4.6.	Excerpt of nozzle data sheet from Spraying Systems Co.® [1]. The orange circles mark operating points close to the target value of $\dot{V}_0 = 2.448 \frac{l}{min} = 0.645 \frac{gal}{min}$	56
4.7.	Examples for the joint diameter-velocity distribution function $f(\bar{D}, \bar{U})$ calculated for three different nozzles. The mean diameter of the drops produced by the nozzles decreases from left to right, while the mean velocity increases.	63
5.1.	The minimum chamber dimensions allow the drops to move distance s in which they absorb most of the ammonia	64
5.2.	Mesh for an absorption chamber of $r = 0.28 m$ and $h = 0.12 m$	66
5.3.	Ammonia concentration of all drops as a function of their distance from the nozzle, evaluated at different times.	68
5.4.	Visualization of scenario 1 after 8 seconds. The spheres represent the drops, their color indicates the ammonia concentration (blue = low concentration, red = high concentration).	69
5.5.	Drops from scenario 2 of diameter $D \approx D_{30} = 84.5 \mu m$. The top graph shows the development of temperature and ammonia mass fraction of a drop generated at the beginning of the simulation, the bottom graph shows the same for a drop generated 20 seconds later.	70
5.6.	Drop from scenario 2, calculated on the model from sec. 2.3.2	71
5.7.	Drop from scenario 2, calculated on the model from sec. 2.3.4	72
5.8.	Scenario 2: Average ammonia concentration and average temperature of all impinging drops, average chamber temperature as a function of time.	73

5.9. Scenario 4: Average lifetime of drops as a function of their diameter	74
5.10. Scenario 4: Ammonia mass fraction as a function of distance from the nozzle and of drop diameter $x(D, s)$	75
5.11. Scenario 4: Red: Fraction of total volume formed by drops of diameter smaller than $\bar{D} = \frac{D}{D_{30}}$. Blue: Ammonia mass fraction of amount of liquid formed by drops of diameter smaller than \bar{D}	76
5.12. Scenario 1: Heat power of all drops escaping from the absorber chamber P_{esc}	77
5.13. Scenario 1: Heat power of all drops escaping from the absorber chamber P_{esc} and power produced by absorption P_{abs}	78
5.14. Scenario 1: Heat flux through absorber chamber walls	79
A.1. The class <i>SwirlNozzleInjection</i> -highlighted in blue- inserted in the modified UML diagram of <i>KinematicCloud</i> [29].	84
C.1. Scenario 1: Ammonia concentration and drop temperature for three individual drops at the beginning of the simulation (left column) and at the end (right column), plotted against time (upper row) and distance (lower row).	101
C.2. Scenario 1: Ammonia concentration of all drops as a function of their distance from the nozzle, evaluated at different times.	102
C.3. Scenario 1: Average ammonia concentration and average temperature of all impinging drops, average chamber temperature as a function of time.	102
C.4. Scenario 1: Average lifetime of drops as a function of their diameter.	103
C.5. Scenario 1: Ammonia mass fraction as a function of distance from the nozzle and of drop diameter $x(D, s)$	103
C.6. Scenario 1: Red: Fraction of total volume formed by drops of diameter smaller than $\bar{D} = \frac{D}{D_{30}}$. Blue: Ammonia mass fraction of amount of liquid formed by drops of diameter smaller than \bar{D}	104

C.7. Scenario 2: Ammonia concentration and drop temperature for three individual drops at the beginning of the simulation (left column) and at the end (right column), plotted against time (upper row) and distance (lower row).	104
C.8. Scenario 2: Ammonia concentration of all drops as a function of their distance from the nozzle, evaluated at different times.	105
C.9. Scenario 2: Average ammonia concentration and average temperature of all impinging drops, average chamber temperature as a function of time.	105
C.10.Scenario 2: Average lifetime of drops as a function of their diameter. .	106
C.11.Scenario 2: Ammonia mass fraction as a function of distance from the nozzle and of drop diameter $x(D, s)$	106
C.12.Scenario 2: Red: Fraction of total volume formed by drops of diameter smaller than $\bar{D} = \frac{D}{D_{30}}$. Blue: Ammonia mass fraction of amount of liquid formed by drops of diameter smaller than \bar{D}	107
C.13.Scenario 3: Ammonia concentration and drop temperature for three individual drops at the beginning of the simulation (left column) and at the end (right column), plotted against time (upper row) and distance (lower row).	107
C.14.Scenario 3: Ammonia concentration of all drops as a function of their distance from the nozzle, evaluated at different times.	108
C.15.Scenario 3: Average ammonia concentration and average temperature of all impinging drops, average chamber temperature as a function of time.	108
C.16.Scenario 3: Average lifetime of drops as a function of their diameter. .	109
C.17.Scenario 3: Ammonia mass fraction as a function of distance from the nozzle and of drop diameter $x(D, s)$	109
C.18.Scenario 3: Red: Fraction of total volume formed by drops of diameter smaller than $\bar{D} = \frac{D}{D_{30}}$. Blue: Ammonia mass fraction of amount of liquid formed by drops of diameter smaller than \bar{D}	110

C.19.Scenario 4: Ammonia concentration and drop temperature for three individual drops at the beginning of the simulation (left column) and at the end (right column), plotted against time (upper row) and distance (lower row).	110
C.20.Scenario 4: Ammonia concentration of all drops as a function of their distance from the nozzle, evaluated at different times.	111
C.21.Scenario 4: Average ammonia concentration and average temperature of all impinging drops, average chamber temperature as a function of time.	111
C.22.Scenario 4: Average lifetime of drops as a function of their diameter.	112
C.23.Scenario 4: Ammonia mass fraction as a function of distance from the nozzle and of drop diameter $x(D, s)$	112
C.24.Scenario 4: Red: Fraction of total volume formed by drops of diameter smaller than $\bar{D} = \frac{D}{D_{30}}$. Blue: Ammonia mass fraction of amount of liquid formed by drops of diameter smaller than \bar{D}	113
C.25.Scenario 5: Ammonia concentration and drop temperature for three individual drops at the beginning of the simulation (left column) and at the end (right column), plotted against time (upper row) and distance (lower row).	113
C.26.Scenario 5: Ammonia concentration of all drops as a function of their distance from the nozzle, evaluated at different times.	114
C.27.Scenario 5: Average ammonia concentration and average temperature of all impinging drops, average chamber temperature as a function of time.	114
C.28.Scenario 5: Average lifetime of drops as a function of their diameter.	115
C.29.Scenario 5: Ammonia mass fraction as a function of distance from the nozzle and of drop diameter $x(D, s)$	115
C.30.Scenario 5: Red: Fraction of total volume formed by drops of diameter smaller than $\bar{D} = \frac{D}{D_{30}}$. Blue: Ammonia mass fraction of amount of liquid formed by drops of diameter smaller than \bar{D}	116

Introduction

Decreasing reserves of fossil fuels, rising costs for heating buildings and the negative effects of greenhouse gases have turned renewable energy sources and the efficient use of energy into important topics. In Germany, according to the law for renewable energy [13], since 2008 a certain part of the overall energy requirement of new buildings must be covered by renewable energy sources. Therefore, providing private households with ecological, efficient, affordable and reliable energy supply systems became a big task for industry.

The extraction of heat from the surrounding air, soil or ground water by heat pumps offers the use of an energy source independent to the widely-used solar energy. Because of that independence, the combination of both energy sources seems obvious. Absorption heat pumps seem a good choice for that, as their components are quite simple and cheap. The usual implementation of the absorber are bubble- and falling-film-absorbers. A disadvantage is the large amount of space required for the absorber, which is needed to achieve a proper efficiency. Although a spray absorbers requires less space, the efficiency of its current implementations is quite low. Limiting factor is the heating up of the drops during absorption due to the enthalpy of solution (energy that is released when a gas dissolves in a liquid solvent).

The absorption process and its effect on a residential heat pump's efficiency was simulated and analyzed in the diploma thesis of SYLVIA PORRAS-SEYLER [32]. The types of absorbers considered were bubble- and falling-film-absorber, while spray absorbers were left out as their efficiency was assumed low compared to the other absorber types.

However, considering the high surface-volume ratio which can be achieved by a spray, it seems worthwhile to figure out the root causes for this low efficiency and find a remedy for those.

Objective and Guidelines

The main purpose of the study carried out in this thesis was to develop, setup and evaluate a simulation environment in OpenFOAM that allows the simulation and optimization of an ammonia-water spray absorber with regard to achievable ammonia concentration and efficiency. For this, the crucial parameters impacting the efficiency of a spray absorber for residential ammonia-water-heat pumps as considered in [32] had to be identified. To be able to determine the absorption capability in different configurations by simulating the processes in the absorption chamber in OpenFOAM, a proper model for spray nozzles reproducing all necessary properties of the spray had to be developed. For heat and mass transfer a given model, arising from a PhD thesis, had to be used and evaluated.

To be able to compare results from this simulation setup with [32], the following parameters were considered fixed:

1. The volume flow rate of the liquid absorbent (i.e. water) $\dot{V} = 4.067 \cdot 10^{-5} \frac{m^3}{s}$
2. The temperature of the absorbent (water) and the absorbate (ammonia vapor) when entering the absorber $T_0 = 300 K$
3. The temperature of the absorber chamber's walls $T_{walls} = 300 K$
4. The pressure of the ammonia atmosphere in the chamber $p = 2 \cdot 10^5 Pa$
5. The pressure of the liquid being injected through the nozzle $p_{inj} < 2 \cdot 10^6 Pa$

1. Heat Pumps

A heat pump is a thermal engine that moves heat energy, oppositely to the direction of spontaneous heat flow, from a cold heat source to a warmer heat sink [14]. To accomplish the work of transferring energy from the heat source to the heat sink, the heat pump consumes external power, usually electrical power. The efficiency of the heat pump is described in the Coefficient of Performance (*COP*)[17]:

$$COP = \frac{Q}{W} \tag{1.1}$$

where Q is the heat supplied to the sink or removed from the source and W is the work consumed by the heat pump. Mostly, heat pumps are used in refrigerating machines where the the system is used to draw heat energy from the surrounding gas or liquid and to cool it down thereby. In those applications, the important parameter is the transferred heat energy Q , so even a $COP < 1$ may be acceptable in some cases. However, if the heat pump is used as a heater, the COP must be higher than unity, otherwise it would be more efficient to run an electrical heater by the external power W .

Furthermore, original costs, costs of operation and space required for a heat pump system often make the conventional central-boiler heating the more economic solution [37]. The major part of the costs of operation is made up by electrical energy consumed by the heat pump. The ratio of electrical energy consumed by the heat pump to the amount of heat energy produced by the heat pump within a year is defined in the Seasonal Performance Factor (*SPF*):

$$SPF = \frac{\int^{year} \dot{Q} dt}{\int^{year} P_{el} dt} \tag{1.2}$$

This is the final number that determines if installing a heat pump system is economically reasonable in a particular case, but it depends not only on the efficiency of the heat pump, but also on the constructional situation of the building, the dimensioning

of the system, etc.

Considering all stages of energy loss at a residential heat pump system, WATTER [37] postulates $SPF \geq 3$ for economical operation.

1.1. Compression Heat Pumps

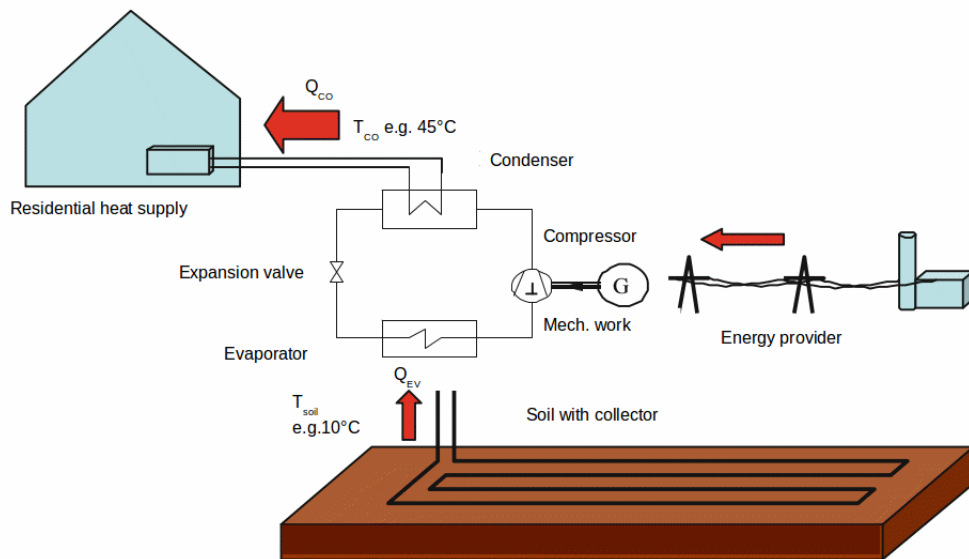


Fig. 1.1.: *Compression heat pump cycle for residential heater [37]*

Most heat pumps in use are compression heat pumps. Fig. 1.1 shows a schematic of a compressor heat pump cycle used for residential heat supply [37]. Here, the heat source is the soil of a plot with a temperature T_{soil} of 10°C . From this source, heat energy Q_{EV} is consumed to vaporize the liquid cooling agent, called “refrigerant”. Subsequently in the compressor, the refrigerant vapor is compressed by mechanical work. This increases the temperature ($T_{CO} = 45^{\circ}\text{C}$) and pressure of the refrigerant. By cooling down the refrigerant in the residential heater system, heat energy Q_{CO} is released from the heat pump cycle. Next the refrigerant is expanded while flowing through the throttle valve. By this the refrigerant vaporizes and cools down in the evaporator. The changes in pressure and temperature of the refrigerant are shown in Fig. 1.2. The cold refrigerant warms up in the evaporator from T_{EV} to T_{soil} . In the compression pump, both pressure and temperature are raised, so the refrigerant enters the condenser with high pressure and high temperature. While Q_{CO} is drawn

by the heater system, the temperature drops down. Finally at the expansion valve, both pressure and temperature decrease.

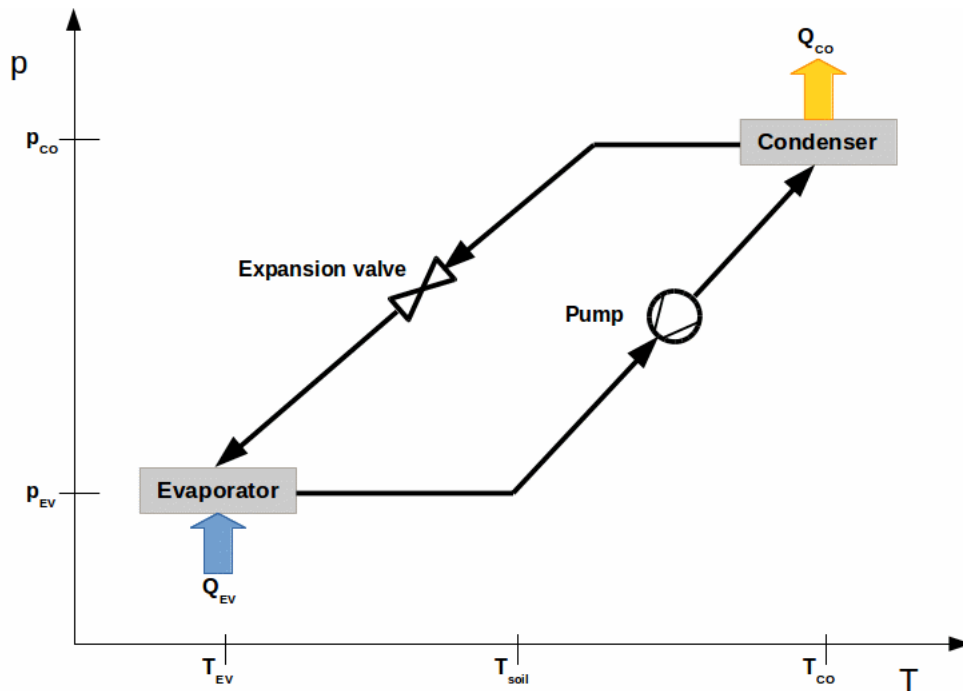


Fig. 1.2.: Schematic diagram of a compression cooling cycle [17]

1.2. Absorption Heat Pumps

The physical principle of an absorption heat pump is usually illustrated like in Fig. 1.3 by the P-T-diagram of the absorption cooling cycle. Like in compressor heat pumps, heat is removed from the surrounding area and transferred to a vaporized refrigerant.

The elements left-hand-side of the absorption cooling system (condenser, expansion valve and evaporator) are the same as for the compressor heat pump. But on the right-hand-side, instead of the compressor, there are absorber, generator and economizer [17].

In the evaporator the working fluid evaporates at a reduced pressure and temperature while taking heat from environment (Q_{EV}). Next in the absorber, this working fluid vapor is absorbed at low pressure into the concentrated absorber solution. A

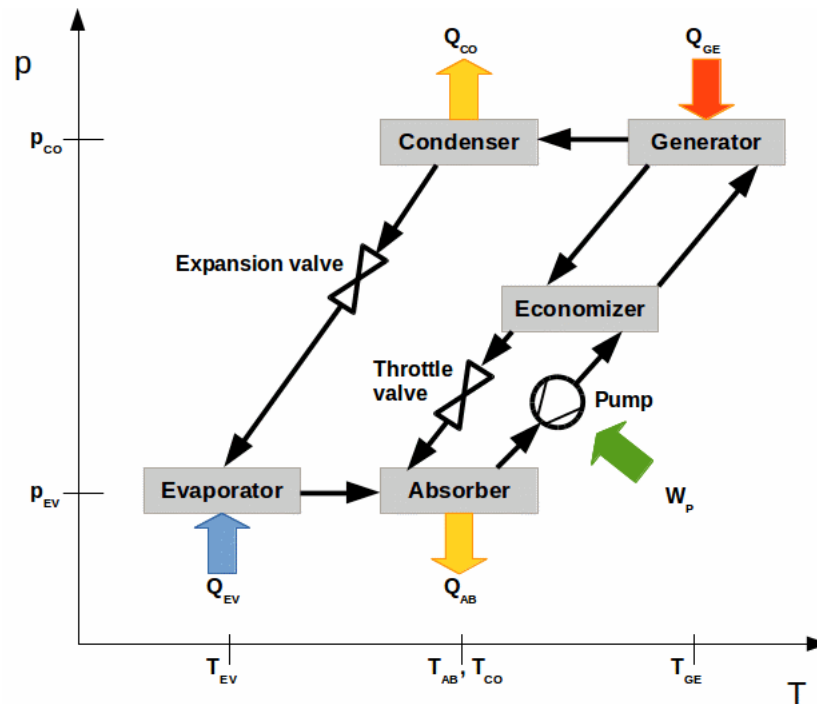


Fig. 1.3.: Schematic diagram of an absorption cooling cycle [17]

quantity of heat (Q_{AB}), originating from the enthalpy of solution is released when the refrigerant vapor is absorbed. This heat must be removed by some cooling fluid from the absorber. In the following energy recovery device called “economizer”, the diluted absorber solution is preheated by the concentrated absorber solution. In the next stage, the generator, a part of the working fluid is vaporized from the diluted absorber solution. By addition of a quantity of heat (Q_{GE}) temperature and pressure are raised¹. In the condenser, heat (Q_{GE}) is removed and the working fluid vapor condenses. The working fluid liquid is then returned to the evaporator through the expansion valve. Then the absorption cycle repeats from the evaporator.

Presently, the *COP* of absorption heat pumps is smaller than that of compression heat pumps. However, as no compressor is needed, absorption heat pumps can be built smaller and cheaper, which could make them an interesting solution for private households. With a higher *COP*, an absorption heat pump would even become financially attractive.

Second Law thermodynamic analysis shows that the highest energy loss occurs in

¹This heat energy can be produced by an electrical heater or -more efficiently- by a direct gas fired heater.

the absorber [17], due to the temperature difference between the absorber and the surroundings, so the absorber is the critical component in optimizing the *COP* of the heat pump.

1.3. COP of an Absorption Heat Pump

The COP is defined in eqn. 1.1 as the ratio of the energy released by the heat pump to the energy consumed by it. The individual parts of energy can be seen in Fig. 1.3.

$$COP = \frac{-[Q_{CO} + Q_{AB}]}{Q_{GE} + W_P} \quad (1.3)$$

The heat energy from the environment Q_{EV} does not appear in above equation as this a cost-free energy source. Instead, the energy consumed by the pump W_P shows up in the denominator. Assuming input conditions from [32], the individual terms can be estimated.

The heat flow \dot{Q}_{CO} from the condenser consists of the condensation heat (which is equal to the enthalpy of vaporization) and the loss of temperature of the gas:

$$\dot{Q}_{CO} = - \left[\frac{\dot{m}_g}{M_g} \Delta H_{vap,g} + (T_{GE} - T_{CO}) c_{p,g} \dot{m}_g \right] \quad (1.4)$$

where \dot{m}_g denotes the mass flow rate of the gas, M_g its molar mass, $c_{p,g}$ its specific heat capacity and $\Delta H_{vap,g}$ the specific enthalpy of vaporization.

The absorber power \dot{Q}_{AB} ² arises from the enthalpy of solution $\Delta H_{sol,g}$.

$$\dot{Q}_{AB} = - \left[\frac{x}{1-x} \frac{\dot{m}_l}{M_g} \Delta H_{sol,g} + (T_{AB} - T_{EV}) [(1-x) c_{p,l} + x c_{p,g}] (\dot{m}_l + \dot{m}_g) \right] \quad (1.5)$$

where x is the mass fraction of the gas solved in the liquid.

In the generator, the gas is dissolved from the liquid by heating it up to a certain

²Assuming no gas being solved in the liquid solvent before entering the the absorber.

temperature. The power \dot{Q}_{GE} ³ required for this is

$$\dot{Q}_{GE} = (T_{GE} - T_{AB}) [(1 - x) c_{p,l} + x c_{p,g}] (\dot{m}_l + \dot{m}_g) \quad (1.6)$$

³In a real system, not all of the heat produced by the generator is transferred to the liquid in the heat pump. PORRAS-SEYLER [32] estimates the generator's waste heat about 13% of the useful heat.

2. Ammonia Absorption

“Gas absorption is a unit operation in which soluble components of a gas mixture are dissolved in a liquid” [31].

Ammonia and water are highly polar substances with the ability to form hydrogen bonding. In aqueous solution, ammonia deprotonates a small fraction of the water to give ammonium and hydroxide according to the following equilibrium [21]:



The solubility of ammonia depends on the temperature of the water and decreases with rising temperature. On the other hand, the water-ammonia solution is heated up by the enthalpy of solution.

For the characterization of ammonia absorption several models can be found in literature.

2.1. Mass Transfer Theories

2.1.1. Diffusive Mass Transfer

Diffusion is the movement of a substance from a region of high concentration to a region of low concentration driven by the the concentration gradient. As described in Fick’s law the mass flow density $j \left[\frac{mol}{m^2s} \right]$ is proportional to the diffusion coefficient

\mathcal{D}_{AB} $\left[\frac{m^2}{s}\right]$ ¹ and the concentration gradient in x-direction [6]

$$j = -\mathcal{D}_{AB} \frac{dc_A}{dx} \quad (2.2)$$

The mass flow density between two regions of a known concentration difference Δc_A can be characterized by the mass transfer coefficient k_m

$$j = k_m \Delta c_A \quad (2.3)$$

There are several methods to calculate the mass transfer coefficient k_m . Depending on the materials and the system, or environment being studied, the proper theory to determine k_m must be chosen. An overview of the three major theories is given in the following subsections.

2.1.2. Film Theory

In this model diffusion is considered only in a thin layer of thickness δ between two regions of constant concentration of a certain substance (Fig. 2.1). The film theory assumes a constant concentration gradient along this layer, the mass transfer coefficient is

$$k_m = -\frac{\mathcal{D}_{AB}}{\delta} \quad (2.4)$$

¹ \mathcal{D}_{AB} is usually determined for either diffusion in liquid or in gaseous phase. For diffusion between different phases, it depends on the theory and the particular case which \mathcal{D}_{AB} matches better, i.e. if the resistance for diffusion is mainly made by the liquid or the gaseous phase.

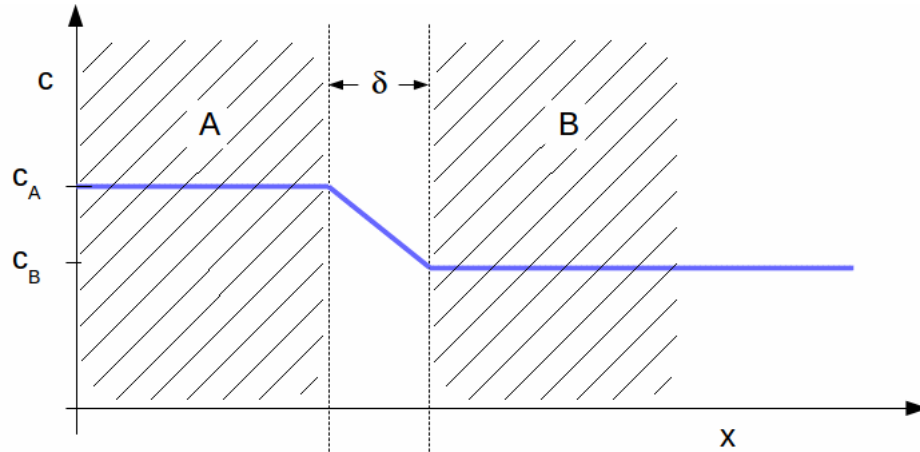


Fig. 2.1.: *The film theory assumes diffusion is taking place only in a thin film (of thickness δ) between two regions A and B of constant concentration c_A and c_B .*

2.1.3. Boundary Layer Theory

The process of diffusion produces depletion of a species on the high-concentration-edge of the diffusion film and accumulation on the low-concentration-edge. This would reduce the concentration gradient and hence the mass transfer flow. This effect can be counterbalanced by convective flow along the boundary of the two regions. By this, the mass transfer coefficient k_m is increased by a certain factor, the Sherwood number Sh (which will be explained later in sec. 2.3.4):

$$k_m = -\frac{\mathcal{D}_{AB}Sh}{L} \quad (2.5)$$

Here, the diffusion coefficient is related to a characteristic length L instead of the layer thickness. For a sphere (e.g. a drop) L is equal to the drop's diameter.

2.1.4. Penetration Theory

The penetration theory [25, 6], originally developed by Higbie 1935 for rising steam bubbles in liquids, assumes that each liquid element at the gas-liquid interface is exposed to the gas for the same time period ϑ , the so-called contact time. ϑ can be considered as the time in which a steam bubble moves at its own diameter.

Mass transfer from the gas into a liquid element occurs under unsteady-stated conditions once they are in contact, while equilibrium exists at the gas-liquid interface. The penetration theory expresses the liquid-side mass transfer coefficient k_m in terms of the contact time ϑ and the molecular diffusivity \mathcal{D}_{AB} of the gas in the liquid:

$$k_m = 2\sqrt{\frac{\mathcal{D}_{AB}}{\pi\vartheta}} \quad (2.6)$$

2.1.5. Surface Renewal Theory

Applying the mathematics of the penetration theory, the surface renewal theory [25, 6] no longer assumes the same fixed contact time between the two phases for all liquid elements. Instead, it assumes the liquid elements on the surface of the drop being randomly swapped by fresh elements from the bulk so the contact time has to be described by a distribution function.

Although the surface renewal theory provides a very exact description of mass transfer processes, it is not applicable if the contact time distribution function is not known (which is the case quite often). Therefore, the penetration theory is “most frequently used for predicting gas absorption rates” [19].

Here, for simple prior estimations of the absorption rate, the boundary layer theory was chosen, because it can easily be implemented in a spreadsheet and because the drop diameters considered in this work are small enough that an equilibrium state in temperature and concentration is reached almost instantaneously.

2.2. Types of Absorber

2.2.1. Falling Film Absorbers

Most of the absorber units in commercial cooling absorption machines are falling film absorbers. In this process, the liquid absorbent is guided along a cooled surface forming a thin film which is exposed to the gaseous absorbate. There are two different falling film absorber configurations as shown in Fig. 2.2 a) and b):

In the horizontal bank tube, the liquid flows vertically along a set of horizontal tubes. Thereby an increased surface is exposed to the gas which raises the absorption rate.

Also, the large surface of the cooled tubes wetted by the liquid supports the transfer of the heat arising from the enthalpy of solution. This prevents a limitation of absorption due to reduced gas solubility of the heated absorbent. However, this configuration requires a larger absorber chamber than other methods. Furthermore, the wettability of the tubes is largely influenced by liquid properties and operating conditions which makes it difficult to maintain a stable performance.

In the vertical tube falling film absorber, the gas flows through a cylindrical chamber whose inner face is wetted by the absorber fluid, which slowly descends downward while it absorbs the gas. The outer face is cooled. This concept is much simpler and more robust than the horizontal bank tube but less efficient due to the smaller surface area of the liquid.

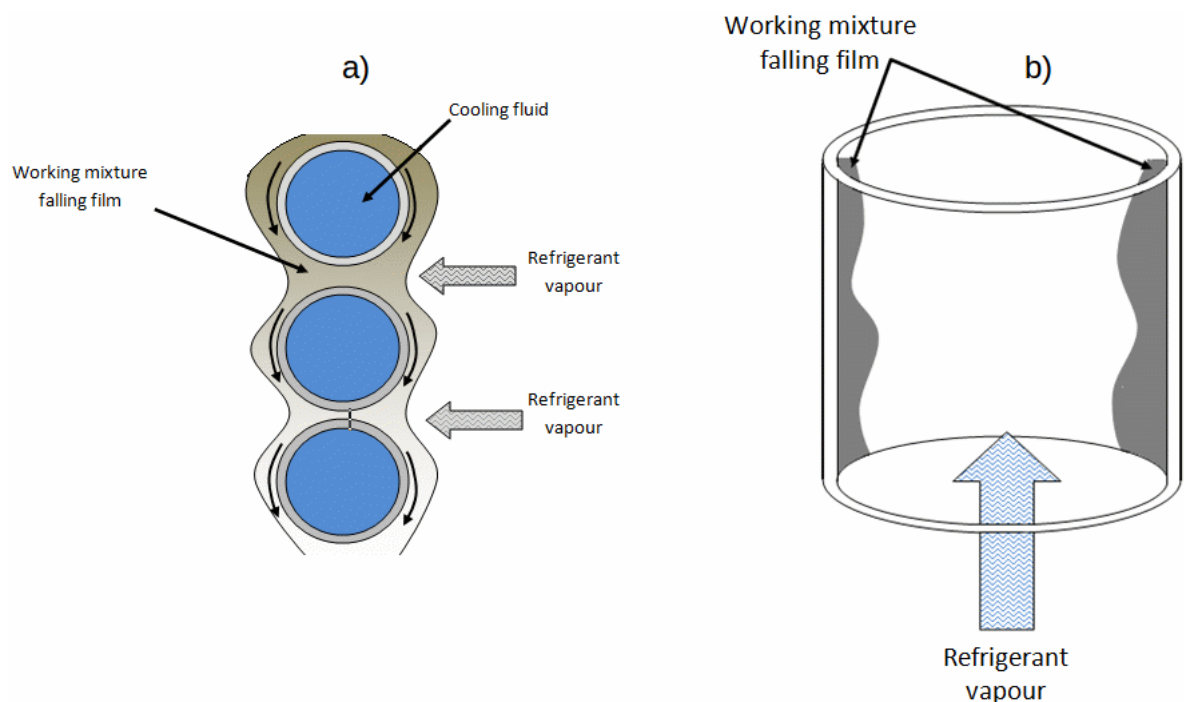


Fig. 2.2.: *Falling film absorber configurations: (a) horizontal bank tube and (b) vertical tube [17]*

2.2.2. Bubble Absorbers

In a bubble absorber, the liquid absorbent flows through a vertical cylinder while the gaseous absorbate is injected into the liquid. Forming bubbles, the gas ascends in the liquid and a part of it is being absorbed at the bubble-liquid interface. The liquid can

be cooled from the outer surface of the cylinder. At low capacity absorbers with low solution flow rates, bubble absorption is more efficient than falling film absorption due to the low wetted area in falling film flow under such regimes. Fig. 2.3 a) shows the bubble absorber configuration.

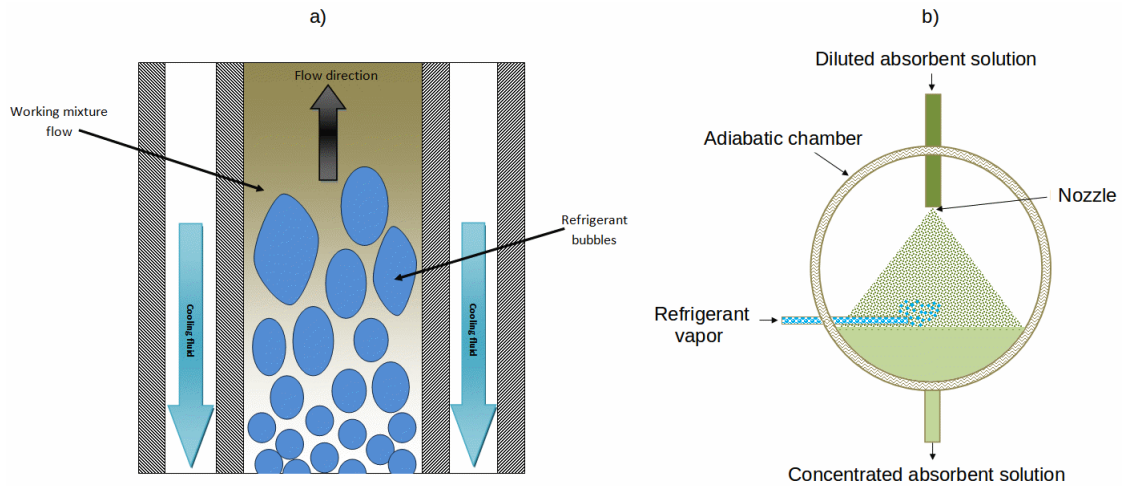


Fig. 2.3.: Schematics of (a) bubble absorber and (b) spray absorber [17]

2.2.3. Spray Absorbers

In spray absorption, the liquid absorbent is injected through an atomizer nozzle into a chamber containing the gaseous absorbate as shown in Fig. 2.3 b). The developing drops form the highest surface-to-volume ratio for the liquid which leads to a high initial absorption rate. However, there is no way to discharge the heat from the drops², so the absorption process soon decays. This means that absorption occurs in a very short time only, and that the distance the drops travel until reaching their saturation concentration is very short. This distance determines the (quite small) size of the absorber chamber. Although the efficiency of a spray absorber is lower than that of the other methods, the simplicity and the low cost of the absorption chamber reduces the total costs of the machine significantly.

²Except for conductive and convective heat conduction through the absorbate atmosphere. The remaining heat is to be transferred subsequently into an external heat exchanger.

2.3. Prior Estimations of the Absorption Process

Whenever a (physical) process is simulated, only the properties of the system that matter (or at least are assumed to become important) for this distinct process will be modeled. Considering additional physical interaction outside the focus of the simulation would only cost computing capacity. Furthermore, in order to define the range of the simulation in space and time, it is necessary to get an idea about the magnitudes of the relevant physical quantities. Therefore it is important before modeling the spray, to determine which of its properties are relevant for ammonia absorption, and how the system will develop in time and temperature.

Another, obvious reason for preceding estimations of the simulation results, is to counter-check simulation results. Wrong setup, incorrect models or even non-converging sequences in the simulation program can often only be identified if the magnitude of the resulting values is known.

So the first question in practice is: What is the maximum ammonia concentration that can be achieved by pure adiabatic absorption in water spray?

2.3.1. Saturation Concentration vs. Enthalpy of Solution

When a gas dissolves in a liquid solvent, energy is released. This energy is called enthalpy of solution and heats up the solvent. For ammonia dissolving in water at 25°C, the enthalpy of solution is given by [16]: $\Delta H_{sol,NH_3|25^\circ C} = -30.50 \cdot 10^3 \frac{J}{mol}$. To raise the concentration of ammonia in a drop of water by 1 % $\frac{kg}{kg}$, the temperature of the drop will rise by

$$\Delta T_{1\% \frac{kg}{kg}} = -\frac{\Delta H_{sol,NH_3|25^\circ C}}{100 \cdot M_{NH_3} c_{P,H_2O}} = 4.29 K \quad (2.7)$$

where $M_{NH_3} = 17.013 \cdot 10^{-3} \frac{kg}{mol}$ is the molar mass of ammonia and $c_{P,H_2O} = 4.180 \frac{J}{g \cdot K}$ is the specific heat of water (values from [16]). On the other hand, the saturation concentration of ammonia depends on the temperature of the water, as listed in Tab. 2.1. In Fig. 2.4 the values for saturation concentration in $[\frac{g}{ml}]$ were approximately set equal to concentrations in $[\frac{kg}{kg}]$ and a line was fitted through these

points³. So the saturation concentration can be denoted as

$$x_s = \chi T_0 + \xi \quad (2.8)$$

where $\chi = -5.8 \cdot 10^{-3} \frac{1}{K}$ and $\xi = 2.0575$. The other line represents the rise of temperature as an effect of the enthalpy of solution when solving ammonia in water⁴. This line starts at ambient temperature (300 K) with a slope of $\frac{1}{4.29} \frac{1}{K}$. Both lines cut at about 338 K and $0.09 \frac{kg}{kg}$. This seems to be the maximum concentration that can be achieved

$T [^{\circ}C]$	saturation concentration $[\frac{g}{ml}]$
0	0.47
15	0.38
20	0.34
30	0.28
50	0.18

Tab. 2.1.: Saturation concentration of ammonia in water depending on the temperature of the water [3]

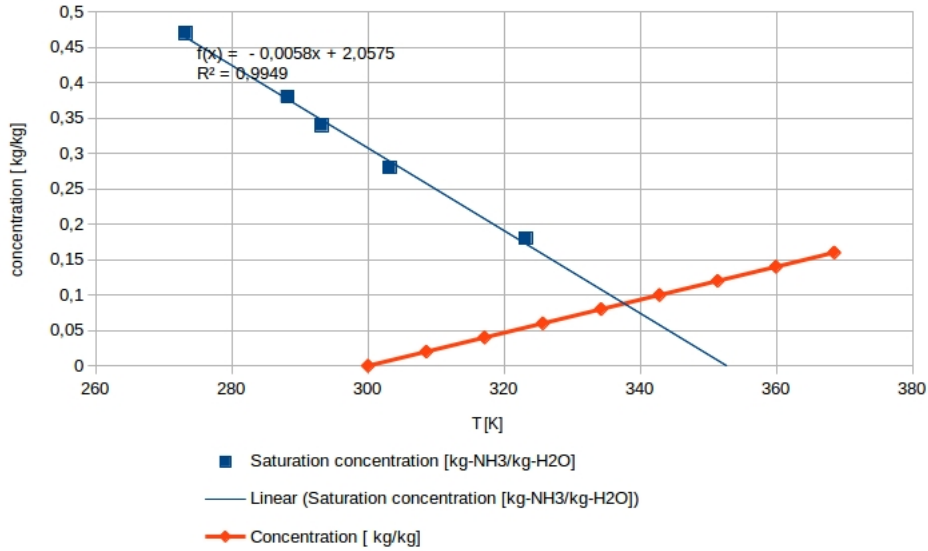


Fig. 2.4.: Saturation concentration of ammonia in water and actual concentration when solving ammonia in water starting at 300K as a function of temperature

³Here, for convenience, ΔH_{sol} was assumed constant over the whole temperature range. Later, in the OpenFOAM simulation its temperature dependency is being considered.

⁴Assuming no thermal energy dissipation from the drop

2.3.2. Estimation of Absorption Rate according to Elperin

In his study [11] ELPERIN deduces the temporal development of the concentration of gases in water being absorbed by a falling drop based on the penetration theory. He considers both flow processes inside the drop stimulated by the drag forces and thermal effects. One of the results of his study is the development of the mass fraction X_B of certain gases solved in water drops as a function of a dimensionless time τ as shown in Fig. 2.5. In this graph, the mass concentration X_B is scaled by the equilibrium weight fraction of ammonia (curve 6) at the initial temperature as a function of a dimensionless time $\tau = t \frac{wU}{R}$ ⁵ where U is the velocity of the drop, R is its radius and w a constant factor set equal to $w = 0.04$. X_B is defined as

$$X_B = \frac{x_B - x_0}{x_s - x_0} \quad (2.9)$$

where x_0 is the initial weight fraction and $x_s = \chi T_0 + \xi$ denotes the equilibrium weight fraction of an absorbate at the initial temperature T_0 , which is the saturation concentration as listed in Tab. 2.1.

⁵Elperin calculated these curves for a Peclet number for diffusion of $Pe_D = \frac{krU}{D_{dif}} = 10^5$, where \mathcal{D} is the molecular diffusion coefficient in a liquid phase (for ammonia in water $\mathcal{D} = 1.64 \cdot 10^{-9} \frac{m^2}{s}$). For our application where $35 \mu m \leq r \leq 100 \mu m$ and $1 \frac{m}{s} \leq U \leq 30 \frac{m}{s}$, the Peclet number is found in the range of $854 \leq Pe_D \leq 73171$.

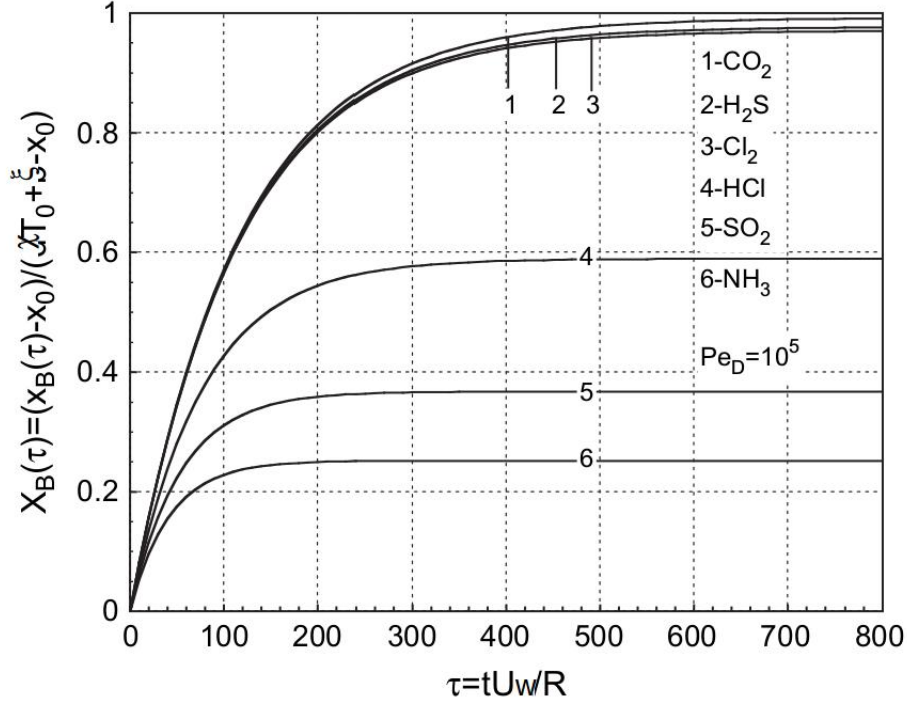


Fig. 2.5.: Dimensionless weight fraction X_B of an absorbate in the bulk of a drop as a function of dimensionless time τ [11]

The parameters χ and ξ can therefore be identified as the fitted-line parameters in Fig. 2.4: $\chi = -5.8 \cdot 10^{-3} \frac{1}{K}$ and $\xi = 2.0575$. For an estimation of the time development of the ammonia concentration in the drop, we use the values from curve 6 of the concentration graph Fig. 2.5. Although it results from sophisticated numerical calculations, this curve can be approximated acceptably by the equation

$$X_B(\tau) \approx 0.2517 [1 - \exp(-0.023\tau)] \quad (2.10)$$

Assuming $x_0 = 0$ and $T_0 = 300 K$, the actual weight fraction x_B can be easily calculated from Eqn. 2.9. The dimensionless time τ as a function of the drop velocity U and time t must be developed iteratively, starting from $t = 0$:

$$d\tau = \frac{w}{R} U dt \quad (2.11)$$

$$\tau(t) = \frac{w}{R} \int_{\hat{t}=0}^t U(\hat{t}) d\hat{t} \quad (2.12)$$

or, for a numerical calculation:

$$\tau_{i+1} = \tau_i + \frac{w}{R} U_i \Delta t \quad (2.13)$$

The velocity $U(t)$ of a falling drop with an initial velocity U_0 (due to the spray injection), both in direction of the gravity must also be developed iteratively, as the magnitude of deceleration depends on the drag force which depends again on $U(t)$ and $U^2(t)$:

$$U_{i+1} = U_i - \frac{F_{d,i}}{m} \Delta t + g \Delta t \quad (2.14)$$

where $F_{d,i} = \frac{1}{2} \rho_g U_i^2 C_{d,i} R^2 \pi$ is the drag force. The equation for the drag coefficient C_d depends according to [34] on the Reynolds number $Re = \frac{2RU\rho_g}{\mu_g}$

$$Re \leq 0.2 \quad C_d = \frac{24}{Re} \left(1 + \frac{3}{16} Re + \frac{9}{160} Re^2 \ln(2Re) \right) \quad (2.15)$$

$$0.2 \leq Re \leq 500 \quad C_d = \frac{24}{Re} \left(1 + 0.15 Re^{0.687} \right) \quad (2.16)$$

$$500 \leq Re \leq 2 \cdot 10^5 \quad C_d = 0.44$$

Implemented in a LibreOffice spread sheet, one can estimate the time until the ammonia concentration in the drop reaches saturation and also the distance the drop moves until saturation. Fig. 2.6 shows the concentration of ammonia and the distance a drop moves as functions of time for different diameters and different initial velocities.

Apparently the ammonia concentration rises faster with smaller diameter (due to the higher surface-to-volume ratio). The distance a drop moves within a certain time decreases with the drop diameter due to the faster deceleration and lower terminal velocity of the smaller drops. A higher initial velocity, on the other hand, can accelerate the absorption.

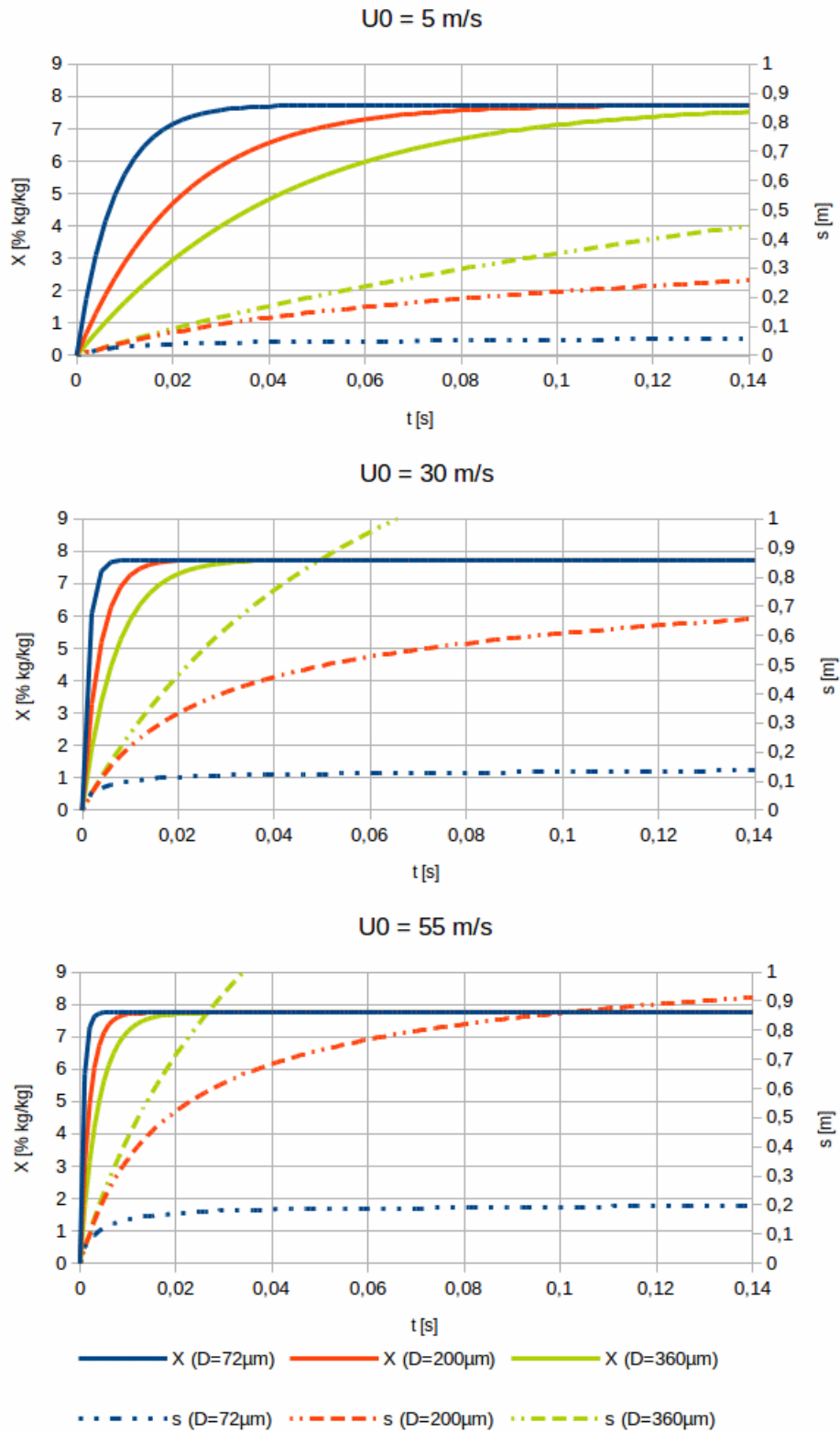


Fig. 2.6.: Ammonia concentration in a moving water drop as a function of time for different diameters and initial velocities (applied to the results of [11])

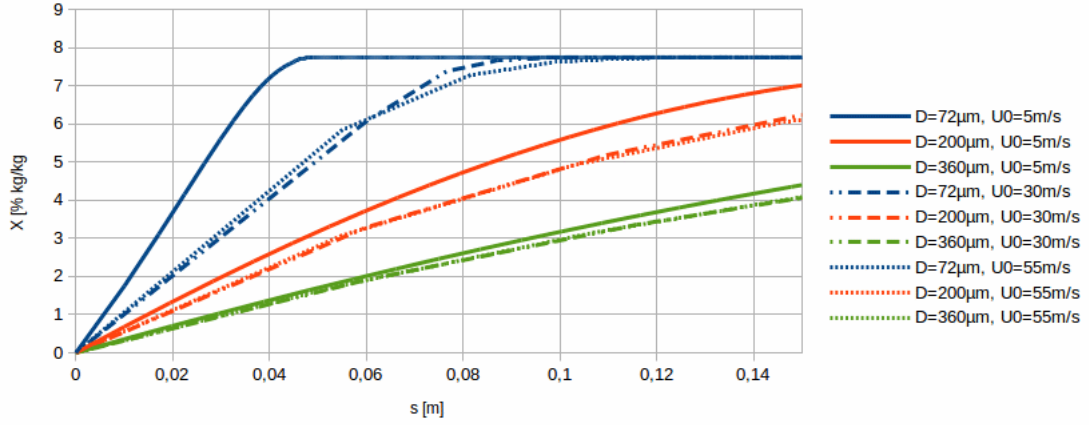


Fig. 2.7.: Ammonia concentration as a function of the distance covered by a drop.

The curves in Fig. 2.7 show the concentration as a function of the distance. The shortest distance a drop must move to reach its saturation concentration of ammonia is at lowest speed and smallest diameter.

2.3.3. Estimation of Heat Dissipation

ELPERIN assumes a negligible heat dissipation from the drop by conduction, convection or radiation, which may be justifiable for the considered drop diameters of $D = 500 \mu\text{m}$ and more. However, as the drop diameters in this thesis can be ten times smaller, heat dissipation from the drop should be considered in the calculations.

For single drop in ammonia vapor environment, power dissipation can occur by conductive and convective heat transfer through the gas and by radiation.

The power P that dissipates through a medium along a temperature difference ΔT by thermal conduction can be calculated by:

$$P = \frac{dQ}{dt} = \frac{\Delta T}{R_{th}} \quad (2.17)$$

by using the thermal resistance R_{th} defined as

$$R_{th} = \int_{r_1}^{r_2} \frac{1}{\eta A(x)} dr \quad (2.18)$$

where η is the thermal conductivity measured in $\frac{W}{mK}$ and A is the surface area. For a spheric drop of radius R , the thermal resistance between its surface and the environment becomes

$$R_{th} = \int_R^{\infty} \frac{1}{4\pi r^2 \eta} dr = \frac{1}{4\pi R \eta} \quad (2.19)$$

Eqn. 2.19 inserted in eqn. 2.17, the change rate of the temperature $\frac{dT}{dt}$ of the drop⁶ is equal to

$$\frac{dT}{dt} = \Delta T \frac{4\pi R \eta}{c_p \rho_l \frac{4}{3}\pi R^3} = (T_{\infty} - T(t)) \frac{3\eta}{c_p \rho_l R^2} \quad (2.20)$$

where c_p is the specific heat of the liquid and ρ_l is the density of the liquid. Solving this differential equation yields the temperature of the drop as a function of time

$$T(t) = (T_0 - T_{\infty}) \exp\left(-\frac{3\eta}{c_p \rho_l R^2} t\right) + T_{\infty} \quad (2.21)$$

E.g. a drop of radius $R = 50 \mu m$ of initial bulk temperature of $T_0 = 340 K$ in an ammonia atmosphere of $T_{\infty} = 300 K$ and $\eta = 2.42 \cdot 10^{-2} \frac{W}{mK}$ takes $t = 41.5 ms$ to cool down to $310 K$. The initial heat flow is $\frac{dQ}{dt} = 4.56 \cdot 10^{-4} W$. $\frac{dT}{dt}|_{r_d=50\mu m, T=340K} = 278 \frac{K}{s}$. It is obvious that conductive heat dissipation cannot be ignored for the cases considered in this thesis.

Heat dissipation by radiation is described in the Stefan-Boltzmann equation:

$$P_{rad} = \varsigma \epsilon A (T^4 - T_{\infty}^4) \quad (2.22)$$

where ς describes the Stefan-Boltzmann Constant $\varsigma = 5.57 \cdot 10^{-8} \frac{W}{m^2 K^4}$ and ϵ the radiation coefficient $0 \leq \epsilon \leq 1$. $A = 4\pi R^2$ is the surface area of the drop. At the same conditions as above, the initial power loss due to radiation is $P_{rad} = \epsilon \cdot 9.21 \cdot 10^{-6} W$, which is about 50 times less than the power loss due to conduction (and can therefore be ignored).

⁶Assuming thermal equilibrium in the bulk, no flow of the surrounding gas and no additional heat dissipation from radiation.

2.3.4. Estimation of Absorption Rate according to Fenton

In his work [12], FENTON compares different methods for ammonia trapping, i.e. for cleaning the air by absorption of waste ammonia, which may have leaked from a refrigerator or emitted from a building for livestock. One of these methods is ammonia absorption by water spray.

For the absorption rate, FENTON referred to the characterization of mass transfer given by BIRD [7]: The mol-based mass transfer rate \dot{n} $\left[\frac{mol}{s}\right]$ is proportional to the concentration difference Δc $\left[\frac{mol}{m^3}\right]$ and the interfacial area A $[m^2]$.

$$\dot{n} = k_m A \Delta c \quad (2.23)$$

where the proportionality factor k_m $\left[\frac{m}{s}\right]$ is called the mass transfer coefficient. The driving force of the mass transfer is the difference in concentration Δc . Multiplying eqn.2.23 by the molar mass M yields the mass-based mass transfer rate \dot{m} $\left[\frac{kg}{s}\right]$

$$\dot{m} = k_m A \Delta \rho \quad (2.24)$$

where $\Delta \rho$ is the density difference of ammonia. Using the boundary layer theory, FENTON assumes the mass transfer takes place in the gas phase on the drop's surface. Initially, when there is no ammonia solved in the water drop, the ammonia density on the surface of the drop is equal to zero. So $\Delta \rho$ is equal to the ammonia density ρ_{NH_3} of the atmosphere. When the absorbed ammonia has reached its saturation concentration, there is no more mass transfer between the atmosphere and the drop. This means that at this stage $\Delta \rho$ must also become equal to zero. FENTON assumes the absorption rate \dot{m} proportional to the ratio $\frac{x_s - x}{x_s}$ where x_s is the (mass-based) saturation concentration of ammonia in water and x is the actual concentration. So $\Delta \rho$ can be written as $\Delta \rho = \rho_{NH_3} \frac{x_s - x}{x_s}$. For an individual drop of diameter D in an ammonia atmosphere, eqn. 2.24 becomes

$$\dot{m} = k_m D^2 \pi \rho_{NH_3} \frac{x_s - x}{x_s} \quad (2.25)$$

In a static atmosphere, mass transfer is only driven by diffusion and the mass transfer coefficient $k_{m,0}$ (in a static fluid) is equal to the diffusion coefficient \mathcal{D}_{AW} divided by

the characteristic length, which is the drop diameter D .

$$k_{m,0} = \frac{\mathcal{D}_{AW}}{D} \quad (2.26)$$

According to the boundary layer theory, mass transfer is also driven by convection, when there is a relative velocity U between the surface and the surrounding fluid,. The ratio of the transfer coefficient in a static fluid $k_{m,0}$ to the transfer coefficient k_m in a moving fluid is called the Sherwood number [7].

$$Sh = \frac{k_m D}{\mathcal{D}_{AW}} \quad (2.27)$$

FENTON calculates the Sherwood number by the Ranz-Marshall equation for a sphere⁷ :

$$Sh = 2 + 0.6Re^{\frac{1}{2}}Sc^{\frac{1}{3}} \quad (2.28)$$

where $Re = \frac{DU\rho_g}{\mu_g}$ is the Reynolds number and $Sc = \frac{\mu_g}{\rho_g\mathcal{D}_{AW}}$ is the SCHMIDT number. The diffusion coefficient for the gas phase is estimated using procedures from [31] :

$$\mathcal{D}_{AW} = \frac{0.01013T^{1.75}D\left(\frac{1}{M_1} + \frac{1}{M_2}\right)^{0.5}}{p\left[(\sum v_1)^{\frac{1}{3}} + (\sum v_2)^{\frac{1}{3}}\right]^2} \quad (2.29)$$

where p is the atmospheric pressure, $M_{1,2}$ are the molar masses of the two species and $v_{1,2}$ are their atomic diffusion volume.

Although some complex dependencies are considered, this procedure suggested by FENTON, is still simple enough to implement it in a LibreOffice spreadsheet, in order to see how the ammonia concentration in a single falling drop evolves when some of the initial parameters are changed. Therefore, the procedure must be re-written as a numerical sequence. For calculation of the initial parameters, assuming $\Delta\rho_0 = 0$, an initial speed of U_0 and an initial temperature T_0 , the sequence can be calculated as follows:

⁷The Sherwood number is only an empirical proportionality factor. All the equations that can be found in literature to determine the Sherwood number are curves with parameters fitted to experimental results.

1. First calculate the saturation concentration $x_{s,i}$ using eqn. 2.8

$$x_{s,i} = \chi T_i + \xi \quad (2.30)$$

2. Next get the density difference

$$\Delta\rho_i = \rho_{NH_3} \frac{x_{s,i} - x_i}{x_{s,i}} \quad (2.31)$$

3. Calculate Re , \mathcal{D}_{AW} , Sh and k_m for this time step

$$Re_i = \frac{\rho_{NH_3} D U_i}{\mu_{NH_3}} \quad (2.32)$$

$$\mathcal{D}_{AW,i} = \frac{0.01013 T_i^{1.75} D \left(\frac{1}{M_1} + \frac{1}{M_2} \right)^{0.5}}{p \left[(\sum v_1)^{\frac{1}{3}} + (\sum v_2)^{\frac{1}{3}} \right]^2} \quad (2.33)$$

$$Sc = \frac{\mu_g}{\rho_g \mathcal{D}_{AW,i}} \quad (2.34)$$

$$Sh_i = 2 + 0.6 Re_i^{\frac{1}{2}} Sc_i^{\frac{1}{3}} \quad (2.35)$$

$$k_{m,i} = \frac{\mathcal{D}_{AW,i} Sh_i}{D} \quad (2.36)$$

4. Finally get the actual mass transfer rate

$$\dot{m}_i = k_{m,i} D^2 \pi \Delta\rho_i \quad (2.37)$$

5. For the next time step calculate the ammonia concentration in the drop

$$x_{i+1} = x_i + \frac{\dot{m}_i \Delta t}{\dot{m}_i \Delta t + \frac{D^3}{6} \pi \rho_{H_2O}} \quad (2.38)$$

6. The temperature for the next time step is determined by an energy gain due to the enthalpy of solution in eqn. 2.7 and an energy loss due to conductive and convective heat dissipation (eqn. 2.17)⁸. For convective heat dissipation the Nusselt number has to be determined (using the Prandtl number $Pr = \frac{\mu_{NH_3} c_{P,H_2O}}{\eta}$):

$$Nu_i = 2 + 0.6 Re_i^{\frac{1}{2}} Pr^{\frac{1}{3}} \quad (2.39)$$

$$T_{i+1} = T_i + \frac{\dot{m}_i \Delta t}{\frac{D^3}{6} \pi \rho_{H_2O}} \cdot \frac{\Delta_{sol} H_{NH_3}^0}{M_{NH_3} c_{P,H_2O}} - (T_0 - T_i) \frac{12\eta}{c_{P,H_2O} \rho_{H_2O} D^2} \cdot Nu_i \quad (2.40)$$

7. The velocity $U(t)$ of a falling drop with an initial velocity U_0 (due to the spray injection), both in direction of the gravity must also be developed iteratively, as the magnitude of deceleration depends on the drag force which depends again on $U(t)$ and $U^2(t)$. The drag coefficient $C_{d,i}$ for the current time step is a function of the Reynolds number Re determined as in 2.15.
8. Using the corresponding drag coefficient, the drag force can be determined

$$F_{d,i} = \frac{1}{8} \rho_{NH_3} U_i^2 C_{d,i} D^2 \pi \quad (2.41)$$

9. So finally the velocity for the next time step results

$$U_{i+1} = U_i - \frac{F_{d,i}}{\frac{D^3}{6} \pi \rho_{H_2O}} \Delta t + g \Delta t \quad (2.42)$$

Fig. 2.8 shows the temperature and ammonia concentration of a falling drop with $U_0 = 23 \frac{m}{s}$ and $D = 100 \mu m$ calculated by above equations. The convective heat transfer discharges the heat produced by the enthalpy of solution, which enhances the ammonia absorption.

Considering the ammonia concentration as a function of the the distance covered by the drop, Fig. 2.9 shows that small drops of $D = 72 \mu m$ can reach the ambient temperature and the maximum ammonia concentration within a distance of 0.5 m.

⁸Although Fenton only considers the heating up due to enthalpy of solution and no heat dissipation from the drops, the latter effect must also be taken into account in this estimation, as the drop diameters assumed in the current study are about five times smaller than those in [12].

The effect of convective heat dissipation soon decays with increasing diameters. For large drops of $D = 360 \mu m$ the curves become similar to the ones in Fig. 2.7.

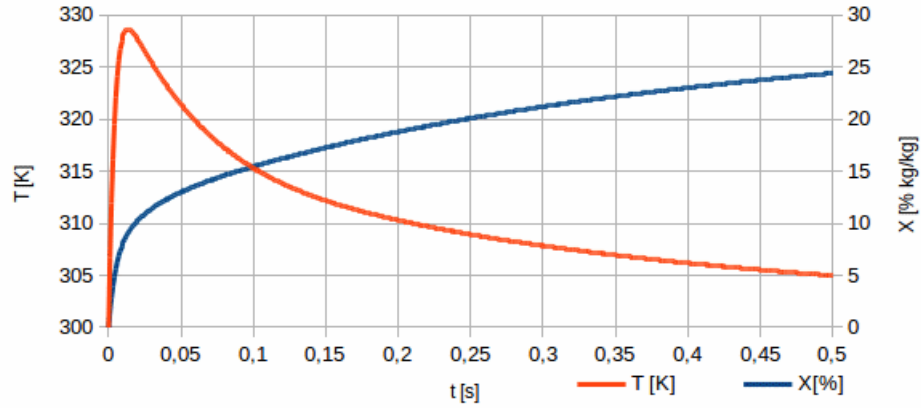


Fig. 2.8.: A water drop falling with initial velocity $U_0 = 23 \frac{m}{s}$ and diameter $D = 100 \mu m$ in ammonia atmosphere. The curves for temperature and ammonia concentration in the drop were calculated using the boundary layer theory like in [12] for the absorption rate and considering convective heat dissipation.

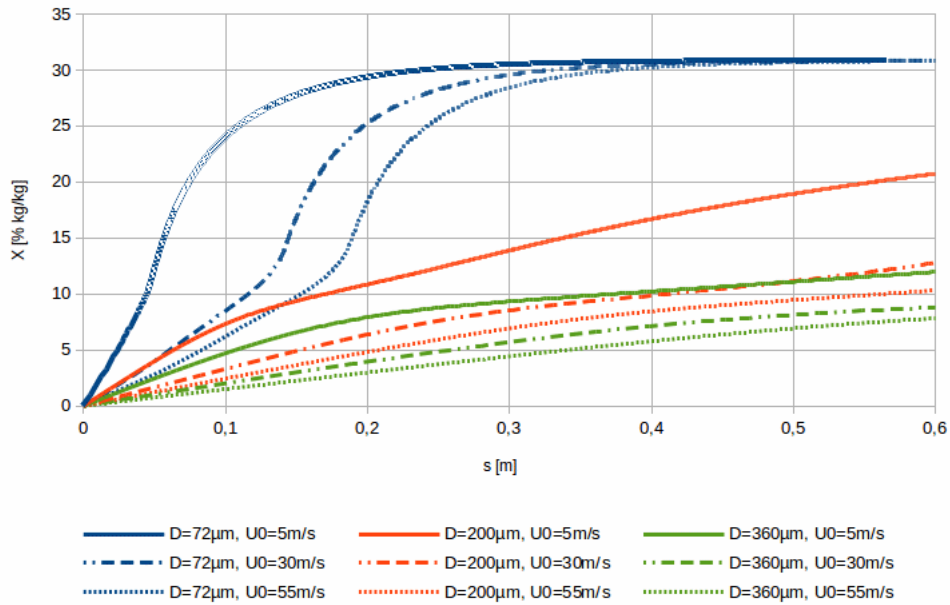


Fig. 2.9.: Set of $X(s)$ curves for different diameters and initial velocities.

2.3.5. Estimation of Heat Flux through the Chamber Walls

As already mentioned in sec. 1.3, the thermal power which has to be dissipated from the absorber chamber \dot{Q}_{AB} (which is equal to the heat flux Φ through the chamber walls⁹) is described by eqn. 1.5:

$$\dot{Q}_{AB} = \frac{\dot{m}_g}{M_g} \Delta H_{sol,g} + (T_{AB} - T_{EV}) [(1-x)c_{p,l} + xc_{p,g}] (\dot{m}_l + \dot{m}_g)$$

where $\dot{m}_l = \dot{V}_0 \rho_l = 4.067 \cdot 10^{-5} \frac{m^3}{s} \cdot 1000 \frac{kg}{m^3} = 4.067 \cdot 10^{-2} \frac{kg}{s}$ is the mass flow rate of the injected liquid \dot{m}_g can be calculated by $\dot{m}_g = \frac{x}{1-x} \dot{m}_l$

Let's assume that the life time of an average drop ($D = D_{30}$) is long enough, so that the drop's temperature T is almost equal to the chamber temperature T_{ch} when it hits the wall and leaves the chamber, so $T_{AB} = T = T_{ch}$. So the equation for Φ becomes

$$\Phi = \frac{\dot{m}_g}{M_g} \Delta H_{sol,g} + (T - T_0) (\dot{m}_l + \dot{m}_g) [(1-x)c_{p,l} + xc_{p,g}] \quad (2.43)$$

where $T_0 = 300 K$ is the initial temperature of the injected fluid. Here the ammonia mass fraction x is the saturation concentration $x_s = \chi T + \xi$ from eqn. 2.8 .Fig. 2.10 shows Φ as a function of T . It is obvious that Φ will never reach values of zero watts or below, so the chamber temperature must always be below $340 K$.

⁹ Φ has a negative sign as the direction of the heat flux points outside the chamber.

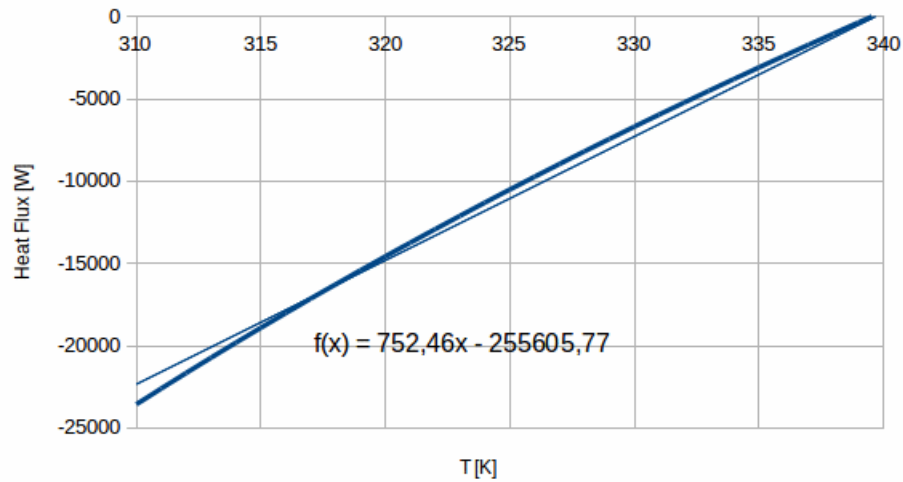


Fig. 2.10.: Heat flux Φ as a function of the final drop temperature T . The thin line in red shows the linearized approximation of Φ within the range of $310\text{ K} < T < 340\text{ K}$.

Now, let's estimate the average chamber temperature \bar{T} as a function of the heat flux Φ . For convenience consider an absorption chamber of spheric shape of radius r_o . Assume the heat source of constant flux Φ (representing the heated drops) spheric of radius r_i and placed in the center of the chamber as outlined in Fig. 2.11.

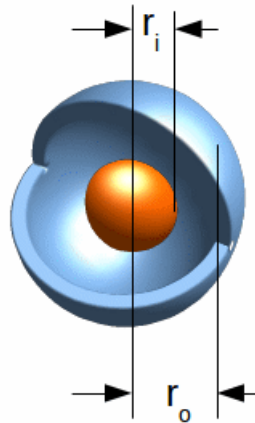


Fig. 2.11.: Simplified model of the absorber chamber: The source of the heat flux Φ , i.e. drops of higher temperature has the shape of a sphere of radius r_i . The chamber is also spheric with radius r_o .

The temperature of the chamber wall remains constant at T_0 . Using eqn. 2.17, the temperature $T(r)$ at an arbitrary point $r_i \leq r \leq r_o$ can be calculated by

$$T(r) = R_{th}(r) \Phi + T_0 \quad (2.44)$$

where $R_{th}(r)$ is the thermal resistance between r and r_o , given as

$$R_{th}(r) = \int_r^{r_o} \frac{1}{\eta A(x)} dx = \int_r^{r_o} \frac{1}{4\pi x^2 \eta} dx = \frac{r - r_o}{4\pi r_o r \eta} \quad (2.45)$$

The average temperature \bar{T} in the chamber can approximately¹⁰ be determined as

$$\bar{T} = \frac{3}{4\pi l (r_o^3 - r_i^3)} \int_{r_i}^{r_o} T(r) 4\pi r^2 dr \quad (2.46)$$

$$\bar{T} = \Phi \left(\frac{1}{4\pi r_o} - \frac{3(r_o^2 - r_i^2)}{8\pi(r_o^3 - r_i^3)} \right) + T_0 \quad (2.47)$$

The heat flux Φ in above equation depends on the average chamber temperature \bar{T} as shown in 2.43. In Fig. 2.10, Φ is also approximated by a linear equation

$$\Phi(T) \approx 752.46 \frac{W}{K} \cdot T - 255605.77 W \quad (2.48)$$

Inserted in eqn. 2.47 yields

$$\bar{T} = \frac{-255605.77 W \left(\frac{1}{4\pi r_o} - \frac{3(r_o^2 - r_i^2)}{8\pi(r_o^3 - r_i^3)} \right) + T_0}{1 - 752.46 \frac{W}{K} \left(\frac{1}{4\pi r_o} - \frac{3(r_o^2 - r_i^2)}{8\pi(r_o^3 - r_i^3)} \right)} \quad (2.49)$$

This means that the average chamber temperature \bar{T} and therefore the heat flux Φ depend mainly on the chamber dimensions and the size of the spray area. Fig. 2.12 shows Φ and T as a function of r_o at $r_i = 0.2 m$. The heat flux through the chamber walls to be expected is at about $1 kW$, the average chamber and drop temperature at about $338 K$ and the ammonia mass fraction of the strong solution at about $0.09 \frac{kg}{kg}$.

¹⁰relating T to volume elements dV instead of mass elements dm .

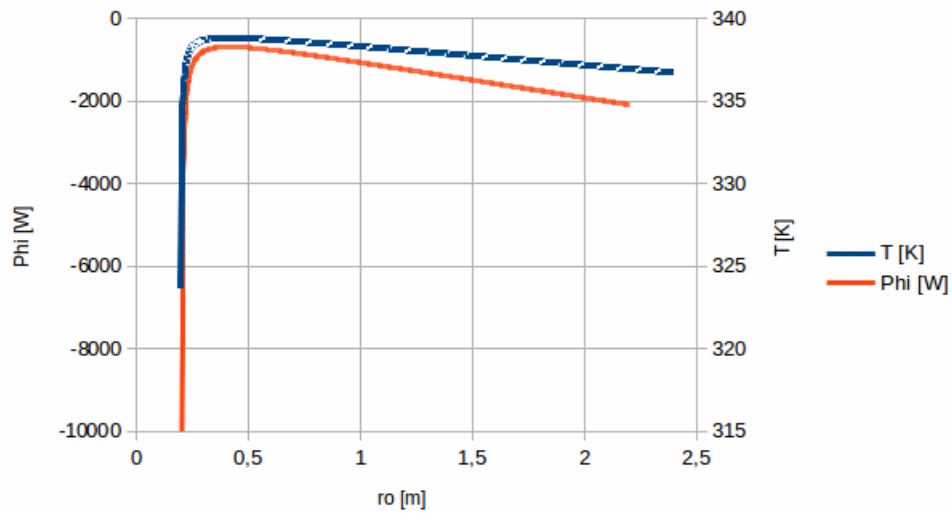


Fig. 2.12.: Φ and T plotted as a function of r_o , assuming $r_i = 0.2$ m.

2.3.6. Conclusions on Requirements for the Spray

Apparently, the best way to achieve maximum ammonia absorption within a minimum distance, is to produce small drops with low initial velocity. It will be shown in the next chapter that drops produced by a spray nozzle, however, will become smaller and faster at higher injection pressure or bigger and slower at lower injection pressure. Considering a given flow rate, a lower injection pressure requires a larger orifice at the nozzle, which results in larger drop diameters. But as can be seen in Fig. 2.9, small diameter seems to be the more effective than low velocity, so drop diameter should be the main criterion when the choosing the nozzles.

3. Sprays

3.1. Nozzle Types

Although there are many ways to produce sprays, in most cases¹ the atomization is initiated by a high relative velocity between the liquid to be atomized and the surrounding gas. Some nozzles accomplish this by discharging the liquid at high velocity into a slow-moving gas while other types of nozzles inject a slow-moving liquid into a high-velocity air stream.

In view of the wide variety of spray nozzles (see [22, 4]), each developed for a special application and a particular range of flows, we shall concentrate on the types that come into consideration for a setup described in sec. 2.2.3: Simple, cheap and designed for relatively low pressure and small drop diameter.

3.1.1. Plain Orifice Nozzles

A simple circular orifice is used to inject a round jet of liquid into the surrounding gas. The smaller the orifice, the smaller the diameters of the drops. Also higher injection pressure leads to smaller diameters. Due to possible contamination of the liquid with particles which might clog the orifice, the minimum orifice diameter is limited. The main application for plain orifice nozzles is in fuel combustion. The advantage of plain orifice nozzles is its robustness due to the simple design.

3.1.2. Twin-Fluid Nozzles

In twin-fluid atomizing nozzles, shown in Fig. 3.1, a high velocity gas stream is brought in contact with a liquid stream. This can be done either within or outside

¹Except for some “exotic”, scarcely used methods like supersonic or electrostatic atomization[4, 38].

of the nozzle. This way, twin-fluid atomizing nozzles can generate small drops at low liquid flow rates. Although both properties would be desirable for the spray absorber as shown in sec. 2.3, a twin-fluid nozzle cannot be used for this application, as, besides the liquid, compressed air is also injected into the absorber. This air would dilute the ammonia vapor atmosphere and reduce the absorption process.

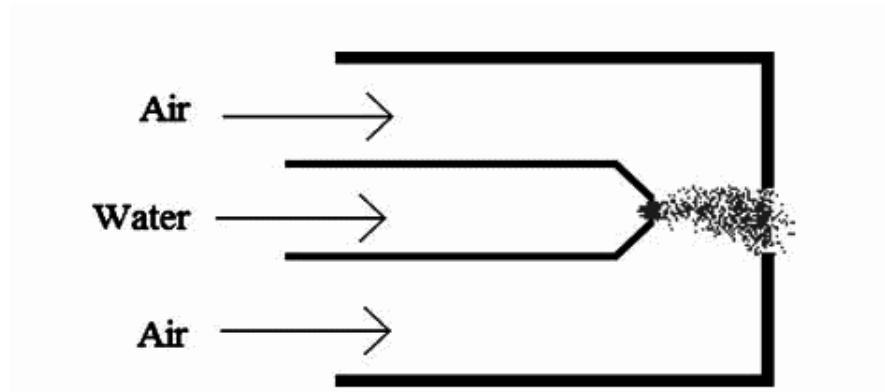


Fig. 3.1.: *Schematic of a twin-fluid nozzle [4]*

3.1.3. Pressure Swirl Nozzles

In swirl nozzles, the liquid is being swirled within the nozzle. The centrifugal force acting on the liquid results in the formation of a sheet which later breaks into droplets. Depending on the design of the nozzle, the shape of the spray can be a full cone or a hollow cone. To produce a hollow cone, the liquid is injected tangentially into a circular chamber, as shown in Fig. 3.2, (a). Flowing only on the chamber walls, the liquid emerges from the nozzle along the edges of the orifice and forms an annular sheet. For the full cone, the liquid is injected axially into the chamber and develops a swirl guided by spiral grooves at the outlet as outlined in Fig. 3.2 (b).

Swirl nozzles are the most common type of nozzles found in use today. Although the the drop diameters still depend on the orifice diameter, they can also be influenced by the design of the swirl chamber and the resulting spray angle. At a given injection pressure and flow rate, the mean drop diameter of a spray produced from a swirl nozzle is significantly smaller than from a plain orifice nozzle.

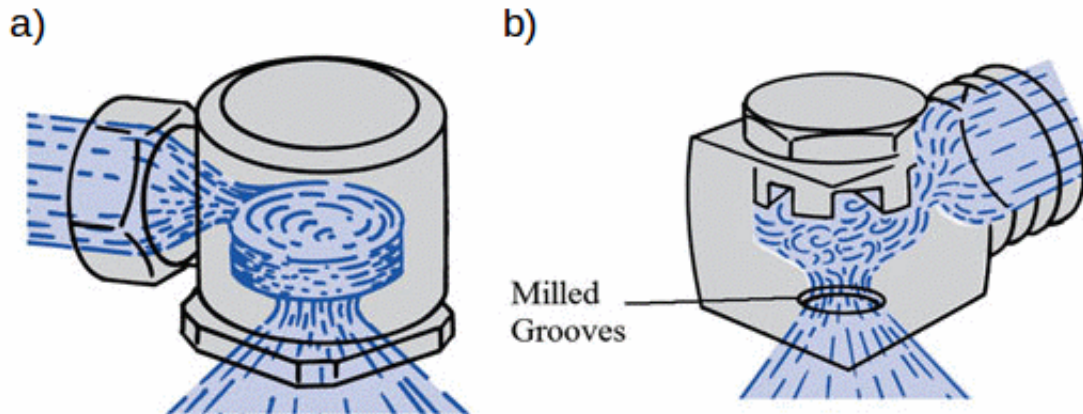


Fig. 3.2.: Schematic of a hollow cone nozzle (a) and a full cone nozzle (b) [4]

Swirl nozzles are the preferred type for spray absorption. WARNAKULASURIYA [36] compares the efficiency of different nozzles on spray absorption experimentally and shows that swirl nozzles produce the most efficient spray. As the mean drop diameter of a hollow cone spray produced by a swirl nozzle is smaller than the one from a full cone spray (at same pressure and flow rate), the preferred injection type to be modeled for this work is a hollow-cone swirl nozzle.

3.2. Mechanism of Atomization

3.2.1. Atomization of a Liquid Sheet

For swirl nozzles the cone-shaped liquid sheet can approximately be considered as a two-dimensional planar sheet. While moving through a gaseous medium, the sheet will be disturbed by shear forces acting on its surface. Counterforced by surface tension forces the disturbances finally develop oscillations and waves on the liquid sheet. In the linear stability theory [4], two modes of oscillation are considered: symmetric and antisymmetric (see Fig. 3.3). In the symmetric mode the middle plane is undisturbed, while in the antisymmetric mode, the free surfaces move in the same direction and with the same magnitude so that sinuous waves develop. The latter is the dominant mode of disturbance².

²at least in the cases discussed in this work with quite low velocity and pressure

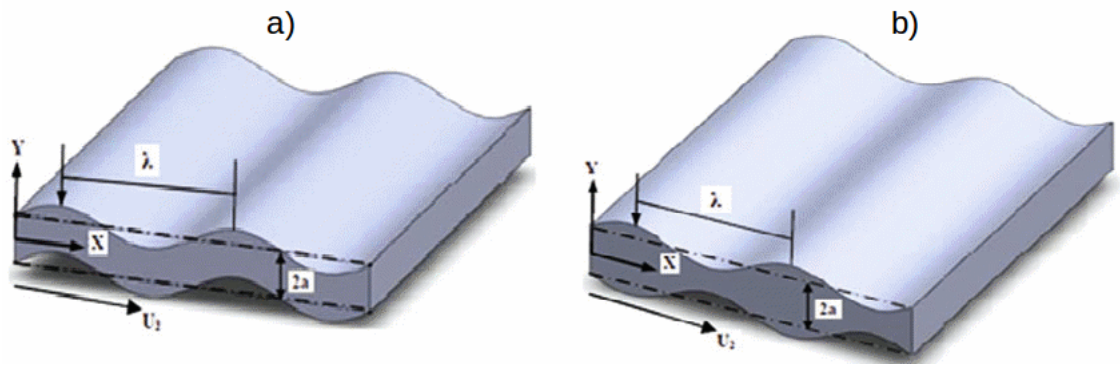


Fig. 3.3.: Schematic of (a) antisymmetric (sinuous) disturbance and (b) symmetric disturbance [4]

The sheet is unstable for axial disturbances with a wavelength greater than the cut-off wavelength λ_c , but stable otherwise. As shown in Fig. 3.4, the amplitude of the disturbance wave with $\lambda > \lambda_c$ grows until the sheet breaks into ligaments which finally form the drops.

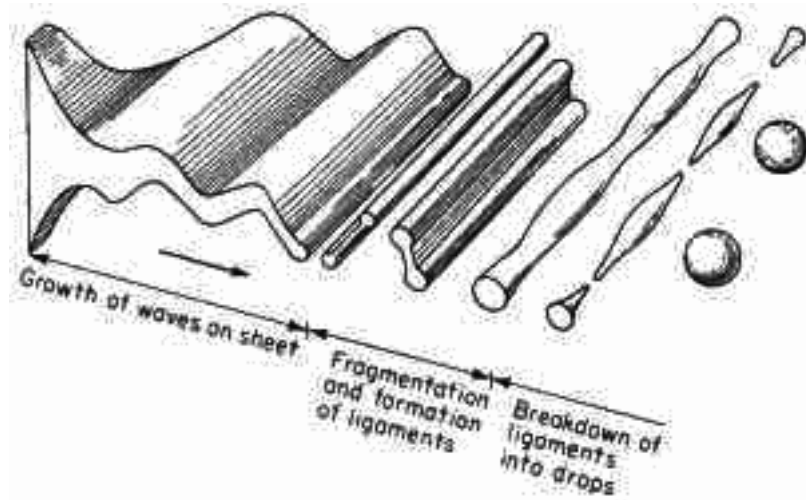


Fig. 3.4.: Schematic of the breakup process from a liquid sheet. The drop diameters are of the same dimension as the sheet thickness [30]

The growth rate ω of a wave describes the increase of the displacement z of the surface

$$z = \mathcal{A} \exp(\omega t) \tag{3.1}$$

where \mathcal{A} is the amplitude of the initial disturbance. The sheet breaks off into liga-

ments when the amplitude of the disturbance is equal to half of the sheet thickness. The wave with the maximum growth rate, whose wavelength is called dominant wavelength, dominates the breakup and droplet formation process. Hence, the majority of the drops formed in the spray correspond to the wave with the dominant wavelength. However, however, as all the unstable waves within the spectrum of the wavelength are amplified, drops are formed corresponding to each of the unstable wavelengths λ .

According to [20], the mean volume diameter D_{30} of the developing drops depends on the sheet thickness t_s and the dominant wavelength:

$$D_{30} = \zeta t_s \sqrt{\lambda_b} \quad (3.2)$$

where the constant factor ζ can be assumed equal to 3 [24] (but may vary with different nozzle types). λ_b denotes the dimensionless interval (normalized by the half sheet thickness $\frac{t_s}{2}$) between the successive breakup points of the liquid sheet corresponding to the dominant wavelength.

The dimensionless drop diameter $\bar{D} = \frac{D}{D_{30}}$ corresponding to the unstable wavelength λ , is given by [20]

$$\bar{D} = \sqrt{\frac{\lambda}{\lambda_b}} \quad (3.3)$$

From this follows the wave number k :

$$k = \frac{2\pi}{\lambda_b \bar{D}^2} \quad (3.4)$$

or, using eqn. 3.2:

$$k = \frac{2\pi}{\bar{D}^2} \sqrt{\frac{3t_s}{2D_{30}}} \quad (3.5)$$

The dimensionless growth rate $\bar{\omega}$ as a function of k is given by ASHGRIZ [4] for planar liquid sheets:

$$\bar{\omega} = \frac{\omega}{kU_l} = \sqrt{\frac{\frac{\rho_g}{\rho_l} \tanh\left(\frac{t_s}{2}k\right)}{\left(\frac{\rho_g}{\rho_l} + \tanh\left(\frac{t_s}{2}k\right)\right)^2} - \frac{\frac{t_s}{2}k}{We\left(\frac{\rho_g}{\rho_l} + \tanh\left(\frac{t_s}{2}k\right)\right)}} \quad (3.6)$$

where $We = \frac{\rho_g U_l^2 t_s}{\sigma}$ is the WEBER number, ρ_g and ρ_l denote the density of gas and liquid and U_l is the velocity of the liquid sheet.

3.2.2. Satellite Droplets

Despite the linear break-off theory, not all of the drops produced from the liquid sheet correspond to the wavelength λ of the instable waves. During atomization, when the drops break off from the ligaments, small satellite droplets are formed from liquid threads between the main drops (see Fig. 3.5). These satellite droplets account for the “left-hand side” of the drop diameter distribution and have to be considered in the spray model.

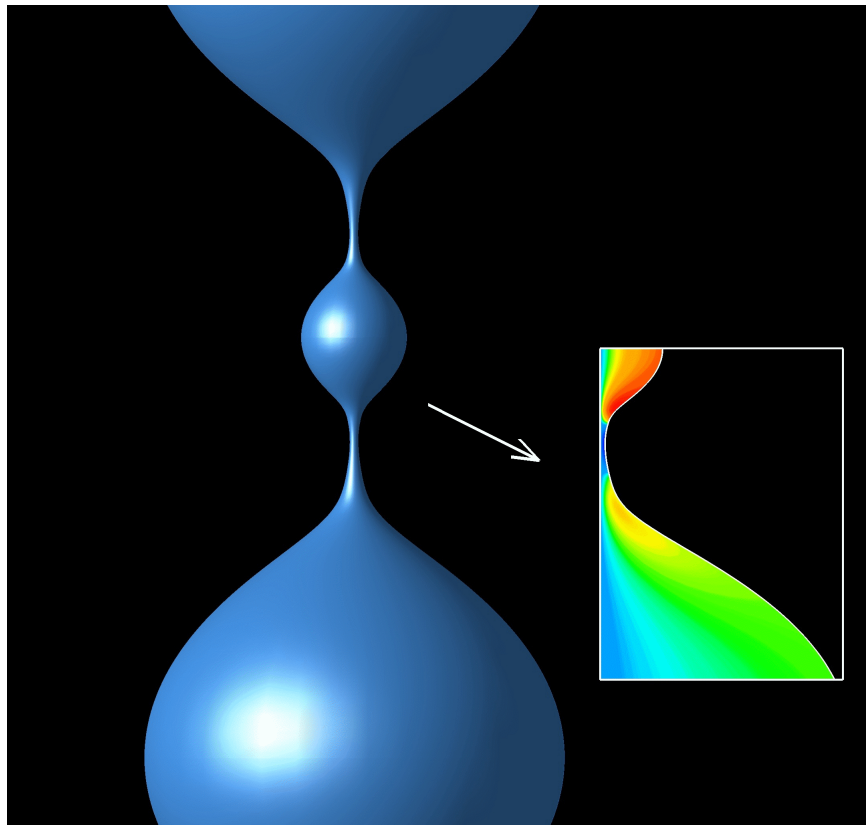


Fig. 3.5.: *Simulated breakoff of a drop from the bulk. A small satellite droplet develops in the middle of the breakoff-thread [35].*

3.3. Mean Drop Diameters

For estimating the effect of a spray in terms of drop dimensions, the parameters diameter, surface area and volume are of interest. In order to characterize spray properties regarding one or two of these three parameters, different definitions for the “mean drop diameter” have been developed and adopted. (See LEFEBVRE [22] or SOWA [33] for a detailed overview.)

Consider a spray consisting of drops of a certain diameter distribution. Let N_i be the number of drops in the size range i and D_i be the average diameter of the size range i . The average diameter \bar{D} then can be expressed as

$$\bar{D} = \frac{\sum N_i D_i}{\sum N_i} \quad (3.7)$$

or, using a continuous frequency distribution $\frac{dN}{dD}$

$$\bar{D} = \frac{\int_{D_{min}}^{D_{max}} D \left(\frac{dN}{dD} \right) dD}{\int_{D_{min}}^{D_{max}} \left(\frac{dN}{dD} \right) dD} \quad (3.8)$$

In order to determine the total surface of the drops, it is necessary to consider the average surface of a drop, the so-called “surface mean” D_{20} .

$$\bar{D}_{surf} = D_{20} = \left(\frac{\int_{D_{min}}^{D_{max}} D^2 \left(\frac{dN}{dD} \right) dD}{\int_{D_{min}}^{D_{max}} \left(\frac{dN}{dD} \right) dD} \right)^{\frac{1}{2}} \quad (3.9)$$

The subscripts “20” follow a convention introduced by MUGELE and EVANS [28] to

classify the different mean diameters. In general the definition for the subscripts is

$$D_{ab} = \left(\frac{\int_{D_{min}}^{D_{max}} D^a \left(\frac{dN}{dD} \right) dD}{\int_{D_{min}}^{D_{max}} D^b \left(\frac{dN}{dD} \right) dD} \right)^{\frac{1}{a-b}} \quad (3.10)$$

Tab. 3.1 lists the common mean diameters. The Sauter Mean Diameter (SMD) is the most commonly used representative diameter in describing the properties of a spray respectively of a nozzle. The ratio of volume to surface area is one of the main parameters for chemical reactions or absorption.

Symbol	Name	Meaning
D_{10}	Diameter mean	Average diameter of a drop
D_{20}	Surface mean	Diameter of the drop whose surface area is equal to the total surface area of the entire spray divided by the number of drops
D_{30}	Volume mean	Diameter of the drop whose volume is equal to the total volume of the entire spray divided by the number of drops
D_{32}	SAUTER Mean Diameter (SMD)	Diameter of the drop whose ratio of volume to surface area is the same as that of the entire spray

Tab. 3.1.: Common mean diameters and their meaning [22]

3.4. Drop Size and Velocity Distribution

Besides knowledge of the mean drop diameter, also the distribution and spread of the drop diameter is of interest. The classical way to describe the drop size distribution is empirical where a curve is fit to measured values. A commendable summary of empirical drop size distributions is given by BABINSKY [5]. The most commonly used empirical distribution is the Rosin-Rammler distribution which will be described next.

3.4.1. Rosin-Rammler Distribution

Although originally developed for powders, the Rosin-Rammler distribution became the standard characterization for drop size distribution. It is usually expressed in the cumulative form:

$$1 - G = \exp \left[- \left(\frac{D}{K} \right)^q \right] \quad (3.11)$$

where G denotes the fraction of the total volume contained in drops of smaller diameter than D . The shape of the distribution is defined by the parameters K and q . 63.2 % of the total liquid volume is contained in drops of diameter less than K . The distribution with is characterized by q : the smaller the value of b , the higher the distribution width. Typical values of b can be found in the range of 1 to 3, while the value of K is always close to the mean volume diameter D_{30} .

3.4.2. Maximum Entropy Formalism (MEF)

Since the 1980's the maximum entropy formalism (MEF) has been developed as an alternative to the empirical method (see [5]). Based on the thermodynamic principle of maximum entropy, the MEF assumes that the most likely distribution of drop properties maximizes the entropy of the system. The great advantage is that the resulting distribution function is a joint diameter-velocity distribution³. Beyond that, the MEF only requires parameters which are known from the operating conditions or can be read from the nozzle's data sheet. Therefore, the MEF was the chosen method for this thesis. In literature, several different approaches to the MEF can be found. For this work, the author followed the procedure of MITRA [24], KIM [20] and YAN [39] (who recently applied the MITRA-KIM-style MEF to swirl nozzles [40]) respectively.

According to the Second Law of Thermodynamics, an isolated system evolves to-

³In contrary to the Rosin-Rammler distribution which only describes the diameter distribution. Acutally, in all the cited papers on MEF ([10, 12, 20, 23, 26, 39, 40]) the resulting joint-diameter-velocity distribution was finally being integrated over velocity as the authors were only interested in the diameter distribution.

wards thermodynamic equilibrium which is the state where the entropy

$$S = k_B \ln(\Omega) \quad (3.12)$$

of the system maximizes (where k_B denotes the Boltzmann constant and Ω the number of configurations of the system). This equation for the entropy of a macro-state can also be expressed by the probabilities p_i of the distinct micro-states (also known as SHANNON's entropy).

$$S = k_B \sum_i p_i \ln(p_i) \quad (3.13)$$

The difference of entropy from one macro-state to the next (or “the measure of the nearness of the two probability distributions” [20]) is defined by the BAYESIAN entropy⁴.

$$I = k_B \sum_i p_i \ln \frac{p_i}{p_{0,i}} \quad (3.14)$$

where $p_{0,i}$ is the prior distribution of the state i .

For the MEF applied to drop distributions in sprays, the initial assumption of this method is that the most likely probability distribution $p(D, U)$ is the one that minimizes the BAYESIAN entropy I , in our case expressed by

$$I = k_B \sum_i \sum_j p_{ij} \ln \frac{p_{ij}}{p_{0,ij}} \quad (3.15)$$

where p_{ij} is the probability for a drop having a diameter of $D_i \leq D < D_{i+1}$ and a velocity of $U_j \leq U < U_{j+1}$. $p_{0,ij}$ is the prior distribution of the state ij . The distribution function $p(D, U)$ can then be determined by Lagrangian multipliers [15] if the following constraints are fulfilled:

- Conservation of mass

$$\sum_i \sum_j p_{ij} \frac{\pi}{6} D_i^3 \rho_l \dot{N} = \dot{m}_l + S_m \quad (3.16)$$

⁴If $p_{0,ij} = 1$, eqn. 3.15 describes the SHANNON's entropy. It is used in some studies [26, 23] instead of the BAYESIAN entropy. However, the assumption of a uniform prior distribution results in a probability distribution $\lim_{\bar{D} \rightarrow 0} f(\bar{D}, \bar{U}) \neq 0$ which does not match experimental data [5].

- Conservation of momentum

$$\sum_i \sum_j p_{ij} \frac{\pi}{6} D_i^3 \rho_l \dot{N} U_j = \dot{m}_l U_l + S_{mv} \quad (3.17)$$

- Conservation of energy

$$\sum_i \sum_j p_{ij} \left[\frac{1}{2} \left(\frac{\pi}{6} D_i^3 \rho_l \dot{N} U_j^2 \right) + \sigma \pi D_i^2 \dot{N} \right] = \frac{1}{2} \dot{m}_l U_l^2 + S_e \quad (3.18)$$

- Definition of probability

$$\sum_i \sum_j p_{ij} = 1 \quad (3.19)$$

where S_m , S_{mv} and S_e denote the source terms of mass, momentum and energy, \dot{m}_l is the liquid mass flow, \dot{N} is the drop flow and σ is the surface tension of the liquid.

Depending on the nozzle type, the equations for the source terms must be setup accordingly or can be found in literature (DUMOUCHEL [10] applied the MEF for solid cone nozzles, MOVAHEDNEJAD did it for hollow cone nozzles [26] and YAN for swirl nozzles [40]).

By means of simplification, droplet diameter can be scaled with the mass-mean diameter $\bar{D}_i = \frac{D_i}{D_{30}}$ and the droplet velocity can be scaled with the liquid velocity at the atomizer exit $\bar{U}_j = \frac{U_j}{U_l}$. The source terms must then be scaled accordingly: $\bar{S}_m = \frac{S_m}{\dot{m}_l}$, $\bar{S}_{mv} = \frac{S_{mv}}{\dot{m}_l U_l}$, $\bar{S}_e = \frac{S_e}{\dot{m}_l U_l^2}$. Substituting the term $\frac{12\sigma}{\rho_l U_l^2 D_{30}}$ by B , the equations become:

$$\sum_i \sum_j p_{ij} \bar{D}_i^3 = 1 + \bar{S}_m \quad (3.20)$$

$$\sum_i \sum_j p_{ij} \bar{D}_i^3 \bar{U}_j = 1 + \bar{S}_{mv} \quad (3.21)$$

$$\sum_i \sum_j p_{ij} \left(\bar{D}_i^3 \bar{U}_j^2 + \bar{D}_i^2 B \right) = 1 + \bar{S}_e \quad (3.22)$$

$$\sum_i \sum_j p_{ij} = 1 \quad (3.23)$$

From these equations the Lagrangian function \mathcal{L} [15] results⁵:

$$\begin{aligned} \mathcal{L}(p_{ij}, \Lambda) = & \sum_j \sum_i p_{ij} \ln \frac{p_{ij}}{p_{0,ij}} + \Lambda_0 \left(\sum_i \sum_j p_{ij} - 1 \right) + \Lambda_1 \left(\sum_i \sum_j p_{ij} \bar{D}_i^3 - 1 - \bar{S}_m \right) \\ & + \Lambda_2 \left(\sum_i \sum_j p_{ij} \bar{D}_i^3 \bar{U}_j - 1 - \bar{S}_{mv} \right) + \Lambda_3 \left(\sum_i \sum_j p_{ij} (\bar{D}_i^3 \bar{U}_j^2 + \bar{D}_i^2 B) - 1 - \bar{S}_e \right) \end{aligned} \quad (3.24)$$

For the solution, all derivatives of \mathcal{L} must be equal to zero:

$$\frac{\partial}{\partial p_{ij}} \mathcal{L} = \left(\ln \frac{p_{ij}}{p_{0,ij}} + 1 \right) + \Lambda_0 + \Lambda_1 \bar{D}_i^3 + \Lambda_2 \bar{D}_i^3 \bar{U}_j + \Lambda_3 (\bar{D}_i^3 \bar{U}_j^2 + \bar{D}_i^2 B) = 0 \quad (3.25)$$

$$\frac{\partial}{\partial \Lambda_0} \mathcal{L} = \sum_i \sum_j p_{ij} - 1 = 0 \quad (3.26)$$

$$\frac{\partial}{\partial \Lambda_1} \mathcal{L} = \sum_i \sum_j p_{ij} \bar{D}_i^3 - 1 - \bar{S}_m = 0 \quad (3.27)$$

$$\frac{\partial}{\partial \Lambda_2} \mathcal{L} = \sum_i \sum_j p_{ij} \bar{D}_i^3 \bar{U}_j - 1 - \bar{S}_{mv} = 0 \quad (3.28)$$

$$\frac{\partial}{\partial \Lambda_3} \mathcal{L} = \sum_i \sum_j p_{ij} (\bar{D}_i^3 \bar{U}_j^2 + \bar{D}_i^2 B) - 1 - \bar{S}_e = 0 \quad (3.29)$$

Eqn. 3.25 can be re-written as

$$p_{ij} = p_{0,ij} \exp \left[-1 - \Lambda_0 - \Lambda_1 \bar{D}_i^3 - \Lambda_2 \bar{D}_i^3 \bar{U}_j - \Lambda_3 (\bar{D}_i^3 \bar{U}_j^2 + \bar{D}_i^2 B) \right] \quad (3.30)$$

⁵For convenience, instead of the BAYESIAN entropy I , the function to be minimized is $\frac{I}{k_b}$.

Finally, it is obvious that the discrete probability function p_{ij} can be replaced by a continuous probability density function

$$f(\bar{D}, \bar{U}) = f_0 \exp \left[-1 - \Lambda_0 - \Lambda_1 \bar{D}^3 - \Lambda_2 \bar{D}^3 \bar{U} - \Lambda_3 (\bar{D}^3 \bar{U}^2 + \bar{D}^2 B) \right] \quad (3.31)$$

For this work, the Lagrangian equation has been solved using a Scilab library function which uses the Powell hybrid method. Fig. 3.6 shows a joint diameter-velocity distribution function calculated for a 1-8-Ax-5-5W nozzle from Spraying Systems Co..

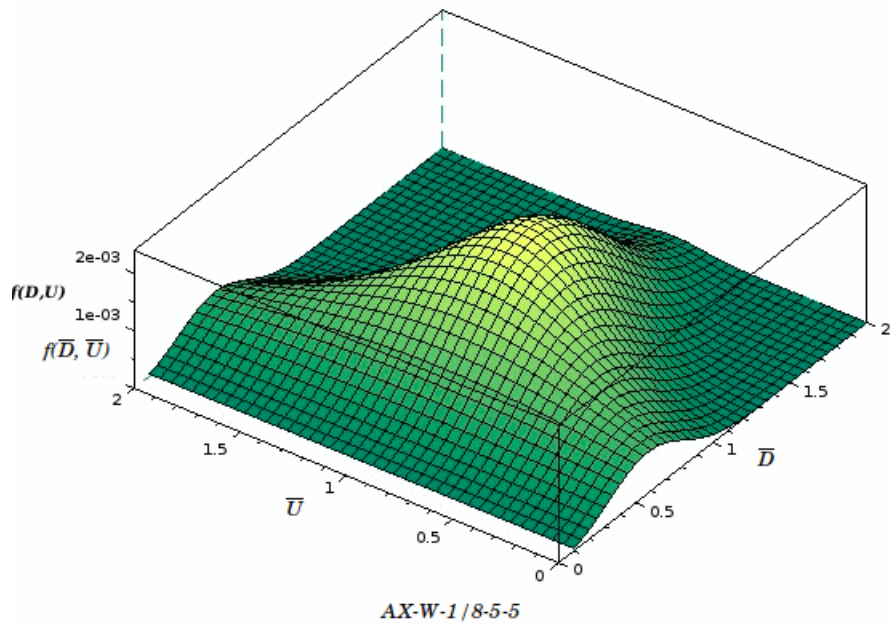


Fig. 3.6.: *Joint diameter-velocity distribution function calculated by the MEF for a 1-8-Ax-5-5W nozzle from Spraying Systems Co..*

3.4.2.1. Prior Distribution Function

For the prior distribution function, MITRA [24] and KIM [20] refer to the breakup process, where the drops are formed corresponding to wavelength λ of the unstable waves, as described in sec. 3.2.1. Therefore, they assume the prior distribution f_0 proportional to the linear growth rate $\bar{\omega}$ of all the unstable waves⁶ (eqn. 3.6).

⁶Although eqn. 3.6 denotes ω as a function of k , it can easily be transformed into a function of \bar{D} by using eqn. 3.5.

According to the linear instability theory, waves are stable if their wavelengths are less than the cut-off wavelength λ_c which is above zero and approaches zero as the liquid velocity (or more precisely, the Weber number) is increased. However, drops with sizes less than D_c (which corresponds to the cut-off wavelength λ_c) may be produced in sprays due to the satellite drop formation. To accommodate this fact, MITRA and KIM assume⁷ the prior distribution f_0 to vary as the square of the drop diameter in that range:

$$f_0 = \begin{cases} \kappa \bar{D}^2 & \bar{D} \leq \bar{D}_{cr} \\ \bar{\omega}(\bar{D}) & \bar{D} > \bar{D}_{cr} \end{cases} \quad (3.32)$$

where the values κ and \bar{D}_{cr} (=critical diameter) are parameters to accomplish a smooth⁸ connection between the two regions. Fig. 3.7 shows an example of a prior distribution function.

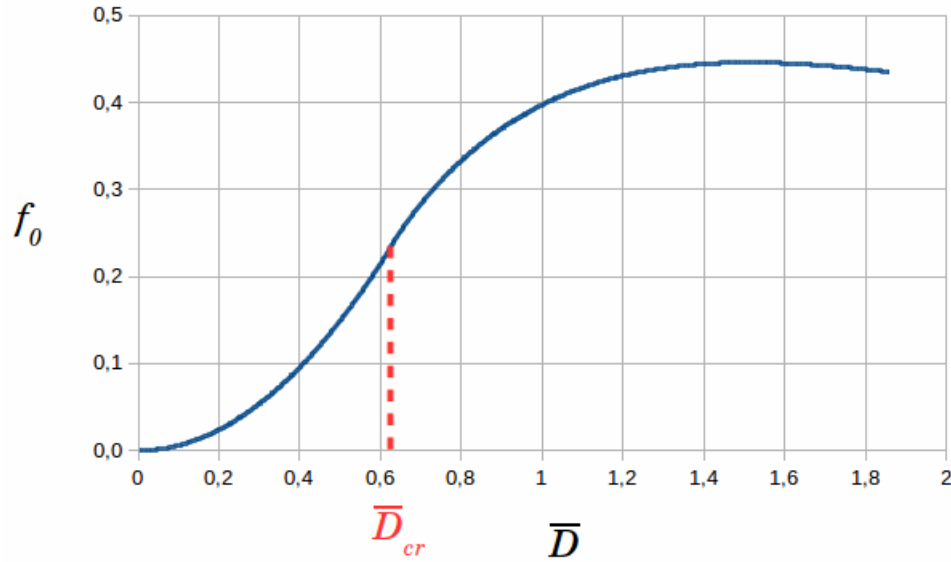


Fig. 3.7.: Prior distribution function f_0 according to eqn. 3.32, calculated for $We = 9.24$, $t_s = 2.93 \cdot 10^{-4}m$, $D_{30} = 5.84 \cdot 10^{-5}m$. The two regions are connected at $\bar{D}_{cr} = 0.626$ and $\kappa = 0.597$.

⁷“...without giving any physical justification for that” as Dumouchel criticizes in [10]

⁸“Smooth” means $\kappa \bar{D}_{cr}^2 = \bar{\omega}(\bar{D}_{cr})$ and $\frac{d}{d\bar{D}} \kappa \bar{D}_{cr}^2 = \frac{d}{d\bar{D}} \bar{\omega}(\bar{D})|_{\bar{D}_{cr}}$. The parameters κ and \bar{D}_{cr} can be identified by solving these two equations.

3.4.2.2. Source Terms

In order to calculate the drop-size-velocity distribution function for a certain nozzle at certain conditions (e.g. flow rate and pressure), one has to identify the mass-, momentum- and energy source terms within the control volume (i.e. from the point where the droplets form from ligaments to the point where they have reached their final diameter and velocity). The mass source term S_m is always considered equal to zero (as there is no mass source or drain within the control volume). However, the terms for momentum S_{mv} and energy S_e may vary with different methods of atomization. Equations for the specific source terms can be found in literature [10, 26, 40].

4. Modeling the Nozzle

4.1. About OpenFOAM

OpenFOAM (for "Open source Field Operation And Manipulation") is an object-oriented toolbox written in C++ for the development of customized numerical solvers. It is based on the finite-volume method and thereby the proper tool for the solution of continuum mechanics and fluid dynamics problems [8]. Besides simulating continuous fluids, OpenFOAM provides the option to integrate clouds of particles into the simulation and have them interact physically and chemically with the fluid. Position and velocity of these particles are calculated using the Lagrangian description. The template C++ classes collected in the "Lagrangian" library folder of the OpenFOAM standard distribution package provide a wide variety of properties and abilities which can be assigned to the particles. All kinds of mass and energy transfer (mechanical, thermal and chemical) with the fluid environment can be integrated in the simulation by including the relevant classes into the solver (and by configuring the specific properties when setting up the simulation).

4.2. Available Injection Models in OpenFOAM

Simulating the spray in order to maximize the ammonia absorption requires a detailed and exact model with regard to velocity and diameter of the drops and their distributions, for those are the parameters that control the absorption process, as shown in sec. 2.3.

It would be possible to model each of the different stages of atomization, starting from the injection of the liquid into the swirl chamber, following up with the development of the liquid sheet at the nozzle exit, finishing with the detailed breakup process which generates the drops and satellite droplets. The OpenFOAM standard

distribution package actually contains template objects for liquid sheets. However, this would consume a large part of the computing capacity. Due to the fact, that the spray phases before breakup do not account for absorption [34], a detailed simulation of the atomization process is not maintainable. So it is important to find a proper model that is able to simply inject drops with the required distribution of number, diameter and velocity

The class “ReactingCloud” provides a set of different injection models that can be used to describe a bulk of drops regarding their initial properties. Besides simple models like “ManualInjection” where the initial position of each individual drop has to be determined in a separate position file, the class “ConeNozzleInjection” can be used to describe several nozzle-specific properties. The inner and outer spray cone angle, position and direction of the nozzle can be defined as well as flow rate, start and duration of the injection. For the drop size distribution, the user can choose between Rosin-Rammler, exponential, normal and uniform distribution. However, the initial velocity, although configurable, is set the same value for all drops.

4.3. Required Extensions for the Injection Model

As velocity and drop diameter play important roles for absorption, it appears wrong to describe the spray by a one-dimensional distribution of only drop diameter, ignoring any distribution in velocity (as it is implemented in the “ConeNozzleInjection” model)¹. For lack of an already existing model that could describe a joint diameter-velocity distribution a new injection model “SwirlNozzleInjection”, based on “ConeNozzleInjection” had to be implemented. Also the tangential velocity component of the drops due to the swirl has been regarded in this model. As the liquid sheet of the spray cone hardly affects the total amount absorption as shown above, the drops will be created in an annular area, in a breakup length L_b distance away from the nozzle exits position.

To simulate a swirl nozzle by this model, the user has to define configuration parameters (additionally to the parameters needed for “ConeNozzleInjection”): The Lagrangian multipliers $\Lambda_{0,1,2,3}$ for the MEF (see sec. 3.4.2), the parameters for the prior distribution function κ and \bar{D}_{cr} , the maximum value of the distribution func-

¹Besides that, the parameters for the Rosin-Rammler distribution for individual nozzles had to be determined by experiment or by curve-fit, as this data is not provided by the producer.

tion f_{max} , the mean values for diameter and velocity D_{30} , U_l , the sheet thickness t_s and the breakup length L_b .

4.4. Implementation in OpenFOAM

4.4.1. Generating random variables with a specific probability distribution

The MEF predicts the probability for drops with a certain diameter and velocity. In the simulation, the parcels representing the drops must meet this probability distribution. However, the standard libraries of C only contains functions to generate uniformly distributed random numbers. Although OpenFOAM provides also normal, exponential or even Rosin-Rammler distributions to be used for the generation of random numbers, so far there is no implementation of a two-dimensional joint probability distribution in the OpenFOAM standard toolbox. Therefore, a method to gain random numbers according to the joint diameter-velocity probability distribution $f(\bar{D}, \bar{U})$ had to be implemented as a part of the “SwirlNozzleInjection” class.

This method is based on the “acceptance-rejection algorithm” which is a type of Monte-Carlo method [27]: First, a uniformly distributed random vector \vec{x} in the domain of a given probability distribution function $h(\vec{x})$ is sampled. Subsequently, a uniformly distributed random scalar l between 0 and any arbitrary ceiling value $\hat{l} \leq \hat{h}$ (where \hat{h} is the maximum value of $h(\vec{x})$) is sampled. If $l \leq h(\vec{x})$ the random vector \vec{x} is accepted, otherwise \vec{x} will be rejected, the sequence repeats and a new set of \vec{x} and l will be sampled. The resulting (i.e. only the accepted) random variable \vec{x} is then distributed with $h(\vec{x})$. Fig. 4.1 shows the flow chart of the acceptance-rejection algorithm applied to joint diameter-velocity probability distribution $f(\bar{D}, \bar{U})$.

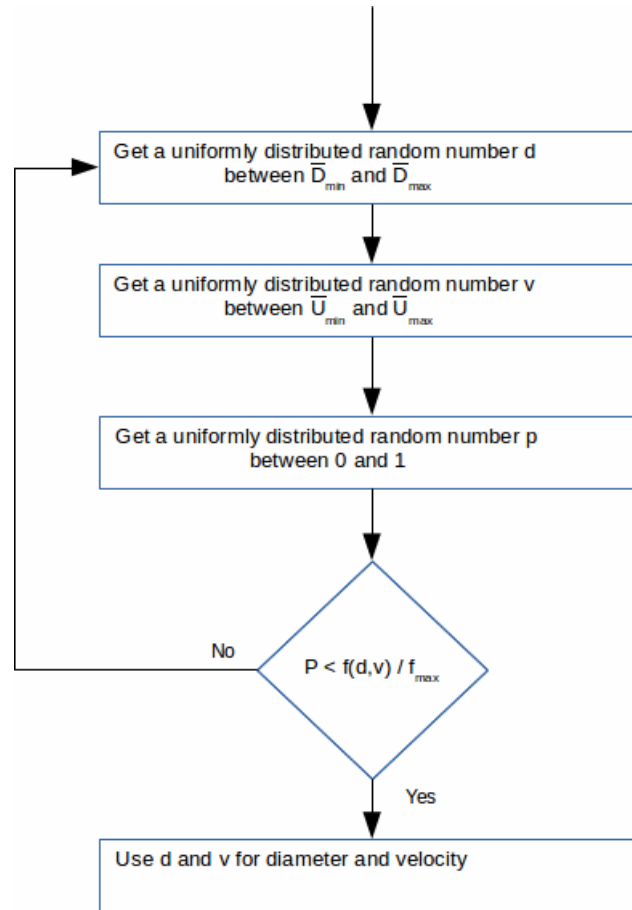


Fig. 4.1.: Flow chart of acceptance-rejection algorithm applied to joint diameter-velocity probability distribution $f(\bar{D}, \bar{U})$

4.4.2. Creating the Parcels

Like in the class `ConeNozzleInjection`, spheric parcels representing the drops of a spray are created. Starting at a defined injection time, a certain number of parcels will be added to the cloud until the specified injection time has expired. These parcels are provided with certain properties like size, position, velocity (the latter two are vectors). At each time step, first a valid random vector $\vec{x} = (\bar{D}, \bar{U})^T$ is being created by the acceptance-rejection function. This yields the diameter and the magnitude of the velocity for the parcel.

4.4.2.1. Initial Position and Velocity

Next, the initial position \vec{s}_b and velocity \vec{u}_i of the parcel is identified. From the configuration parameters the orifice diameter d , the normed vector in axial direction \vec{a} and the orifice position \vec{z} are known (Fig. 4.2).

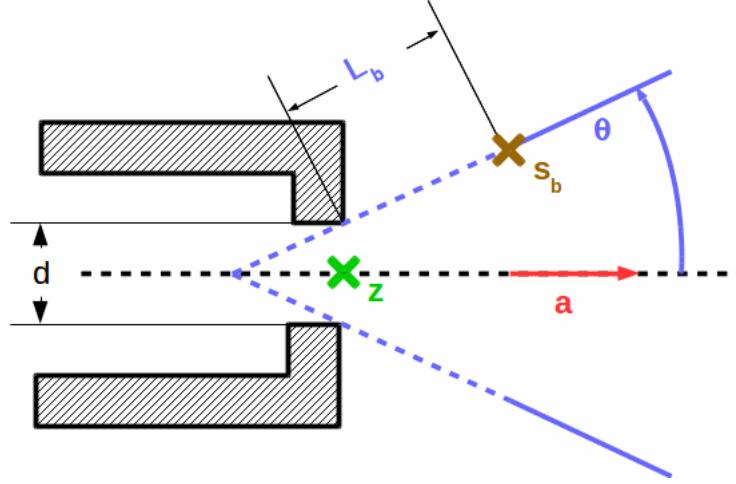


Fig. 4.2.: *The initial position of the parcels representing the drops is at the breakup point, L_b away from the nozzle exit along the spray cone with spray angle θ .*

Although a single drop break up from the liquid sheet later at L_b , it starts -as a part of the liquid sheet- its travel at a certain point $\vec{z} + \vec{r}$ along the circular edge of the nozzle orifice. The orifice plane is perpendicular to the axial vector \vec{a} so two auxiliary vectors \vec{b} and \vec{c} , perpendicular to \vec{a} and perpendicular to each other are needed to determine the radius vector \vec{r} (Fig. 4.3). \vec{b} can be chosen as $\vec{b} = (a_2 - a_3, a_3 - a_1, a_1 - a_2)^T$ (which is perpendicular to \vec{a} , as $\vec{a} \cdot \vec{b} = 0$). Then \vec{c} can easily be found by $\vec{c} = \vec{a} \times \vec{b}$. So \vec{r} can be written as

$$\vec{r} = \frac{d}{2} \left(\frac{\vec{b}}{\|\vec{b}\|} \sin \alpha + \frac{\vec{c}}{\|\vec{c}\|} \cos \alpha \right) \quad (4.1)$$

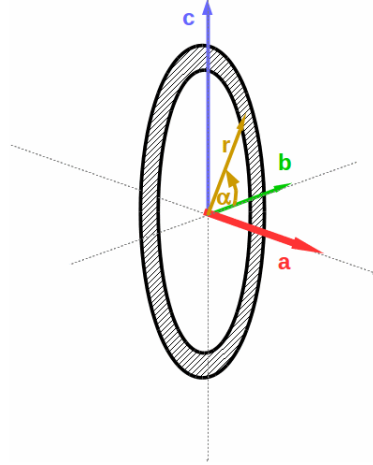


Fig. 4.3.: The radius vector \vec{r} can be constructed by two vectors \vec{b} and \vec{c} , perpendicular to the axial vector \vec{a} and perpendicular to each other. The radial component α of the initial position of the liquid sheet is determined by a random number $0 \leq \alpha < 2\pi$.

where the angle α of the initial position of the parcel along this circle is determined by a a random number $0 \leq \alpha < 2\pi$. The velocity vector \vec{u}_i of the liquid sheet can be separated into a vector \vec{u}_{ax} in axial direction and a vector \vec{u}_{tan} in tangential direction as shown in Fig. 4.4.

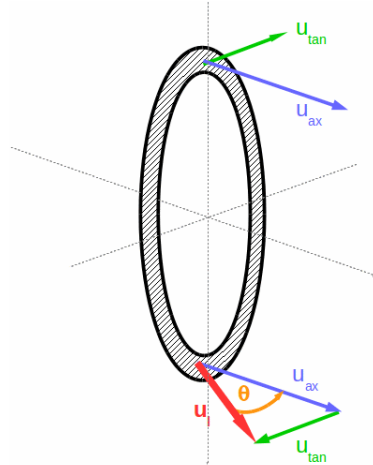


Fig. 4.4.: The initial velocity \vec{u}_i is the result of the velocity component in axial direction \vec{u}_{ax} and the tangential component \vec{u}_{tan} which is caused by the swirl of the liquid. (Its magnitude U_l is specified in the setup parameters).

The magnitude of these components can be calculated by the setup parameter U_l :

$$\| \vec{u}_{ax} \| = U_l \cos \theta \quad (4.2)$$

$$\| \vec{u}_{tan} \| = U_l \sin \theta \quad (4.3)$$

The direction of \vec{u}_{tan} is perpendicular to \vec{a} and \vec{r} :

$$\frac{\vec{u}_{tan}}{\| \vec{u}_{tan} \|} = -\vec{b} \sin \alpha + \vec{c} \cos \alpha \quad (4.4)$$

so the sum of both vectors becomes

$$\vec{u}_l = \vec{u}_{tan} + \vec{u}_{ax} = U_l \left[a \cos \theta + \sin \theta \left(-\vec{b} \sin \alpha + \vec{c} \cos \alpha \right) \right] \quad (4.5)$$

Finally the point where the drop evolves from the liquid sheet, \vec{s}_b is the starting vector \vec{s} at the nozzle orifice can plus breakup length in direction of the velocity:

$$\vec{s}_b = \vec{z} + \vec{r} + L_b \frac{\vec{u}_l}{U_l} \quad (4.6)$$

The whole sequence of generating the drops as implemented in the class “SwirlNozzleInjection” is illustrated in Fig. 4.5.

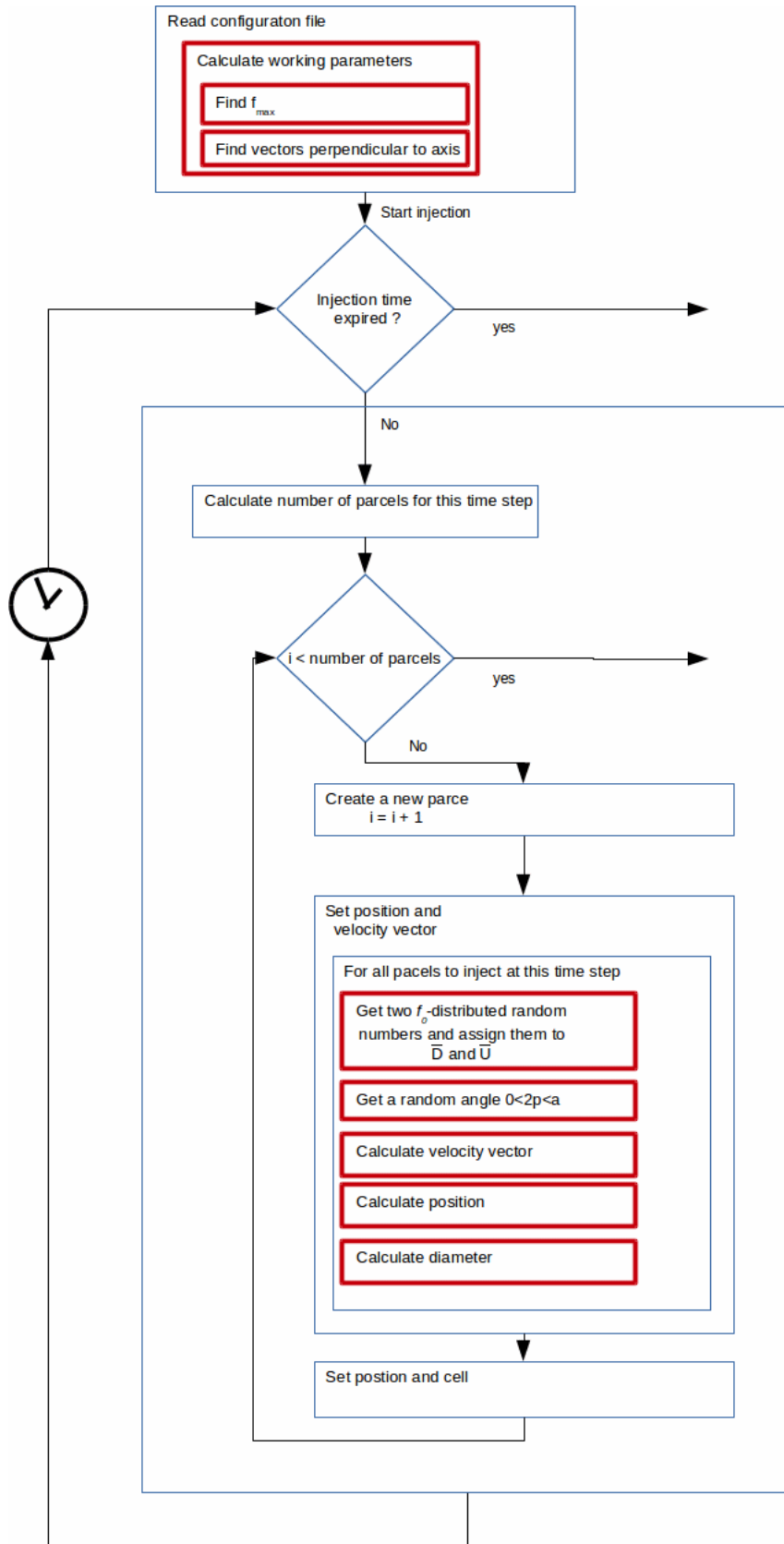


Fig. 4.5.: Flow chart of class “SwirlNozzleInjection”. The boxes with the red frame denote the code that is different to the standard class “ConeNozzleInjection”.

4.4.2.2. Number of Parcels

The number of parcels added to the cloud at a time step is determined by the parameter “ParcelsPerSecond” which can be calculated by

$$ParcelsPerSecond = \frac{6\dot{V}_l}{D_{30}^3\pi} \quad (4.7)$$

where \dot{V}_l is the flow rate and D_{30} is the mean volume diameter. The total number for all parcels created within a time step is $\text{floor}(ParcelsPerSecond \cdot \Delta t)$ where Δt is the time step width of the simulation which is adapted by the solver depending on the Courant number. It is obvious that only whole numbers of drops can be created in a time step. However, the resulting flow rate \tilde{V}_l will always be smaller than the target flow rate \dot{V}_l . The smaller Δt becomes, the higher the difference of the actual flow rate to the target flow rate². This fact has to be considered when analyzing the simulation data.

4.5. Parameters for the Injection Model

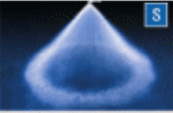
With the implementation of the class SwirlNozzleInjection, relevant nozzle types can be evaluated with regard to the absorption performance of the spray they are producing. The next task now is to find the required setup parameters for the simulation model based on the values in the nozzle data sheets.

4.5.1. Selection of Proper Nozzles

The fix parameters in this work are the volume flow rate of the working fluid $\dot{V}_0 = 2.448 \frac{l}{min}$ and the injection pressure range of $p_{inj} < 18 \text{ bar}$. In the data sheets of Spraying Systems Co.® [1] (Fig. 4.6), twelve swirl nozzles were found with a specified pressure and flow rate within this range.

²In the simulations conducted for this thesis, the resulting flow rate was about $\tilde{V}_l \approx 3 \cdot 10^5 \frac{m^3}{s}$.

4.5 Parameters for the Injection Model

PERFORMANCE DATA: STANDARD ANGLE SPRAY																		
Inlet Conn. (in.)	Nozzle Type		Capacity Size	Inlet Dia. Nom. (in.)	Orifice Dia. Nom. (in.)	Flow Rate Capacity (gallons per minute)										Spray Angle (°)		
	AX	BX				3 psi	5 psi	10 psi	15 psi	20 psi	30 psi	40 psi	60 psi	80 psi	100 psi	10 psi	20 psi	80 psi
1/8	•	•	.5	.031	.047	–	–	.05	.06	.07	.09	.10	.12	.14	.16	.39	58	68
	•	•	1	.063	.063	–	–	.10	.12	.14	.17	.20	.24	.28	.32	41	64	76
	•	•	2	.078	.078	–	.14	.20	.24	.28	.35	.40	.48	.57	.63	52	81	88
	•	•	3	.094	.094	–	.21	.30	.37	.42	.52	.60	.73	.85	.95	52	64	77
	•	•	5	.125	.125	.27	.35	.50	.61	.71	.87	1.0	1.2	1.4	1.6	56	67	76
	•	•	8	.158	.158	.44	.57	.80	.98	1.1	1.4	1.8	2.0	2.3	2.5	58	85	70
	•	•	10	.172	.172	.55	.71	1.0	1.2	1.4	1.7	2.0	2.4	2.8	3.2	55	85	72


PERFORMANCE DATA: WIDE ANGLE SPRAY																		
Inlet Conn. (in.)	Nozzle Type		Capacity Size	Inlet Dia. Nom. (in.)	Orifice Dia. Nom. (in.)	Flow Rate Capacity (gallons per minute)										Spray Angle (°)		
	AX-W	BX-W				5 psi	7 psi	10 psi	15 psi	20 psi	30 psi	40 psi	60 psi	80 psi	10 psi	20 psi	80 psi	
1/0	•	•	0.5-0.5W	.031	.047	–	–	.05	.06	.07	.09	.10	.12	.14	103	117	98	
	•	•	1-1W	.063	.063	–	–	.10	.12	.14	.17	.20	.25	.28	110	125	110	
	•	•	2-3W	.078	.109	–	.21	.25	.31	.35	.43	.50	.61	.71	114	114	97	
	•	•	3-3W	.094	.109	–	.25	.30	.37	.42	.52	.60	.73	.85	114	114	97	
	•	•	3-5W	.094	.125	–	.29	.34	.42	.48	.59	.68	.80	.96	116	110	95	
	•	•	2-10W	.078	.172	–	.36	.41	.51	.59	.72	.82	1.0	1.2	130	135	120	
	•	•	5-5W	.125	.125	–	.42	.50	.61	.71	.86	1.0	1.2	1.4	116	110	92	
	•	•	5-10W	.125	.172	.46	.54	.65	.80	.92	1.1	1.3	1.6	1.8	128	121	95	
	•	•	8-10W	.158	.172	.64	.75	.90	1.1	1.3	1.6	1.8	2.2	2.5	124	112	90	
	•	•	1-1W	.063	.063	–	–	.10	.12	.14	.17	.20	.25	.28	110	117	111	

Fig. 4.6.: Excerpt of nozzle data sheet from Spraying Systems Co.[®] [1]. The orange circles mark operating points close to the target value of $\dot{V}_0 = 2.448 \frac{l}{min} = 0.645 \frac{gal}{min}$.

4.5.2. Conversion of Manufacturer's Data to the Designed Operating Point for p and θ

For most of the nozzles, volume flow rate and injection pressure are related as follows:

$$\frac{\dot{V}_1}{\dot{V}_2} = \left(\frac{p_1}{p_2} \right)^y \quad (4.8)$$

Where the flow exponent y depends on the nozzle type. According to Spraying Systems Co.[®] [1], $y = \frac{1}{2}$ for any type of hollow cone nozzles. In order to get the

required volume flow rate \dot{V}_0 , the injection pressure p_0 must be applied where

$$p_0 = p_{Data} \left(\frac{\dot{V}_0}{\dot{V}_{Data}} \right)^2 \quad (4.9)$$

and p_{Data} and \dot{V}_{Data} are the specified parameters from the data sheet.

The spray angle θ depends on the injection pressure but also on the inner nozzle dimensions and surface properties of the coating of the swirl chamber. So far, there only exist extensive numerical methods for a satisfying ab-initio-prediction of a swirl nozzle's spray angle (e.g. [9], [2]).

As in the data sheet the full spray cone angle $2\theta_{Data1,2,3}$ (which is twice the angle drawn by the liquid sheet and the spray axis) for each nozzle is specified at three different pressure values $p_{Data1,2,3}$, the resulting spray angle θ_0 at p_0 could at least be approximated by linear interpolation:

$$\theta_0 = \theta_{Data1} + \frac{\theta_{Data2} - \theta_{Data1}}{p_{Data2} - p_{Data1}} (P_0 - P_{Data1}) \quad (4.10)$$

where $p_{Data1} \leq p_0 \leq p_{Data2}$.

The results for the selected nozzles are listed in Tab. 4.1.

Type designation	p_0 [$10^5 Pa$]	θ_0 [deg]	r_0 [$10^{-3}m$]
AX-1/8-2	7.22	36.14	0.99
AX-1/8-3	3.18	34.83	1.19
AX-1/8-5	1.15	31.71	1.59
AX-1/8-8	0.44	26.38	1.98
AX-1/8-10	0.28	24.56	2.18
AX-W-1/8-2-3	4.62	50.34	1.38
AX-W-1/8-3-3	3.18	53.29	1.38
AX-W-1/8-3-5	2.47	53.02	1.59
AX-W-1/8-2-10	1.65	67.02	2.18
AX-W-1/8-5-5	1.15	55.98	1.59
AX-W-1/8-5-10	0.68	63.04	2.18
AX-W-1/8-8-10	0.35	64.96	2.18

Tab. 4.1.: Operating points of the selected nozzles at the target flow rate \dot{V}_0

4.5.3. Sheet Thickness

For calculation of the thickness of the liquid sheet t_s at the nozzle orifice LEFEBVRE [22] lists several formulas (mostly semi-theoretically derived, then fitted to experimental data with proper coefficients). In this work we use the latest (and best matching) of these formulas:

$$t_s = 2.7 \left(\frac{2r_0 \dot{V}_0 \mu_l}{p_0} \right)^{0.25} \quad (4.11)$$

4.5.4. Sheet and Swirl velocity

The velocity component of the liquid sheet along the spray axis $U_{0\perp}$ is equal to the flow rate divided by the intersection of the liquid sheet with the orifice plane. To get the velocity in the direction the spray cone U_0 , finally divide by $\cos\theta$:

$$U_{0\perp} = \frac{\dot{V}_0}{\pi [r_0^2 - (r_0 - t_s)^2]} \quad (4.12)$$

$$U_0 = \frac{\dot{V}_0}{\pi [r_0^2 - (r_0 - t_s)^2] \cos\theta} \quad (4.13)$$

The swirl velocity A_0 (the cause of the spray angle) is the angular velocity of the liquid sheet among the spray axis at the orifice. A volume element of the liquid sheet moves by $U_{0\perp} dt$ in axial direction while it moves by $A_0 r_0 dt$ in perpendicular direction. The resulting trajectory of this volume element draws the angle of θ with the spray axis. So A_0 can be described as

$$A_0 = \frac{U_0 \sin\theta}{r_0} = \frac{\dot{V}_0}{r_0 \pi [r_0^2 - (r_0 - t_s)^2]} \tan\theta \quad (4.14)$$

4.5.5. Breakup Length

The breakup length L_b describes the distance of the region where droplets form from the liquid sheet to the orifice. Like for the sheet thickness, several empirical formulas can be found in literature. In contrast to the formulas given by LEFEBVRE [22] which are applicable for all kind of liquid sheets, ASHGRIZ [4] suggested an

equation adapted to swirl nozzle properties (e.g. the spray angle) which was used in this work:

$$L_b = 3 \left(\frac{2r_0 \rho_l \sigma t_s}{\rho_l^2 U_0^2 \tan \theta} \right)^{\frac{1}{3}} \quad (4.15)$$

4.5.6. Reynolds and Weber Number

The Reynolds number Re expresses the ratio of inertial forces to viscous forces acting on an object moving through a fluid.

$$Re = \frac{\rho u L}{\mu} \quad (4.16)$$

where ρ is the density of the fluid, u is the relative velocity of the object in the fluid, μ is the dynamic viscosity of the fluid and L is the characteristic length of the object.

In case of a liquid, cone-shaped sheet, L is considered equal to the sheet thickness t_s [39]. So Re becomes

$$Re = \frac{\rho_g U_0 t_s}{\mu_g} \quad (4.17)$$

The Weber number We is proportional to the ratio of kinetic energy to surface energy on the interface between two fluids (a liquid and a gas).

$$We = \frac{\rho u^2 L}{\sigma} \quad (4.18)$$

where ρ is the density of the gas, u is the relative velocity of liquid and gas, σ is the surface tension of the fluid and L is the characteristic length of the fluid object. Similar to Re , YAN [39] expresses We for a liquid sheet like this

$$We = \frac{\rho_g U_0^2 t_s}{\sigma} \quad (4.19)$$

4.5.7. Mean Droplet Diameter

LEFEBVRE [22] gives an empirical formula for estimating the Sauter Mean Diameter of a drop produced by a swirl nozzle:

$$D_{32} = 4.52 \left(\frac{\sigma \mu_l^2 t_s \cos \theta}{\rho_g \Delta p^2} \right)^{0.25} + 0.39 \left(\frac{\sigma \rho_l}{\rho_g \Delta p} \right)^{0.25} (t_s \cos \theta)^{0.75} \quad (4.20)$$

where Δp denotes the difference between injection pressure and the ambient pressure.

However, for the distribution function gained by the MEF, the mean volume diameter D_{30} is needed. A useful formula to convert different mean drop diameters can be found in DUMOUCHEL [10]:

$$D_{ab} = \nu^{\frac{1}{\nu}} D_{\nu 0} \left(\frac{\Gamma\left(\frac{1+a}{\nu}\right)}{\Gamma\left(\frac{1+b}{\nu}\right)} \right)^{\frac{1}{a-b}} \quad (4.21)$$

Applied for $a = 3$, $b = 2$ and $\nu = 3$ and solved for D_{30} yields:

$$D_{30} = 0.776 \cdot D_{32} \quad (4.22)$$

4.5.8. Source Terms for the MEF

First some of the characterizing parameters of the spray have to be transformed into dimensionless quantities, as the MEF operates only with dimensionless terms. For swirl nozzles, YAN [40, 39] defines the dimensionless velocity U_l^* of the liquid sheet as a function of the original (dimensional) sheet velocity U_l (eqn. 4.13), the orifice radius r_0 , the swirl velocity A_0 (eqn. 4.14) and the sheet thickness t_s (eqn.4.11):

$$U_l^* = \sqrt{1 + \frac{A_0 t_s}{U_l} \left(\frac{r_0 - t_s}{t_s} + \frac{1}{2} \right)^2} \quad (4.23)$$

Instead of the densities ρ_g and ρ_l of the gaseous and liquid medium, the ratio of both is used for the source terms:

$$\varrho = \frac{\rho_g}{\rho_l} \quad (4.24)$$

Two more parameters used by YAN are the swirl strength S_0 , defined as

$$S_0 = 2\pi \left(2 \frac{r_0 - t_s}{t_s} + 1 \right) L_b \quad (4.25)$$

and the drag coefficient C_d

$$C_d = \frac{1.328}{\sqrt{Re}} \quad (4.26)$$

With this dimensionless quantities, the equations for the source terms result as:

$$S_m = 0 \quad (4.27)$$

$$S_{mv} = \rho C_d U_l^{*2} \quad (4.28)$$

$$S_e = \frac{1}{2} \rho C_d S_0 U_l^{*3} \quad (4.29)$$

4.5.9. Lagrangian Multipliers

The calculations described in this section were conducted for the selected nozzles. The resulting characteristic values at target flow rate are listed in Tab. 4.2. These characteristic values and the prior distribution function $f_0(\bar{D})$ from eqn. 3.32 and eqn. 3.6 are necessary to set up the Lagrangian function \mathcal{L} , whose solution is the set of Lagrangian multipliers $\Lambda_{0,1,2,3}$, which determines the joint diameter-velocity distribution function $f(\bar{D}, \bar{U})$.

To obtain the Lagrangian multipliers from the product data sheet, a program in Scilab (find source code in Appendix B) was made that subsequently conducts the following operations:

1. Read the relevant product sheet data P_{Data} , \dot{V}_{Data} , r_0 and θ_{Data}
2. Calculate P_0 and θ_0
3. Calculate t_s , U_0 and L_b

4. Calculate We and Re
5. Calculate D_{32} and D_{30}
6. Calculate dimensionless parameters for source terms
7. Calculate source terms
8. Find parameters for prior distribution function f_0 (i.e. b and \bar{D}_{cr})
9. Define prior distribution function f_0
10. Define Lagrangian function
11. Solve for Lagrangian multipliers $\Lambda_{0,1,2,3}$

The parameters for all twelve selected nozzles are listed in Tab. A.2 and Tab. A.3.

Tab. 4.2.: *Characteristic values for the selected nozzles at target flow rate*

Type designation	t_s [μm]	U_0 [$\frac{m}{s}$]	Re	We	D_{32} [μm]	D_{30} [μm]
AX-1/8-2	262	35.6	762	6.22	72	56
AX-1/8-3	337	22.8	628	3.29	109	85
AX-1/8-5	467	12.0	459	1.27	186	145
AX-1/8-8	628	6.9	354	0.56	311	241
AX-1/8-10	718	5.4	318	0.40	390	303
AX-W-1/8-2-3	293	41.0	982	9.24	75	58
AX-W-1/8-3-3	337	31.3	863	6.21	88	68
AX-W-1/8-3-5	359	29.5	867	5.88	99	77
AX-W-1/8-2-10	380	54.5	1691	21.17	87	68
AX-W-1/8-5-5	467	18.3	698	2.93	140	109
AX-W-1/8-5-10	533	20.3	883	4.11	156	121
AX-W-1/8-8-10	665	14.0	758	2.43	210	163

4.5.10. Results for the Joint Diameter-Velocity Distribution

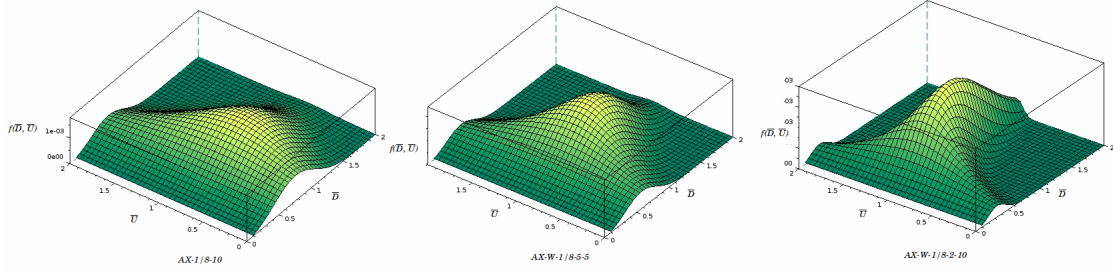


Fig. 4.7.: *Examples for the joint diameter-velocity distribution function $f(\bar{D}, \bar{U})$ calculated for three different nozzles. The mean diameter of the drops produced by the nozzles decreases from left to right, while the mean velocity increases.*

Using the Scilab program, the Lagrangian multipliers have been identified for all of the selected nozzles. In Fig.4.7, the graphs for three of them are shown. Nozzle AX-1/8-10 left hand side, is the one that produces the slowest ($U_0 = 5.4 \frac{m}{s}$) and largest ($D_{32} = 390 \mu m$) drops while AX-W-1/8-2-10 right hand side generates the fastest ($U_0 = 54.5 \frac{m}{s}$) and quite small ($D_{32} = 87 \mu m$) drops. AX-W-1/8-5-5 in the middle represents the average nozzle ($U_0 = 18.3 \frac{m}{s}$ and $D_{32} = 140 \mu m$). Apparently the variance for the velocity decreases with a rising mean value, which can hardly be seen for the diameter.

4.5.11. Validation

As no experimental data for the selected nozzles are available, it is hard to verify the parameters obtained by above algorithm. Explicit values for $\Lambda_{0,1,2,3}$ are only found at MITRA [24], however the nozzles and their operating points differ too much from the parameters in this thesis. Nevertheless, MITRA mentions in the same work an helpful criterion:

“Generally, it is observed that the converged solution of the Lagrangian multipliers for realistic droplet size distribution satisfies the following relations: $\Lambda_1 > 0$, $\Lambda_3 > 0$, $\Lambda_1 + \Lambda_3 > |\Lambda_2|$ and $\Lambda_2 < 0$.” [24]

At least above observation can be confirmed by all $\Lambda_{1,2,3}$ in Tab. A.2 and Tab. A.3.

5. Conduction of Simulation Experiments

5.1. Simulation Setup and Boundary Conditions

5.1.1. Dimension of Absorber Chamber

As mentioned in the introduction, the dimensions of the absorber chamber is supposed to be as small as possible in order to keep costs and required space of the system at minimum. In practice, the absorption chamber is of cylindrical shape. The spray nozzle is mounted in center of top. The minimum chamber size allows the drops to move a distance s in which they absorb most of the ammonia. As can be seen in Fig. 5.1, the height of the chamber results in $h = s \cos \theta$ and its radius $r = s \sin \theta$

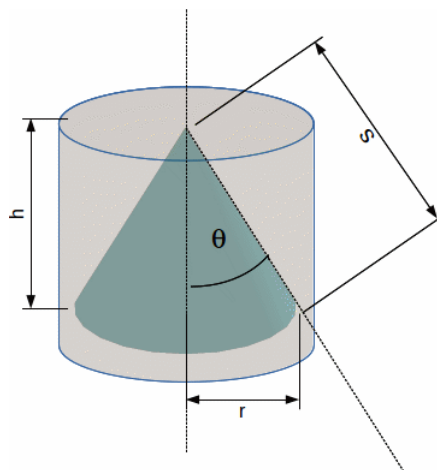


Fig. 5.1.: *The minimum chamber dimensions allow the drops to move distance s in which they absorb most of the ammonia*

5.1.2. Interaction of Drops with Fluid

As already mentioned, the selected nozzles produce up to 80 million drops per second at the required operating point. This would mean for the simulation that for an average life time of a drop of 1.5 seconds, the interactions of 120 million drops with the fluid had to be calculated at each step in OpenFOAM which is beyond all available computational resources. A remedy for this problem is to work with only a small, representative fraction of the total amount of drops. However, it must be ensured that these few drops have the same effect on the fluid as the 120 million drops would have. For this, OpenFOAM provides a parameter named “nParticle” which is used for all interactions between drop and fluid. For each drop the temperature, momentum and mass transfer into the fluid is multiplied by nParticle. In the simulations conducted for this work, nParticle was set to 10000.

5.1.3. Cell Size

In numerical simulation methods like FEM or FVM, smaller cell size means more accurate results. Usually, only the associated increase of computational power determines the minimum cell size. However, in a combination of a fluid phase and discrete parcels like in our case the cell must at least be as big as the containing parcel. If one parcel represents nParticles as described above, the volume of a parcel must exceed the overall volume of nParticles. Inconsistent results in the interaction of parcels and fluid may arise otherwise. For a drop diameter $D = 150 \mu m$, the required volume for $nParticles = 10000$ is $V = \frac{1}{6} \cdot nParticle \cdot D^3 \pi = 1.767 \cdot 10^{-8} m^3$, so the edge length for a cubic cell must be greater than $2.6 mm$. Fig. 5.2 shows the mesh for an absorption chamber of $r = 0.28 m$ and $h = 0.12 m$. The edge length is found in the range of $1 cm$.

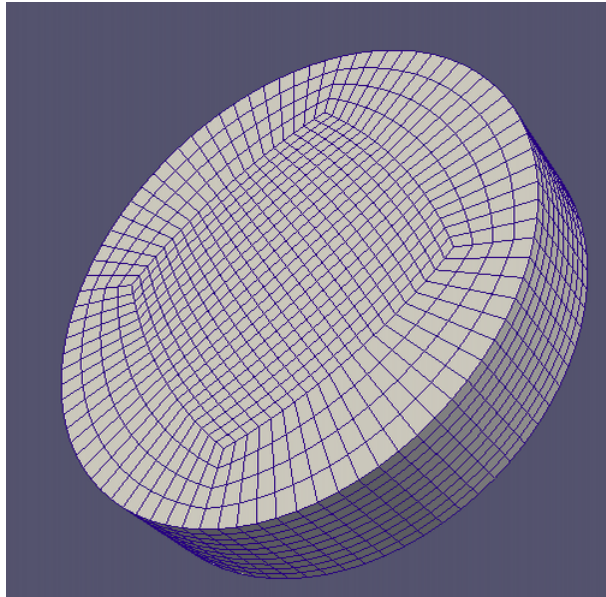


Fig. 5.2.: Mesh for an absorption chamber of $r = 0.28\text{ m}$ and $h = 0.12\text{ m}$

5.1.4. Laminar or Turbulent Flow

If turbulent flow may occur among the spheric drops, the drag force acting on the drop and also heat and mass transfer have to be described by different models than in the laminar case. The calculation of turbulent flow requires quite small meshes which would raise the required computational power. In literature, flow around a spheric body is assumed (mostly) laminar as long as $Re < 300$ [18]. Calculating the Reynolds number according to eqn. 4.16, using the parameters for the selected nozzles in Tab. A.2 and Tab. A.3, yields Reynolds numbers (for average diameter and velocity values) of $133 < Re < 301$. this means that laminar flow can be assumed for most of the drops, therefore no turbulence model was used in the simulations.

5.1.5. Boundary Conditions and Simplifications

For all the mentioned simulations in this chapter, the following boundary conditions (also listed in Tab. 5.1) and simplifications are assumed :

- Gaseous material transfer into or from the absorber chamber only occurs through the inlet patch, which is a part of the bottom surface area.
- A drop touching the chamber walls “escapes” from the simulation. Its mass, momentum and energy vanish from the system.

- The amount of ammonia flowing into the chamber is equal to the amount of ammonia being absorbed by the drops. This is ensured by setting the pressure at the inlet to constant $p = 200000 \text{ Pa}$.
- The ammonia concentration at the inlet is set to constant $x = 0.99 \frac{\text{kg}}{\text{kg}}$.
- All the heat energy at the walls can be dissipated. Except for the inlet, the temperature at the walls is constant $T = 300 \text{ K}$.
- No evaporation of the water drops occurs.

	BC for inlet	BC for other walls
p	<i>totalPressure</i> , $p0 = 200000 \text{ Pa}$	<i>zeroGradient</i>
T	<i>zeroGradient</i>	$T = 300 \text{ K}$
U	<i>pressureInletOutletVelocity</i>	(0, 0, 0)
x_{NH_3}	$0.99 \frac{\text{kg}}{\text{kg}}$	<i>zeroGradient</i>

Tab. 5.1.: *Boundary conditions used for the simulations in this thesis.*

5.1.6. Design of Simulation Experiments

Previous estimations in sec. 2.3 have shown that the absorption capability of drops distinctly declines with diameters larger than $D_{30} > 100 \mu\text{m}$. Because of this, only two nozzle types which produce quite small drop diameters (i.e. $67.5 \mu\text{m}$ and $84.5 \mu\text{m}$) were used for the simulated scenarios. The chamber dimensions were adapted to the spray angle, like described in sec. 5.1.1 for scenario 2 (see Tab. 5.2) and 3. In a sort of “cross-check”, scenario 1 uses nozzle AX-W-1/8-2-10 while the chamber dimensions are those for nozzle AX-1/8-3. Scenario 4 is same as 3 but a 1.5 times larger chamber (in both radius and height). Similarly, scenario 5 is same as 2, but again with a 1.5 times larger chamber.

<i>Scenario</i>	<i>Nozzle</i>	<i>surfaceMassTransferModel</i>	Drop parameter		Chamber dimensions		
			$D_{30} [\mu\text{m}]$	$U_0 [\frac{\text{m}}{\text{s}}]$	$r [\text{m}]$	$h [\text{m}]$	$A [\text{m}^2]$
1	AX-W-1/8-2-10	liquidControlledFlux	67.5	54.5	0.35	0.5	1.87
2	AX-1/8-3	liquidControlledFlux	84.5	22.8	0.35	0.5	1.87
3	AX-W-1/8-2-10	liquidControlledFlux	67.5	54.5	0.28	0.12	0.70
4	AX-W-1/8-2-10	liquidControlledFlux	67.5	54.5	0.42	0.18	1.58
5	AX-1/8-3	liquidControlledFlux	84.5	22.8	0.525	0.75	4.21

Tab. 5.2.: *Setup of simulations.*

5.2. Analysis and Discussion of Simulation Data

5.2.1. Mass Fraction of an Average Drop

In order to find the development of the ammonia concentration in an average drop as a function of distance, the simulated space was divided into spheric shells encasing the nozzle orifice. Within each spheric shell n of radius $[r_n, r_{n+1}]$ first the overall mass $m_{[r_n, r_{n+1}]}$ contained in the drops of mass m_i is calculated:

$$m_{[r_n, r_{n+1}]} = \sum_i m_i \quad | \quad r_n < r_i \leq r_{n+1} \quad (5.1)$$

Next the overall ammonia mass fraction within this spheric shell $x_{[r_n, r_{n+1}]}$ is determined:

$$x_{[r_n, r_{n+1}]} = \frac{\sum_i m_i x_i}{m_{[r_n, r_{n+1}]}} \quad | \quad r_n < r_i \leq r_{n+1} \quad (5.2)$$

The overall mass fractions plotted against the distance for scenario 1 is shown in Fig. 5.3. At the distance of 0.4 m the larger drops whose trajectory is hardly deviated by the flow of the vapor impinge at the chamber wall (see Fig. 5.4). The smaller ones follow the streamlines into the lower part of the chamber and continue absorbing. While the chamber temperature is rising, less heat can dissipate from the drops and less ammonia can be solved in the drops. So the ammonia concentration declines over time.

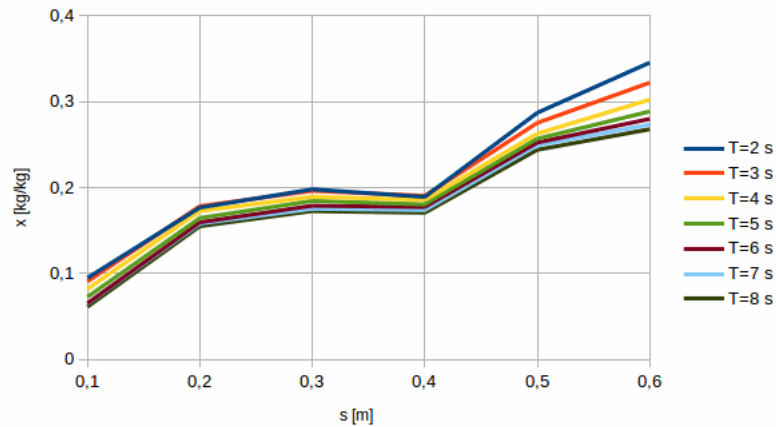


Fig. 5.3.: Ammonia concentration of all drops as a function of their distance from the nozzle, evaluated at different times.

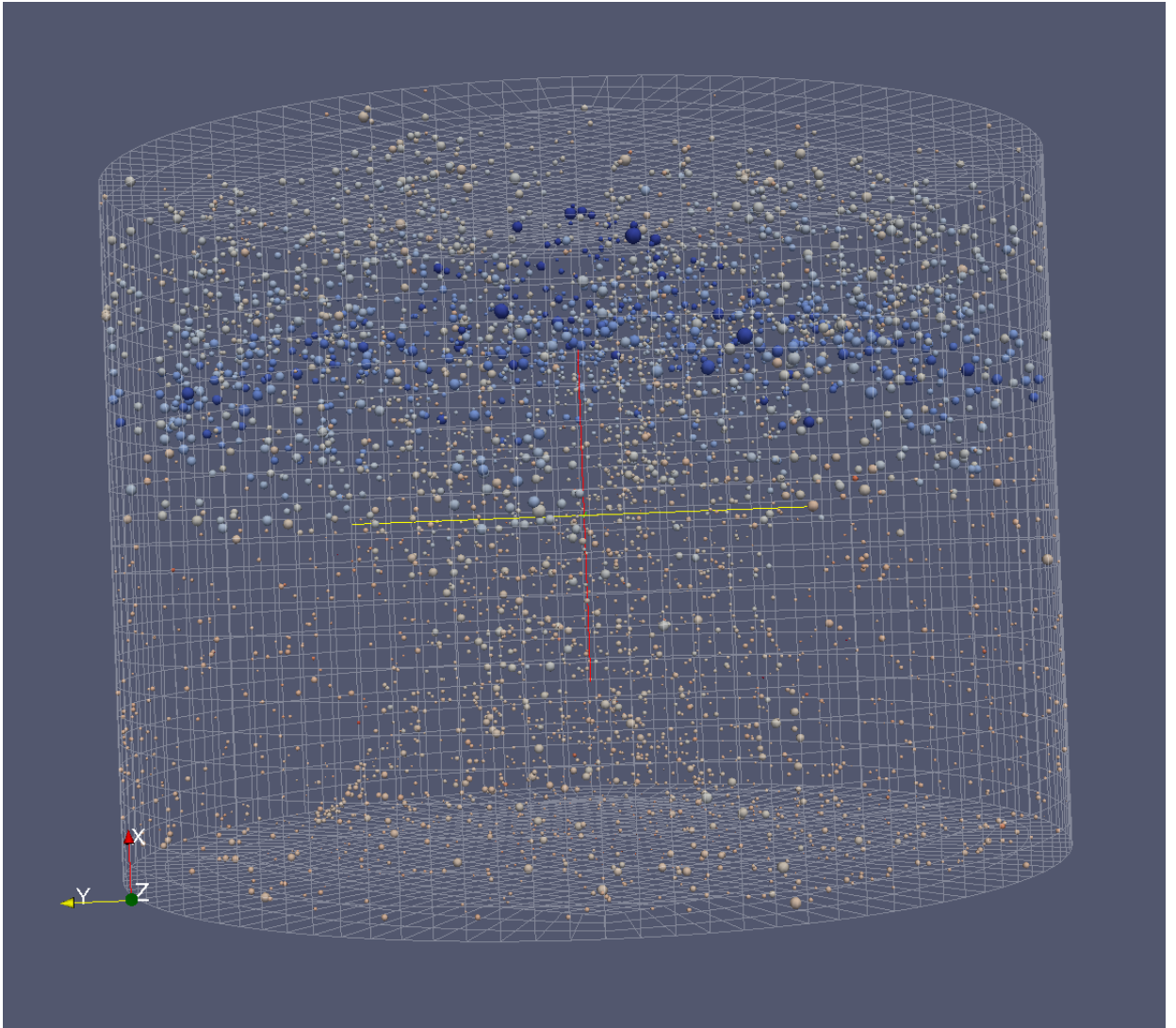


Fig. 5.4.: *Visualization of scenario 1 after 8 seconds. The spheres represent the drops, their color indicates the ammonia concentration (blue = low concentration, red = high concentration).*

5.2.2. Mass Fraction of an Individual Drop

The contribution of individual drops of different sizes on the overall absorption was determined by selecting arbitrary three drops of diameters $D_{1,2,3}$ where $D_1 \approx D_{30}$, $D_2 \approx 0.5 \cdot D_{30}$ and $D_3 \approx 2 \cdot D_{30}$ and tracking them from the breakup point to their impingement on the chamber wall. By tracking both “early” drops, which were generated at the very beginning of the simulation and “late” drops, generated when the system has reached its equilibrium state, one can also see the influence of the

chamber temperature on the absorption, as in Fig. 5.5.

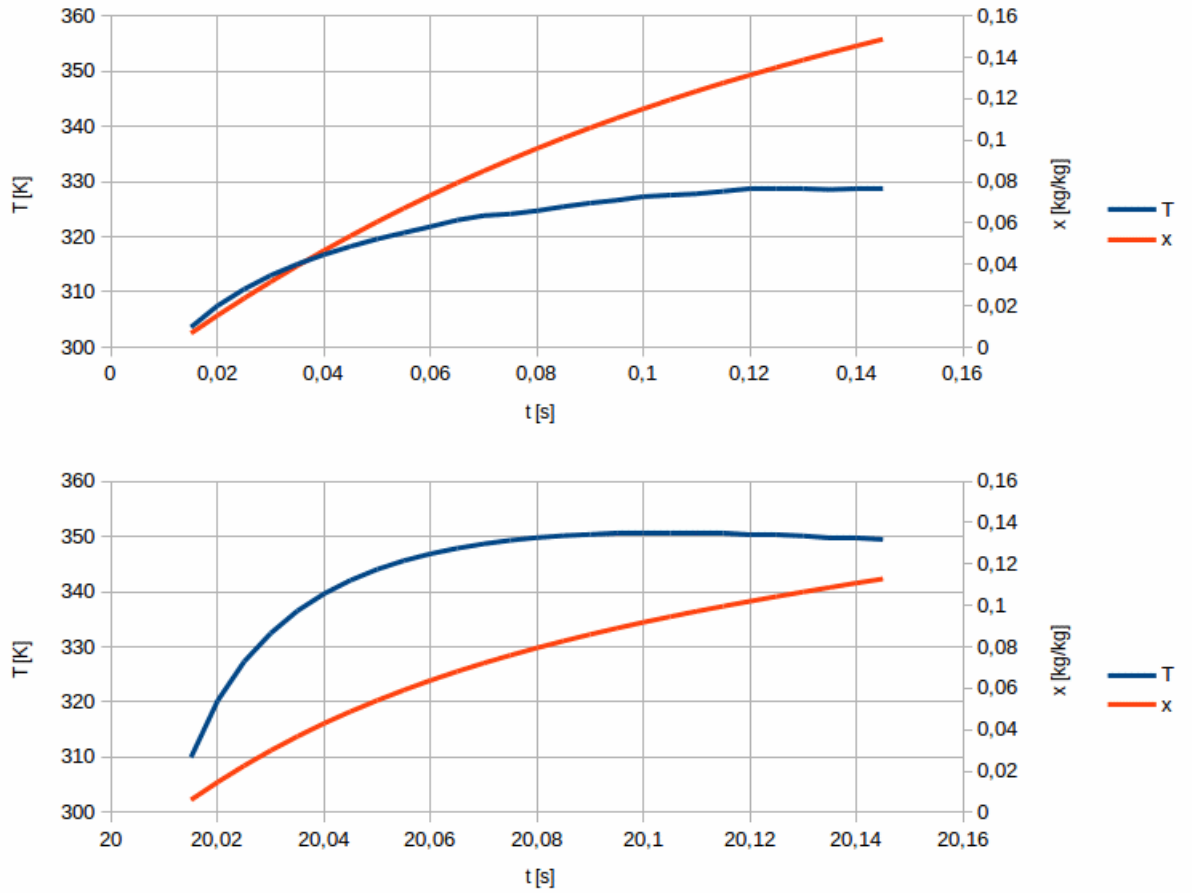


Fig. 5.5.: Drops from scenario 2 of diameter $D \approx D_{30} = 84.5 \mu\text{m}$. The top graph shows the development of temperature and ammonia mass fraction of a drop generated at the beginning of the simulation, the bottom graph shows the same for a drop generated 20 seconds later.

Now let's compare these curves with the prior estimations from sec. 2.3. The saturation concentration curve in sec. 2.3.1 would allow a maximum ammonia mass fraction of about $0.13 \frac{\text{kg}}{\text{kg}}$ at a drop temperature of 328 K . However the top curve in Fig. 5.5 shows a mass fraction of $0.15 \frac{\text{kg}}{\text{kg}}$ at this temperature. Same for the bottom curve: It shows $x = 0.11 \frac{\text{kg}}{\text{kg}}$ at $T = 350 \text{ K}$ while the estimated saturation concentration at this temperature would be below $0.02 \frac{\text{kg}}{\text{kg}}$.

The time dependent behavior of the of the mass fraction looks quite different from the curves calculated on the models from sec. 2.3. Fig. 5.6 shows the calculated evolution of mass fraction for a drop of $D = 84.5 \mu\text{m}$ based on the model from

from sec. 2.3.2 where no heat dissipation is considered. One would expect a similar behavior of the curve from scenario 2 after 20 seconds, where the chamber has heated up and hardly any heat dissipation to the atmosphere occurs. However, the simulated x-curve rises much slower than the calculated one from Fig. 5.6. An explanation could be the the transfer of heat of the initially cool drop from the atmosphere, which reduces the absorption rate.

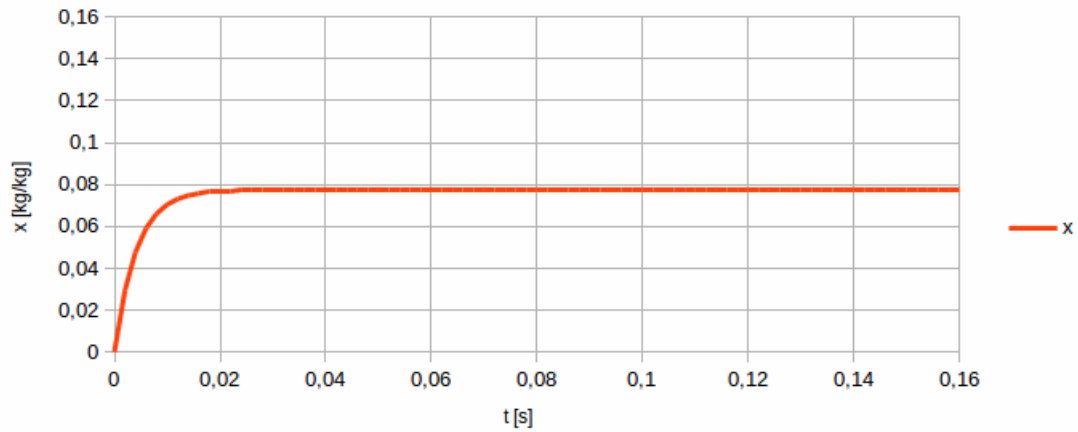


Fig. 5.6.: Drop from scenario 2, calculated on the model from sec. 2.3.2

Analogously, the top curve of Fig. 5.5 from the beginning of the simulation should be similar to the curve calculated on the model from sec. 2.3.4, where heat dissipation is considered. Again the slope of the simulated x-curve is lower than the one from Fig. 5.7, while the T-curve stays longer at high temperature. Apparently the heat dissipation rate from the drop calculated in the simulation is lower than estimated by the model.

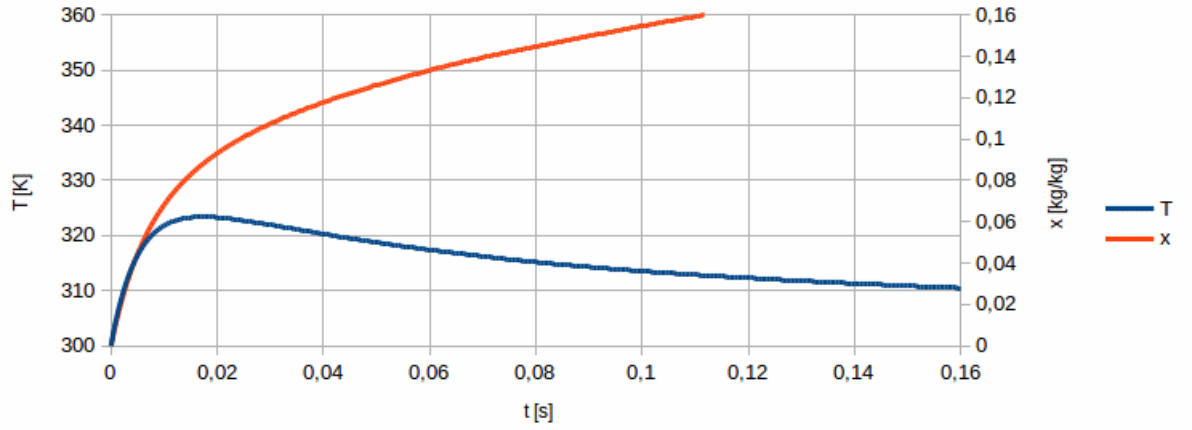


Fig. 5.7.: Drop from scenario 2, calculated on the model from sec. 2.3.4

5.2.3. Absorber Output

The ammonia-water solution leaving the absorber consists of the drops having impinged the chamber walls. So the ammonia mass fraction of the strong solution was determined by summing up, for every time step, the mass all the drops “escaping” from the simulation area

$$\widehat{m} = \sum_i m_i \quad (5.3)$$

and the amount of ammonia they contain

$$\widehat{xm} = \sum_i x_i m_i \quad (5.4)$$

The total mass \widehat{x} fraction of ammonia in the liquid leaving the absorber is then noted by

$$\widehat{x} = \frac{\widehat{xm}}{\widehat{m}} \quad (5.5)$$

Conducting this calculation at every time step yields a curve like in Fig.5.8, a plot from scenario 2. As expected, in the initial phase, when the temperature of the ammonia atmosphere is low, the drops can dissipate the heat arising from the enthalpy of solution. Therefore the ammonia concentration is higher for the first two

seconds, then drops down while the chamber temperature¹ rises and finally stabilizes at the terminal value, in scenario 2 at about $0.09 \frac{kg}{kg}$.

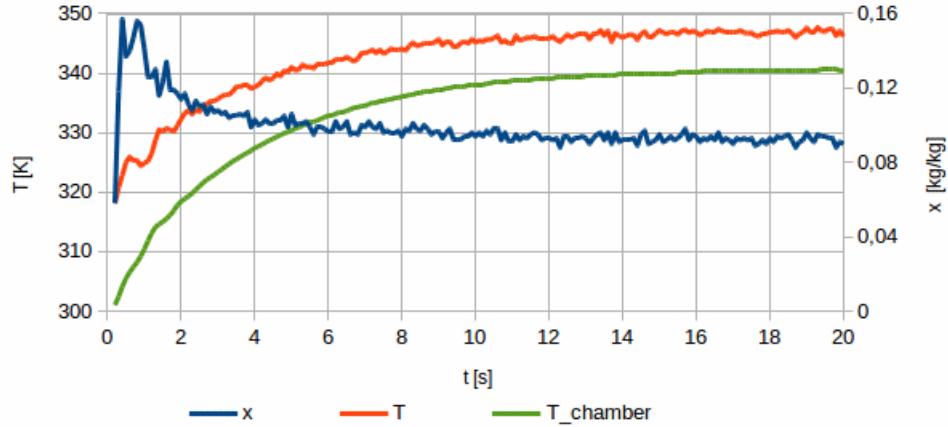


Fig. 5.8.: *Scenario 2: Average ammonia concentration and average temperature of all impinging drops, average chamber temperature as a function of time.*

The terminal values for all simulated scenarios are listed in Tab.5.3. Obviously, higher terminal concentrations can be gained by larger absorption chambers.

Scenario	x [kg/kg]	T_{ch} [K]	T [K]	\dot{Q}_{AB} [W]
1	0.09	338	340	-100
2	0.09	340	347	-110
3	0.04	322	320	-32
4	0.08	335	335	-80
5	0.12	355	355	-110

Tab. 5.3.: *Resulting final ammonia mass fraction, average drop temperature and chamber temperature of the simulated scenarios.*

5.2.4. Lifetime and Mass Fraction of Different Drops

For all drops impinging the chamber wall (at the end of the simulated period), age and diameter was collected and checked for correlation among one another. It can

¹Here, the chamber temperature was determined by summing up the cell temperatures and dividing by the number of cells. This is only valid for approximately equal pressure and volume in the cells.

be seen, that the smaller drops remain longer in the chamber as larger ones. Fig. 5.9 shows the lifetime distribution of the drops in scenario 4. Obviously the small drops are more driven by the flow of the fluid, circulating in the chamber, while large drops keep their initial direction due to their higher momentum.

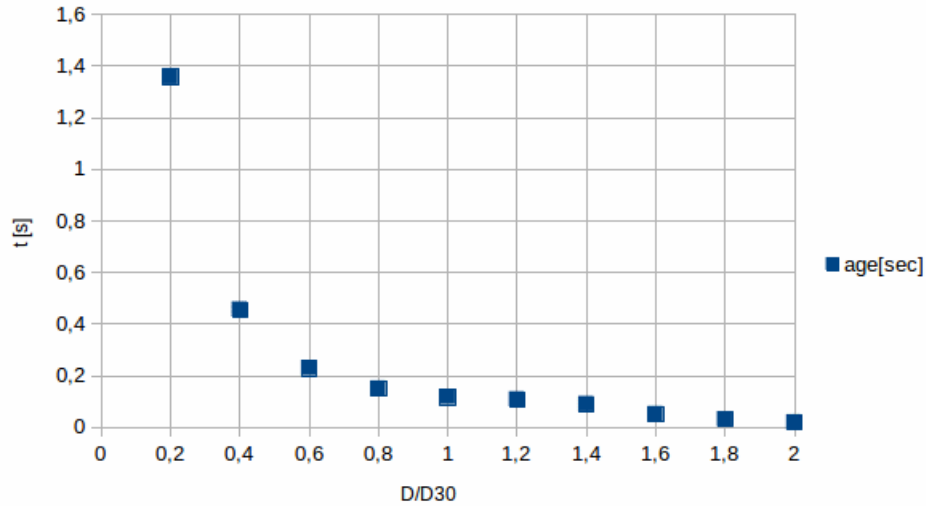


Fig. 5.9.: *Scenario 4: Average lifetime of drops as a function of their diameter*

Both factors, small diameter and long residence time in the chamber support absorption, so the small impinging drops contain a much higher mass fraction of ammonia than the large ones. The dependency of mass fraction on drop diameter and distance from the nozzle exit for scenario 4 can be seen in Fig. 5.10.

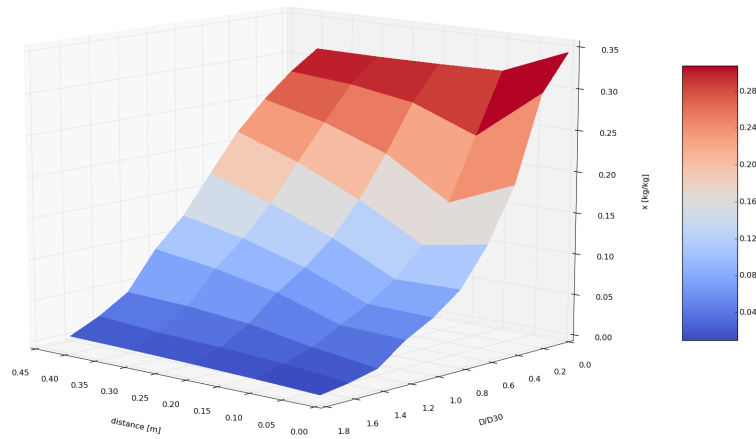


Fig. 5.10.: *Scenario 4: Ammonia mass fraction as a function of distance from the nozzle and of drop diameter x (D, s).*

5.2.5. Fraction of Total Volume as a Function of Drop Diameter

Although the number of the long-living, small drops might be large, their contribution to the total volume of the liquid is still small. In Fig. 5.11, the total volume V_i formed by all escaping drops of diameter $D < D_i$ within a certain period is plotted against $\frac{D_i}{D_{30}}$. Apparently, drops of diameters $D < 0.8D_{30}$ hardly contribute to the total volume. The curve for the mass fraction shows an opposing trend. As expected, high ammonia concentration can only be achieved by small drops.

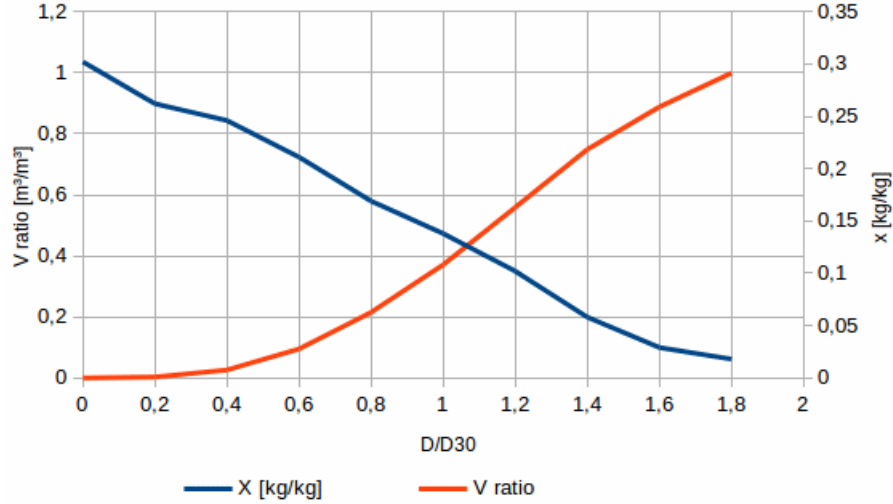


Fig. 5.11.: *Scenario 4: Red: Fraction of total volume formed by drops of diameter smaller than $\bar{D} = \frac{D}{D_{30}}$. Blue: Ammonia mass fraction of amount of liquid formed by drops of diameter smaller than \bar{D} .*

5.2.6. Balance of Energy and Achievable COP

Besides the ammonia concentration in the strong solution, also the heat power produced by absorption P_{abs} is of interest. This heat power consists of the time derivative of the accumulated heat energy of the drops escaping from the absorber $P_{esc} = (T_{AB} - T_{EV}) [(1 - x) c_{p,l} + x c_{p,g}] (\dot{m}_l + \dot{m}_g)$ (see eqn. 1.5) and heat flux through of the absorber walls Φ .

$$P_{abs} = -\frac{x}{1-x} \frac{\dot{m}_l}{M_g} \Delta H_{sol,g} = -\Phi + P_{esc} \quad (5.6)$$

The right part of the sum can be determined directly from the OpenFOAM simulation output, as mass, temperature and ammonia concentration of all drops leaving the chamber at a certain time step is known. For scenario 1 the plot of P_{esc} can be seen in Fig. 5.12

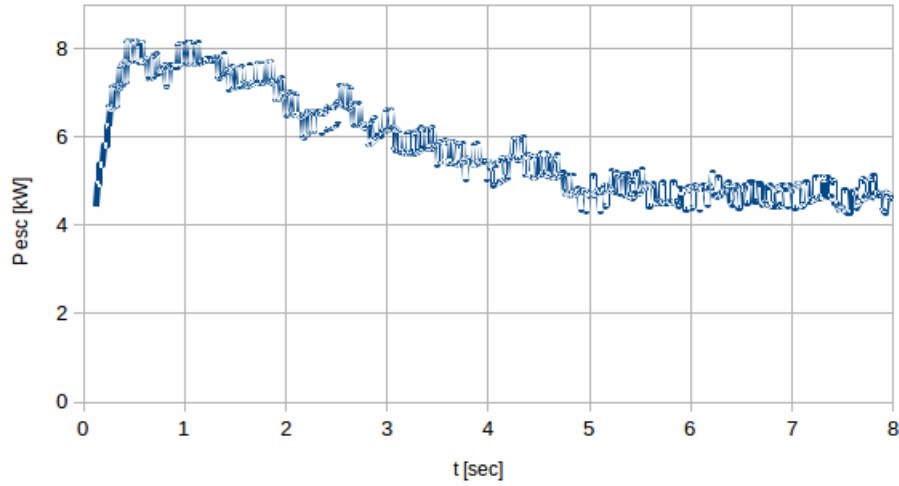


Fig. 5.12.: *Scenario 1: Heat power of all drops escaping from the absorber chamber P_{esc} .*

In a settled state, when number, temperature and mass fraction of the escaping drops stay constant, the total amount of ammonia being solved in water within a time step is equal to the amount of ammonia leaving the absorption chamber within the same time step. So the heat power produced by absorption P_{abs} can be calculated by eqn. 5.6 using the mass fraction x from the strong solution leaving the absorber. P_{abs} calculated this way for scenario 1² can be seen in Fig. 5.13.

²Assuming a constant enthalpy of solution of $\Delta H_{sol,NH_3} = -30.50 \cdot 10^3 \frac{J}{mol}$

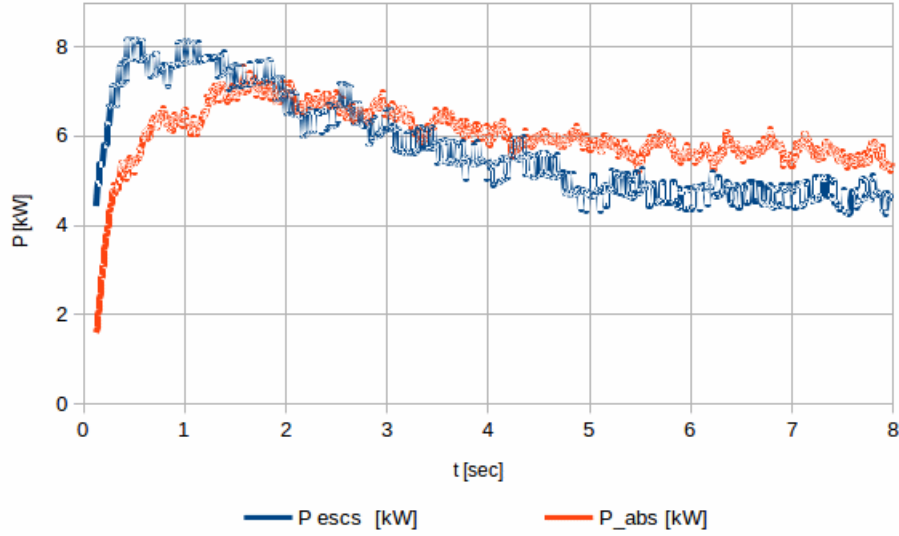


Fig. 5.13.: *Scenario 1: Heat power of all drops escaping from the absorber chamber P_{esc} and power produced by absorption P_{abs} .*

The heat flux Φ through the walls of the absorber chamber was determined using the tool “wallHeatFlux” which is part of the OpenFOAM standard distribution package. For scenario 1, Φ is plotted in Fig. 5.14. Although Fig. 5.12 indicates that the processes in the absorber seem to have settled after 5 seconds, Φ is still rising after 8 seconds. Following the development of the curve, one can estimate the maximum value at roughly about $\Phi = 120 W$. However, to meet eqn. 5.6, the heat flux had to be more than 500 W.

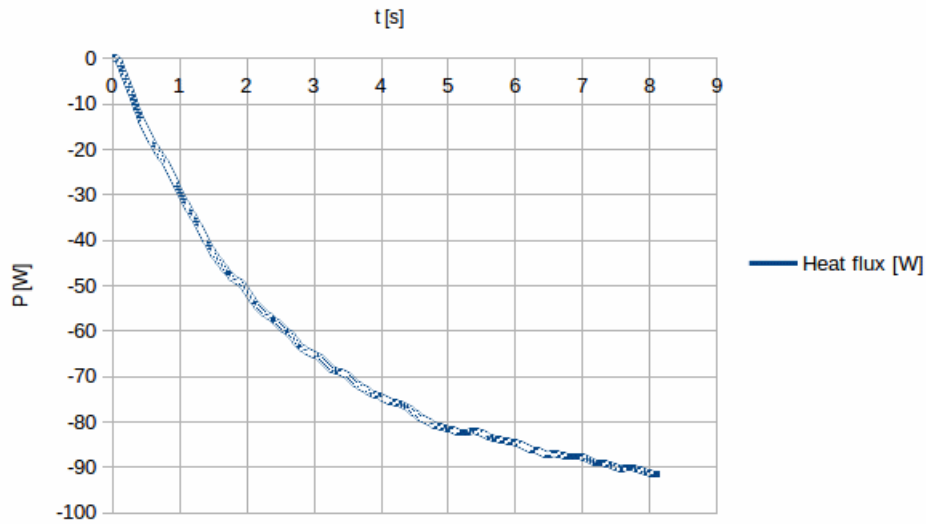


Fig. 5.14.: *Scenario 1: Heat flux through absorber chamber walls*

Applying eqn. 5.6 for all five scenarios, using the final mass fraction x , the temperature of the strong solution leaving the absorber T (as listed in Tab. 5.3) and the given injection flow rate of $\dot{V} = 4.067 \cdot 10^{-5} \frac{m^3}{s}$, the heat flux Φ resulting from this equation is listed in Tab. 5.4. The last column contains the COP calculated by in equations in sec. 1.3, assuming values for the other heat pump stages from [32]: $W_p = 23 W$, $T_{GE} = 368 K$, $T_{CO} = 322 K$. For some cases Φ turns even positive. This would mean that heat energy is flowing through the chamber walls into the chamber, which makes no sense, since the boundary condition for the wall temperature is set fix to $300 K$.

Scenario	x [kg/kg]	T [K]	Φ [W]	COP
1	0.09	340	-72	1, 17
2	0.09	347	1176	1, 23
3	0.04	320	435	0, 24
4	0.08	335	-129	0, 89
5	0.12	355	46	3, 29

Tab. 5.4.: *Heat flux and COP calculated from x and T using eqn. 5.6.*

5.3. Conclusions

Based on the data analysis in the previous section, the following conclusions can be drawn:

1. A quasi-constant circulation in the chamber is being induced by the momentum transfer between spray and fluid which influences the trajectories of the drops.
2. Due to this circulation, smaller drops remain longer in the chamber, as larger ones. So the ammonia concentration in small drops is higher than in large drops. However, most of the liquid volume is contributed by large drops, so the final ammonia mass fraction in the strong solution is dominated mostly by the large drops.
3. Higher absorption rates can be achieved by more surface area of the absorber (as this enhances the heat transfer from the fluid to the chamber wall) and by more volume of the absorber (as this raises the lifetime of the larger drops)
4. For the simple chamber and nozzle design as used in the above scenarios, a cost-efficient COP, according to chapter 1 can only be achieved by large chamber dimensions as in scenario 5.

5.4. Open Issues

Future works basing on this thesis may have to solve the following issues:

1. Due to the parcel-based injection procedure of the swirl nozzle model, the resulting flow rate of the injected fluid does not meet the target flow rate. Although this can be worked around by rising the target value in the configuration parameter, for future applications, the algorithm of parcel injection should be corrected accordingly.
2. The injection model “SwirlNozzleInjection” cannot be used in simulations running on multiple processors. It seems that the assignment of the cell IDs to the parcels is being mixed up in the current implementation when running on multiple processors. This bug has to be fixed before “SwirlNozzleInjection” can be used efficiently on large-scale simulations.
3. The conducted simulation in OpenFOAM show some implausible results regarding the amount of energy produced by absorption and the solubility of ammonia in water. Therefore the material parameters of the used absorption library have to be cross-checked.

5.5. Outlook

The identified weak points in the spray absorber setup can help to develop new approaches to improve the absorber efficiency. Some of them might be:

1. Place the nozzle on the bottom of the chamber and inject the liquid vertically up against the direction of gravitation. This would increase the life time even of the larger drops.
2. Increase the heat transfer between the gas and the chamber walls. E.g. by cooling fins on the inner surface of the absorber chamber or by a wire mesh inside the chamber. The lower chamber temperature resulting from this enhances the absorption rate. Furthermore, those structures might be able to “catch” the small drops with higher ammonia concentration out from the circulating gas flow.
3. Smaller drop diameters can be achieved by higher injection pressure (however, for the selected nozzles, this would imply a higher flow rate). E. g. for a AX-W-1/8-2-10 nozzle, an injection pressure of $P_{inj} = 2 \cdot 10^6 \text{ Pa}$ produces an average drop diameter of $D_{30} = 45 \mu\text{m}$. The resulting liquid flow rate in this case would be $\dot{V} = 1.667 \cdot 10^{-4} \frac{\text{m}^3}{\text{s}}$.
4. The life time of the drops may also be increased by an externally induced swirl flow of the gas that is strong enough to control the trajectory of even the larger drops (which mostly contribute to the total volume).

6. Summary

Preliminary estimations, both analytical and numerical, of the mass and heat transfer processes between water drops and ammonia vapor. The outcome of those was that small drop diameters and low initial velocity can raise the absorption rate. By comparing different nozzle types and their influence on spray properties, it was found that swirl nozzles meet both requirements -small drops at low velocity- the best. Several swirl nozzles with parameters within the specified flow rate and pressure range were chosen from a manufacturers catalog. For these (real) nozzles, the distribution function of drop diameter and velocity, and the individual parameters for the particular nozzles were determined using the Maximum Entropy Formalism (MEF) and empirical equations found in literature. In order to model the spray properties, especially the joint-drop-diameter-velocity distribution function in an OpenFOAM simulation environment, a C++ class reproducing the properties of a swirl nozzle was implemented as a part of a given solver.

Finally, the simulation environment for a spray absorber chamber, including the swirl nozzle model, was setup and five simulations were run with varying chamber dimensions and nozzle types. The results were analyzed with regard to absorption rate, ammonia concentration, drop- and chamber temperature and also plausibility. One of the results is that size and surface area of the absorber chamber has an high impact on the absorber performance. A cost-efficient COP can only be achieved by large absorber dimensions. Furthermore, it was found that the final ammonia concentration is dominated mainly by the large drops of the spray, whose absorption rate is much lower than for the small drops. The results for the heat energy produced by absorption were higher than expected and do not match with the resulting ammonia concentrations. Therefore, wrong material parameters used by the used absorption library were suspected, but could not be identified yet.

Appendix

A. Description of Class SwirlNozzleInjection

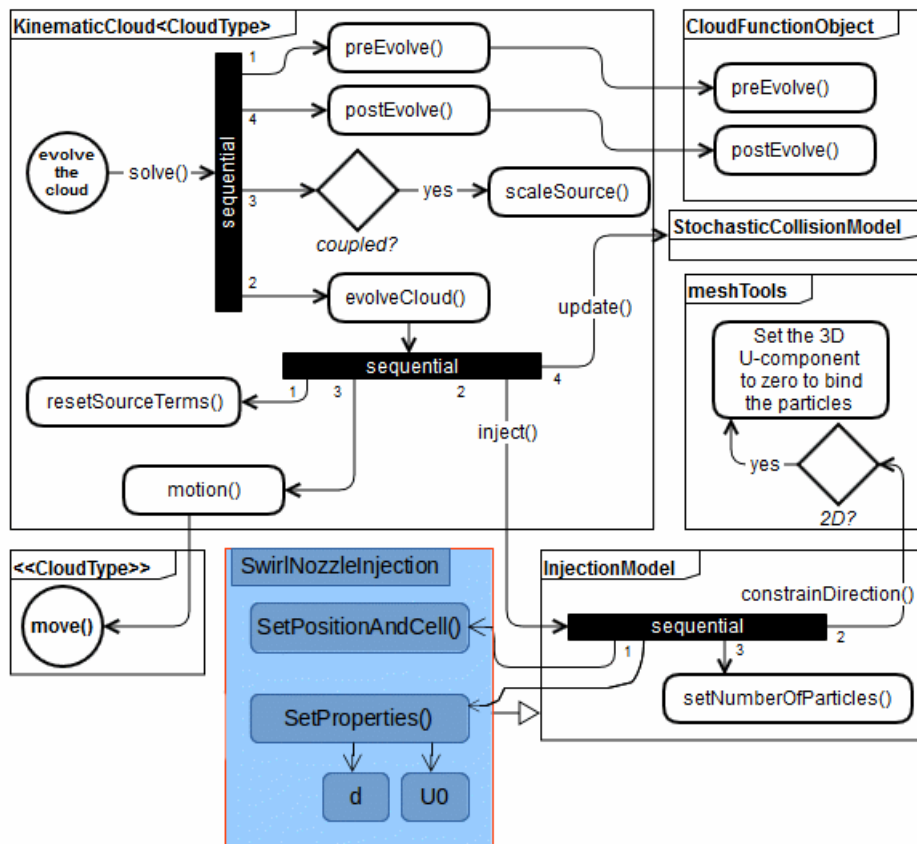


Fig. A.1.: The class *SwirlNozzleInjection* -highlighted in blue- inserted in the modified UML diagram of *KinematicCloud* [29].

A.1. Differences compared to ConeNozzleInjection

The class *SwirlNozzleInjection* is (just a modification of class *ConeNozzleInjection* from the OpenFOAM standard distribution package) derived from *InjectionModel*.

The UML diagram in Fig. A.1 shows the position of *SwirlNozzleInjection* within the class hierarchy. Some of the configuration parameters have changed and three of its member functions are overwritten: The constructor, *SetPositionAndCell()* and *SetProperties()*. The latter two are called from *InjectionModel*.

- Besides the initialization of the class attributes and reading the parameters from the configuration file, the vectors \vec{b} and \vec{c} perpendicular to the spray axis (see sec. 4.4.2.1), are calculated in the constructor.
- In *ConeNozzleInjection*, the member function *SetPositionAndCell()* is only used for identifying the initial position of the created parcel. However for the swirl nozzle model, the initial position of the drop can only be determined when the initial velocity is known (see sec. 4.4.2). The initial velocity, on the other hand, has to be determined by the joint diameter-velocity distribution function. This means that in *SetPositionAndCell()* all the parameters of the drop like diameter and initial velocity have to be calculated before the position can be identified.
- The member function *SetProperties()* no longer needs to calculate the parcel's diameter and velocity like in *ConeNozzleInjection*, because it has already been done in *SetPositionAndCell()*. The only thing that is left is copying these values to the call parameters *parcel.d* and *parcel.U*.

A.2. Description of Parameters

SwirlNozzleInjection needs a certain set of configuration parameters in the file *reactingCloud1Properties* as listed in Tab. A.1

Keyword	Type	Meaning	Valid Values
type	string	NozzleModel	"swirlNozzleInjection"
SOI	float	Start of injection [s]	$0 < \text{SOI} < \{\text{simulated time span}\}$
massTotal	float	Mass of all the fluid being injected [kg]	$\text{massTotal} = \text{flowRateProfile} * \text{duration} * \{\text{density of fluid}\}$
parcelBasisType	string		"fixed"
nParticle	float	Parcel multiplier	$1 \dots 1e37$
injectionMethod	string		"point"
UAvg	float	Average initial velocity of the drops [m/s]	$0 \dots 1e37$
D30	float	Mean volume diameter of drops [m]	$0 \dots 1e37$
duration	float	Duration of injection [s]	$\text{duration} = \{\text{simulated time span}\} - \text{SOI}$
position	vector	Position of nozzle orifice	Any point within the defined mesh
direction	vector	Direction of spray axis	Any vector
parcelsPerSecond	float	Number of parcels generated per second	$\text{parcelsPerSecond} = \frac{6 * \text{flowRateProfile}}{\pi * D30^3}$
flowRateProfile	float	Flow rate of injected liquid [m ³ /s]	$\text{flowRateProfile} = \{\text{"Real" flow rate}\} / nParticle$
orificeDiameter	float	Diameter of nozzle orifice [m]	$0 \dots 1e37$
Lb	float	Breakup length [m]	$0 \dots 1e37$
theta	float	Spray angle [°] (between spray axis and liquid sheet)	$0 \dots 90$
sheetThickness	float	Thickness of liquid sheet [m]	$0 \dots 1e37$
dMin	float	Minimum drop diameter (at the ratio of D30) being generated by the MonteCarlo algorithm	$0 \dots 1e37$
dMax	float	Maximum drop diameter (at the ratio of D30) being generated by the MonteCarlo algorithm	$0 \dots 1e37$
vMin	float	Minimum drop velocity (at the ratio of UAvg) being generated by the MonteCarlo algorithm	$0 \dots 1e37$
vMax	float	Maximum drop velocity (at the ratio of UAvg) being generated by the MonteCarlo algorithm	$0 \dots 1e37$
D_cr_f0	float	Parameter D_{cr} in eqn. 3.32	$0 \dots 1e37$
b_f0	float	Proportionality factor κ in eqn. 3.32	$0 \dots 1e37$
B	float	Parameter B in eqn. 3.22	$0 \dots 1e37$
lambda0	float	Parameter Λ_0 in eqn. 3.31	$-1e37 \dots 1e37$
lambda1	float	Parameter Λ_1 in eqn. 3.31	$-1e37 \dots 1e37$
lambda2	float	Parameter Λ_2 in eqn. 3.31	$-1e37 \dots 1e37$
lambda3	float	Parameter Λ_3 in eqn. 3.31	$-1e37 \dots 1e37$
fMax	float	Maximum value of $f(\bar{D}, \bar{U})$	$0 \dots 1$

Tab. A.1.: Configuration parameters required for SwirlNozzleInjection

The listing below shows an excerpt from the configuration file *reactingCloud1Properties* as it was used in one of the simulations:

```

1   injectionModels
2   {
3       modell //Spray.com 1_8_AX-2-10W, 68um, 67 deg, 55m/sec
4       {
5           type                swirlNozzleInjection;
6           SOI                 0.0;
7           massTotal           8.133e-7;//4.0667E-007;//4.0667E-002;
8           parcelBasisType    fixed;
9           nParticle           1e5;
10          injectionMethod    point;
11          UAvg                54.5;
12          D30                 67.5e-6;
13          duration            2.0;
14          position            (0.119 0 0);
15          direction           (-1 0 0);
16          parcelsPerSecond    2.53e3;
17          flowRateProfile     constant 4.0667E-010;//4.0667E-005;
18          orificeDiameter     0.001981;
19          Lb                  0.004836; // breakup length [m]
20          theta               67.0;
21          sheetThickness      0.0003796;
22          dMin                0.01; // at the ration of D30
23          dMax                4; // at the ration of D30
24          vMin                0.0; // at the ration of UAvg
25          vMax                4; // at the ration of UAvg
26          D_cr_f0             0.483;
27          b_f0                0.7892;
28          B                   0.0043505572;
29          lambda0             3.406;
30          lambda1             17.69;
31          lambda2             -35.54;
32          lambda3             18.06;
33          fMax                0.00379;
34      }
35  }

```

A.3. C++ source code

```

1  /*-----*\
2  ===== /
3  \\ / Field / OpenFOAM: The Open Source CFD Toolbox
4  \\ / Operation /
5  \\ / And / Copyright (C) 2011-2013 OpenFOAM Foundation
6  \\ / Manipulation /
7  -----*/
8  License
9  This file is part of OpenFOAM.
10
11  OpenFOAM is free software: you can redistribute it and/or modify it
12  under the terms of the GNU General Public License as published by
13  the Free Software Foundation, either version 3 of the License, or
14  (at your option) any later version.
15
16  OpenFOAM is distributed in the hope that it will be useful, but WITHOUT
17  ANY WARRANTY; without even the implied warranty of MERCHANTABILITY or
18  FITNESS FOR A PARTICULAR PURPOSE. See the GNU General Public License
19  for more details.
20
21  You should have received a copy of the GNU General Public License
22  along with OpenFOAM. If not, see <http://www.gnu.org/licenses/>.
23

```

```

24 \*-----*/
25
26 #include "SwirlNozzleInjection.H"
27 #include "TimeDataEntry.H"
28 #include "mathematicalConstants.H"
29 //#include "distributionModel.H"
30
31 using namespace Foam::constant;
32
33 // * * * * * Private Member Functions * * * * *
34
35 template<class CloudType>
36 void Foam::SwirlNozzleInjection<CloudType>::setInjectionMethod()
37 {
38     word injectionMethodType = this->coeffDict().lookup("injectionMethod");
39     if (injectionMethodType == "disc")
40     {
41         injectionMethod_ = imDisc;
42     }
43     else if (injectionMethodType == "point")
44     {
45         injectionMethod_ = imPoint;
46
47         // Set/cache the injector cell
48         this->findCellAtPosition
49         (
50             injectorCell_,
51             tetFaceI_,
52             tetPtI_,
53             position_,
54             false
55         );
56     }
57     else
58     {
59         FatalErrorIn("Foam::InjectionModel<CloudType>::setInjectionMethod()")
60             << "injectionMethod must be either 'point' or 'disc'"
61             << exit(FatalError);
62     }
63 }
64
65
66
67 template<class CloudType>
68 void Foam::SwirlNozzleInjection<CloudType>::setMEFParms()
69 {
70     this->coeffDict().lookup("UAvg") >> UAvg_;
71     this->coeffDict().lookup("D30") >> D30_;
72     this->coeffDict().lookup("sheetThickness") >> sheetThickness_;
73
74
75     this->coeffDict().lookup("dMin") >> dMin_;
76     this->coeffDict().lookup("dMax") >> dMax_;
77     this->coeffDict().lookup("vMin") >> vMin_;
78     this->coeffDict().lookup("vMax") >> vMax_;
79     this->coeffDict().lookup("B") >> B_;
80     this->coeffDict().lookup("Lb") >> Lb_;
81     this->coeffDict().lookup("lambda0") >> lambda0_;
82     this->coeffDict().lookup("lambda1") >> lambda1_;
83     this->coeffDict().lookup("lambda2") >> lambda2_;
84     this->coeffDict().lookup("lambda3") >> lambda3_;
85     this->coeffDict().lookup("fMax") >> fMax_;
86     this->coeffDict().lookup("b_f0") >> b_f0_;
87     this->coeffDict().lookup("D_cr_f0") >> D_cr_f0_;
88     fDistMax_ = fMax_;
89
90 }
91
92
93
94 //- MEF distribution function
95 template<class CloudType>

```

```

96 Foam::scalar Foam::SwirlNozzleInjection<CloudType>::fDist(scalar d, scalar v)
97 {
98     double retVal;
99     //Info << "MEF l0=" << lambda0_ << " l1=" << lambda1_ << " l2=" << lambda2_ << " l3=" << lambda3_ << " B="
    << B_ << nl;
100     if(d <= D_cr_f0_)
101     {
102         retVal = b_f0_*d*d*exp(-1-lambda0_-lambda1_*d*d-lambda2_*d*d*v-lambda3_*(d*d*v*v+B_*d*d));
103         //Info << "MEF D=" << d << " U=" << v << " f=" << retVal << nl;
104     }
105     else
106     {
107         scalar rho = 1.3654926004e-3;
108         scalar sigma = 7.28e-2; //surface tension of H2O
109         scalar We = rho*1000*UAvg_*UAvg_*sheetThickness_/sigma;//Weber number
110         scalar k = 2*pi*sqrt(3*sheetThickness_/(2*D30_))/(d*d);
111         scalar omega = sqrt((rho*tanh(k*sheetThickness_/2.)/((rho+tanh(k*sheetThickness_/2.))*(rho+tanh(k*
    sheetThickness_/2.))))-k*sheetThickness_/2.*We*(rho+tanh(k*sheetThickness_/2.)));
112         retVal = omega*exp(-1-lambda0_-lambda1_*d*d-lambda2_*d*d*v-lambda3_*(d*d*v*v+B_*d*d));
113         //Info << "MEF D=" << d << " U=" << v << " f=" << retVal << ", k = " << k << ", omega = " << omega << ",
    We = " << We << nl;
114     }
115
116     return (retVal);
117 }
118
119
120
121
122 // * * * * * Constructors * * * * * //
123
124 template<class CloudType>
125 Foam::SwirlNozzleInjection<CloudType>::SwirlNozzleInjection
126 (
127     const dictionary& dict,
128     CloudType& owner,
129     const word& modelName
130 )
131 :
132     InjectionModel<CloudType>(dict, owner, modelName, typeName),
133     injectionMethod_(imDisc),
134     orificeDiameter_(readScalar(this->coeffDict().lookup("orificeDiameter"))),
135     duration_(readScalar(this->coeffDict().lookup("duration"))),
136     position_(this->coeffDict().lookup("position")),
137     injectorCell_(-1),
138     tetFaceI_(-1),
139     tetPtI_(-1),
140     direction_(this->coeffDict().lookup("direction")),
141     parcelsPerSecond_
142     (
143         readScalar(this->coeffDict().lookup("parcelsPerSecond"))
144     ),
145
146     flowRateProfile_
147     (
148         TimeDataEntry<scalar>
149         (
150             owner.db().time(),
151             "flowRateProfile",
152             this->coeffDict()
153         )
154     ),
155     theta_
156     (
157         TimeDataEntry<scalar>
158         (
159             owner.db().time(),
160             "theta",
161             this->coeffDict()
162         )
163     ),
164     tanVec1_(vector::zero),

```

```

165     tanVec2_(vector::zero),
166     normal_b_(vector::zero),
167     normal_c_(vector::zero),
168     r_(vector::zero),
169     U_parcel_(vector::zero)
170 {
171
172     duration_ = owner.db().time().userTimeToTime(duration_);
173
174     //setInjectionMethod();
175
176     setMEFParms();
177
178     cachedRandom& rndGen = this->owner().rndGen();
179
180     // Normalise direction vector
181     direction_ /= mag(direction_);
182
183
184     //normal_b_(direction_.y()-direction_.z(), direction_.z()-direction_.x(), direction_.x()-direction_.y());
185     normal_b_.x() = direction_.y()-direction_.z();
186     normal_b_.y() = direction_.z()-direction_.x();
187     normal_b_.z() = direction_.x()-direction_.y();
188     normal_b_ /= mag(normal_b_);
189     normal_c_ = (direction_ ^ normal_b_);
190
191     // Set total volume to inject
192     this->volumeTotal_ = flowRateProfile_.integrate(0.0, duration_);
193
194     //updateMesh();
195 }
196
197
198 template<class CloudType>
199 Foam::SwirlNozzleInjection<CloudType>::SwirlNozzleInjection
200 (
201     const SwirlNozzleInjection<CloudType>& im
202 )
203 :
204     InjectionModel<CloudType>(im),
205     injectionMethod_(im.injectionMethod_),
206     orificeDiameter_(im.orificeDiameter_),
207     duration_(im.duration_),
208     position_(im.position_),
209     injectorCell_(im.injectorCell_),
210     tetFaceI_(im.tetFaceI_),
211     tetPtI_(im.tetPtI_),
212     direction_(im.direction_),
213     parcelsPerSecond_(im.parcelsPerSecond_),
214     flowRateProfile_(im.flowRateProfile_),
215     theta_(im.theta_),
216     tanVec1_(im.tanVec1_),
217     tanVec2_(im.tanVec1_),
218     normal_b_(im.normal_b_),
219     normal_c_(im.normal_c_),
220     UAvg_(im.UAvg_),
221     D30_(im.D30_),
222     dMin_(im.dMin_),
223     dMax_(im.dMax_),
224     vMin_(im.vMin_),
225     vMax_(im.vMax_),
226     B_(im.B_),
227     Lb_(im.Lb_),
228     lambda0_(im.lambda0_),
229     lambda1_(im.lambda1_),
230     lambda2_(im.lambda2_),
231     lambda3_(im.lambda3_),
232     fMax_(im.fMax_),
233     Pinj_(im.Pinj_)
234 {}
235
236

```

Appendix

```
237 // * * * * * Destructor * * * * * //
238
239 template<class CloudType>
240 Foam::SwirlNozzleInjection<CloudType>::~SwirlNozzleInjection()
241 {}
242
243
244 // * * * * * Member Functions * * * * * //
245
246 template<class CloudType>
247 void Foam::SwirlNozzleInjection<CloudType>::updateMesh()
248 {
249     // Set/cache the injector cells
250     switch (injectionMethod_)
251     {
252     case imPoint:
253     {
254         this->findCellAtPosition
255         (
256             injectorCell_,
257             tetFaceI_,
258             tetPtI_,
259             position_
260         );
261     }
262     default:
263     {
264         // do nothing
265     }
266     }
267 }
268
269
270 template<class CloudType>
271 Foam::scalar Foam::SwirlNozzleInjection<CloudType>::timeEnd() const
272 {
273     return this->SOI_ + duration_;
274 }
275
276
277 template<class CloudType>
278 Foam::label Foam::SwirlNozzleInjection<CloudType>::parcelsToInject
279 (
280     const scalar time0,
281     const scalar time1
282 )
283 {
284     if ((time0 >= 0.0) && (time0 < duration_))
285     {
286         Info<< "parcelsToInject :time1 = " << time1 << ", duration = " << duration_ << ", parcelsPerSecond = "
287             << parcelsPerSecond_ << "\n";
288         return floor((time1 - time0)*parcelsPerSecond_);
289     }
290     else
291     {
292         Info<< "parcelsToInject :nothing to inject as time0 = "
293             << time0 << "\n";
294         return 0;
295     }
296 }
297
298
299 template<class CloudType>
300 Foam::scalar Foam::SwirlNozzleInjection<CloudType>::volumeToInject
301 (
302     const scalar time0,
303     const scalar time1
304 )
305 {
306     if ((time0 >= 0.0) && (time0 < duration_))
307     {
```

```

308     return flowRateProfile_.integrate(time0, time1);
309 }
310 else
311 {
312     // Info << "volumeToInject : nothing to inject as time0 = "
313     // << time0 << nl;
314     return 0.0;
315 }
316 }
317
318
319 template<class CloudType>
320 void Foam::SwirlNozzleInjection<CloudType>::setPositionAndCell
321 (
322     const label,
323     const label,
324     const scalar time,
325     vector& position,
326     label& cellOwner,
327     label& tetFaceI,
328     label& tetPtI
329 )
330 {
331     cachedRandom& rndGen = this->owner().rndGen();
332     scalar y1;
333     scalar y2;
334     vector tangent;
335     vector swirlVelocity;
336     vector straightVelocity;
337     scalar t = time - this->SOI_;
338     scalar theta = theta_.value(t)*mathematical::pi/180;
339
340     scalar alpha = mathematical::twoPi*rndGen.sample01<scalar>();
341     r_ = 0.5*orificeDiameter_*(normal_b_*cos(alpha)+normal_c_*sin(alpha));
342     //Info << "normal_b_X = " << normal_b_.x() << " normal_b_Y = " << normal_b_.y() << " normal_b_Z = " <<
343     //normal_b_.z() << nl;
344     //Info << "normal_c_X = " << normal_c_.x() << " normal_c_Y = " << normal_c_.y() << " normal_c_Z = " <<
345     //normal_c_.z() << nl;
346
347
348
349     //r_ /= mag(r_);
350     while(1)
351     {
352         y1 = dMin_+(dMax_-dMin_)*rndGen.sample01<scalar>();
353         y2 = vMin_+(vMax_-vMin_)*rndGen.sample01<scalar>();
354
355         scalar U = rndGen.sample01<scalar>();
356         if (U<(fDist(y1,y2)/fDistMax_))
357             break;
358     }
359     Info << "D_rand = " << y1 << " U_rand = " << y2 << nl;
360     swirlVelocity = y2*UAvg_*sin(theta)*(-normal_b_*sin(alpha)+normal_c_*cos(alpha));
361     straightVelocity = direction_* y2*UAvg_*cos(theta);
362     U_parcel_ = straightVelocity + swirlVelocity;
363     // Info << "alpha = " << alpha << ", theta = " << theta << nl;
364     // Info << "U_X = " << U_parcel_.x() << " U_Y = " << U_parcel_.y() << " U_Z = " << U_parcel_.z() << nl;
365     D_parcel_ = y1*D30_;
366
367     halfAngle_ = theta_.value(t)*mathematical::pi/180.0;
368
369     switch (injectionMethod_)
370     {
371     case imPoint:
372     case imDisc:
373     {
374         vector UMag = U_parcel_/mag(U_parcel_);
375         //Info << "U_parcel_/mag(U_parcel_) = " << UMag.x() << ", " << UMag.y() << ", " << UMag.z() << ", "
376         //<< nl;
377         position = position_ + r_;

```



```

377 //Info << "x+r = positionX = " << position.x() << " positionY = " << position.y() << " positionZ
      = " << position.z() << nl;
378 position += Lb_*UMag;
379 //Info << "positionX = " << position.x() << " positionY = " << position.y() << " positionZ = "
      << position.z() << nl;
380 //Info << "position_X = " << position_.x() << " position_Y = " << position_.y() << " position_Z =
      " << position_.z() << nl;
381 //Info << "U_parcel_/mag(U_parcel_) = " << UMag.x() << ", " << UMag.y() << ", " << UMag.z() << ", "
      << nl;
382 //Info << "before this->findCellAtPosition" << nl;
383 this->findCellAtPosition
384 (
385     cellOwner,
386     tetFaceI,
387     tetPtI,
388     position,
389     false
390 );
391 Info << "after this->findCellAtPosition" << nl;
392 break;
393 }
394 default:
395 {
396     FatalErrorIn
397     (
398         "void Foam::SwirlNozzleInjection<CloudType>::setPositionAndCell"
399         "("
400             "const label, "
401             "const label, "
402             "const scalar, "
403             "vector&, "
404             "label&, "
405             "label&, "
406             "label&"
407         ")"
408     ) << "Unknown injectionMethod type" << nl
409     << exit(FatalError);
410 }
411 }
412 }
413
414
415 template<class CloudType>
416 void Foam::SwirlNozzleInjection<CloudType>::setProperties
417 (
418     const label parcelI,
419     const label,
420     const scalar time,
421     typename CloudType::parcelType& parcel
422 )
423 {
424
425     parcel.d() = D_parcel_;
426     parcel.U() = U_parcel_;
427     Info << "U_X = " << parcel.U().x() << " U_Y = " << parcel.U().y() << " U_Z = " << parcel.U().z() << nl;
428 }
429
430
431 template<class CloudType>
432 bool Foam::SwirlNozzleInjection<CloudType>::fullyDescribed() const
433 {
434     return false;
435 }
436
437
438 template<class CloudType>
439 bool Foam::SwirlNozzleInjection<CloudType>::validInjection(const label)
440 {
441     // Info << "injection valid " << nl;
442     return true;
443 }
444

```

A.4. Parameters for the Selected Nozzles

	AX-1/8-2	AX-1/8-3	AX-1/8-5	AX-1/8-8	AX-1/8-10	AX-W-1/8-2-3
massTotal	4.0667E-05	4.0667E-05	4.0667E-05	4.0667E-05	4.0667E-05	4.0667E-05
parcelBasisType	fixed	fixed	fixed	fixed	fixed	fixed
nParticle	1e4	1e4	1e4	1e4	1e4	1e4
injectionMethod	point	point	point	point	point	point
UAvg	35.6	22.81	12	6.9	5.4	41
D30	56.1e-6	84.5e-6	144.6e-6	241.1e-6	302.5e-6	58.4e-6
duration	10	10	10	10	10	10
position	(0.2 0 0)	(0.2 0 0)	(0.2 0 0)	(0.2 0 0)	(0.2 0 0)	(0.2 0 0)
direction	(-1 0 0)	(-1 0 0)	(-1 0 0)	(-1 0 0)	(-1 0 0)	(-1 0 0)
parcelsPerSecond	44090	12730	2568	554	281	38950
flowRateProfile	4.0667E-09	4.0667E-09	4.0667E-09	4.0667E-09	4.0667E-09	4.0667E-09
orificeDiameter	1.98e-3	2.39e-3	3.18e-3	3.96e-3	4.37e-3	1.98e-3
Lb	8.4e-3	0.01329	2.559e-2	4.8e-2	62.6e-3	6.71e-3
theta	36.2	34.8	31.7	26.4	24.6	50.3
sheetThickness	2.32e-4	3.37e-4	4.67e-4	6.28e-4	7.18e-4	2.93e-4
dMin	0.01	0.01	0.01	0.01	0.01	0.01
dMax	4	4	4	4	4	4
vMin	0	0	0	0	0	0
vMax	4	4	4	4	4	4
D_cr_f0	0.7159	1.134	3.475	20	20	0.6257
b_f0	0.486	0.1901	0.007357	3	3	0.5974
B	0.01233	0.0198	0.04167	0.076	0.0979	0.0089
lambda0	3.736	2.882	-0.3013	5.754	5.76	3.726
lambda1	3.464	3.022	2.036	1.554	1.403	5.504
labmda2	-6.848	-5.625	-3.467	-2.517	-2.235	-11.03
lambda3	3.72	3.12	2.065	1.622	1.499	5.804
fMax	2.3e-3	2.3e-3	1.88e-3	1.74e-3	1.7e-3	2.58e-3

Tab. A.2.: Configuration parameters for selected nozzles, part 1

	AX-W-1/8- 3-3	AX-W-1/8- 3-5	AX-W-1/8- 2-10	AX-W-1/8- 5-5	AX-W-1/8- 5-10	AX-W-1/8- 8-10
massTotal	4.0667E-05	4.0667E-05	4.0667E-05	4.0667E-05	4.0667E-05	4.0667E-05
parcelBasisType	fixed	fixed	fixed	fixed	fixed	fixed
nParticle	1e4	1e4	1e4	1e4	1e4	1e4
injectionMethod	point	point	point	point	point	point
UAvg	31.3	29.5	54.5	18.3	20.27	13.95
D30	68.3e-6	77.1e-6	67.5e-6	109e-6	121e-6	163e-6
duration	10	10	10	10	10	10
position	(0.2 0 0)	(0.2 0 0)	(0.2 0 0)	(0.2 0 0)	(0.2 0 0)	(0.2 0 0)
direction	(-1 0 0)	(-1 0 0)	(-1 0 0)	(-1 0 0)	(-1 0 0)	(-1 0 0)
parcelsPerSecond	24330	16970	25220	5998	4373	1793
flowRateProfile	4.0667E-09	4.0667E-09	4.0667E-09	4.0667E-09	4.0667E-09	4.0667E-09
orificeDiameter	2.39e-3	2.39e-3	1.98e-3	3.18e-3	3.18e-3	3.96e-3
Lb	8.64e-3	9.21e-3	4.84e-4	0.01465	0.013	0.01882
theta	53.3	53	67	56	63	65
sheetThickness	3.37e-4	3.59e-4	3.8e-4	4.67e-4	5.33e-4	6.65e-4
dMin	0.01	0.01	0.01	0.01	0.01	0.01
dMax	4	4	4	4	4	4
vMin	0	0	0	0	0	0
vMax	4	4	4	4	4	4
D_cr_f0	0.8237	0.8635	0.483	1.468	1.272	1.991
b_f0	0.3673	0.3359	0.7892	0.1102	0.1556	0.0556
B	0.013	0.013	0.00435	0.02392	0.01755	0.0556
lambda0	3.421	3.293	3.406	2.271	2.422	1.438
lambda1	4.209	4.742	17.69	3.317	5.775	4.65
labmda2	-8.252	-9.305	-3554	-6.132	-11.2	-8.9
lambda3	4.424	4.951	18.06	3.38	5.915	4.78
fMax	2.61e-3	2.78e-3	3.79e-3	2.27e-3	2.9e-3	2.57e-3

Tab. A.3.: Configuration parameters for selected nozzles, part 2

B. MEF Implementation in Sciab

```

1 clear;
2
3 // parameters from the data sheet
4
5 NozzleNameArray = ['1_8_AX-2' '1_8_AX-3' '1_8_AX-5' '1_8_AX-8' '1_8_AX-10' '1_8_AX-2-3W' '1_8_AX-3-3W' '1_
   8_AX-3-5W' '1_8_AX-2-10W' '1_8_AX-5-5W' '1_8_AX-5-10W' '1_8_AX-8-10W'];
6 d_0_in_Array = [0.078 0.094 0.125 0.156 0.172 0.078 0.094
   0.094 0.078 0.125 0.125 0.156];
7 spec_V_dot_gal_min_Ar = [0.63 0.6 0.61 0.57 0.71 0.61 0.60
   0.59 0.59 0.61 0.65 0.64];
8 spec_P_inj_psi_Array = [100 40 15 5 5 60 40
   30 20 15 10 5];
9 spec_ang_10psi_Array = [52 52 56 56 55 114 114
   116 130 116 126 124];
10 spec_ang_20psi_Array = [61 64 67 65 65 114 114
   110 135 110 121 112];
11 spec_ang_80psi_Array = [69 77 76 70 72 97 97
   95 120 92 95 90];
12
13
14 // constants
15 kb=1.38e-23; // boltzmann constant
16 rho_l = 1000; // density of H2O
17 rho_g = 1.3654926004; // density of NH3 at 200000 Pa
18 rho= rho_g/rho_l;
19 V_dot_l_m = 2.44; //target volume flow rate l/min
20 P_ch = 2e5; // chamber pressure in Pa
21 sigma = 7.28e-2; //surface tension of H2O
22 mu_g = 1.67160829859325E-005; // dynamic viscosity NH3 at 300K and 200kPa
23 mu_l = 0.000798; // dynamic viscosity H2O at 300K and 200kPa
24 V_dot = V_dot_l_m/(1000*60);
25 m_dot = rho_l*V_dot; //mass flow rate kg/sec
26
27 for allNozzles = 1:1:12
28 NozzleName = NozzleNameArray(allNozzles);
29 d_0_in = d_0_in_Array(allNozzles); // orifice in inch
30 spec_V_dot_gal_min = spec_V_dot_gal_min_Ar(allNozzles); // specified flow rate in gallons per minute
31 spec_P_inj_psi = spec_P_inj_psi_Array(allNozzles); // specified pressure in psi
32 spec_ang_10psi = spec_ang_10psi_Array(allNozzles); // specified spray angle at 10 psi
33 spec_ang_20psi = spec_ang_20psi_Array(allNozzles); // specified spray angle at 20 psi
34 spec_ang_80psi = spec_ang_80psi_Array(allNozzles); // specified spray angle at 80 psi
35
36
37
38
39 // convert parameters
40 r0 = 0.5*d_0_in*2.54e-2; // orifice radius of the nozzle in m
41 deltaP = spec_P_inj_psi*6894.76*(V_dot/(6.309E-005*spec_V_dot_gal_min))^2; //injection pressure difference
   in Pa
42
43 if deltaP < 20*6894.76 then
44     theta_deg = 0.5*(spec_ang_10psi + (spec_ang_20psi - spec_ang_10psi) * (deltaP - 10*6894.76) /
   (10*6894.76));
45 else
46     theta_deg = 0.5*(spec_ang_20psi + (spec_ang_80psi - spec_ang_20psi) * (deltaP - 20*6894.76) /
   (60*6894.76));
47 end

```

```

48
49
50 P_inj = deltaP + P_ch;
51 theta = theta_deg*pi/180;
52 U_0_Bernoulli = sqrt(2*deltaP/rho_l); // average liquid velocity
53
54 t_s = 2.7*(2*r0*V_dot*mu_l/deltaP)^0.25;
55 U_0 = V_dot/(%pi*cos(theta)*(r0^2-(r0-t_s)^2));
56 Lb = 3*(rho_l*sigma*t_s*2*r0/(rho_g^2*U_0^2*tan(theta)))^(1/3);
57
58 We = rho_g*U_0^2*t_s/sigma; //Weber number
59 Re = rho_g*U_0*t_s/mu_g; //Reynolds number
60
61 D32 = 4.52*((sigma*mu_l^2)/(rho_g*deltaP^2))^0.25*(t_s*cos(theta))^0.25 + 0.39*((sigma*rho_l)/(rho_g*deltaP
    ))^0.25*(t_s*cos(theta))^0.75;
62 D30 = 0.7764582*D32; // mean volume diameter
63 DropsPerSecond = V_dot/(D30^3*pi/6);
64
65
66 A = U_0*sin(theta)/r0; //swirl velocity
67 E = A*t_s/U_0; // swirling strength
68 C_d = 1.328/sqrt(Re); // drag coefficient;
69
70 a = (r0-t_s); //inner cone radius
71 Ah = a/t_s;
72
73
74
75 U_1 = sqrt(1+(E*(2*Ah+1)/2)^2);
76 B = 12*sigma/(rho_l*U_0^2*D30);
77 Q = rho_g/rho_l;
78 W = 0.0; //gas-to-liquid velocity ratio
79
80 S0 = 2*pi*(2*Ah+1)*Lb/t_s;
81 Smv = Q*C_d*(W-U_1)^2;
82 Se = 0.5*Q*C_d*S0*(W-U_1)^3;
83
84
85
86 d_min=0.1;
87 d_max=5;
88 v_min= 0;
89 v_max=4;
90 dv = 0.05;
91 dd = 0.05;
92 sd=1+(d_max-d_min)/dd;
93 sv=1+(v_max-v_min)/dv;
94
95
96
97 function n= k(d) // d is dimensionless !!!
98     n=2*pi*sqrt(3*t_s/(2*D30))/(d^2);
99 endfunction
100
101 function n = omega(d)
102     n= sqrt((rho*tanh(k(d)*t_s/2)/(rho+tanh(k(d)*t_s/2))^2)-k(d)*t_s/(2*We*(rho+tanh(k(d)*t_s/2))));
103 endfunction
104
105 function n=f0(i) // i(1) = Dc, i(2) = b
106     n1 = (i(2)*i(1)^2)-omega(i(1));
107     n2 = 2*i(2)*i(1) - numderivative(omega,i(1));
108     n = [n1;n2];
109
110 endfunction
111 mprintf('z 114\n');
112
113 d_c = 1/8;
114 while ((rho*tanh(k(d_c)*t_s/2)/(rho+tanh(k(d_c)*t_s/2))^2) < (k(d_c)*t_s/(2*We*(rho+tanh(k(d_c)*t_s/2)))))
115     d_c = d_c + 1/50;
116     if d_c > 20 then
117         break;
118     end

```

```

119     end
120     if d_c <= 20 then
121         k_dc = k(d_c);
122         mprintf('z 121\n');
123
124         i0 = [1.1*d_c 3e-3];
125         [n_res,u_res]=fsolve(i0,f0);
126         mprintf('z 125\n');
127         D_c = n_res(1);
128         b = n_res(2);
129     else
130         b = 3;
131         D_c = 20;
132     end
133
134     function p0=f_dist_prior(d_)// d is dimensionless!!
135         if d_ < D_c then
136             p0 = (b*d_^2);
137         else
138             p0 = omega(d_);
139         end
140     endfunction
141
142     d_0=[d_min:0.01:8*D_c];
143     d_0size = 1+(8*D_c-d_min)/0.01;
144     for i = 1:d_0size
145         fArray(i) = f_dist_prior(d_0(i))
146     end
147     fg = scf()
148     plot(d_0,fArray);
149     msprintf('/home/hp-notebook/ownCloud/Simulation_public/Kersch1_Mustafa/NozzlesAndDroplets/NozzleModels/%s_p_%1
150         .1f_d0_%1.1fmm_prior.jpg', NozzleName, P_inj, 2*r0*10);
151
152
153     function p=f_dist(d,v,l0,l1,l2,l3)
154         p=f_dist_prior(d)*exp(-1-l0-l1*d^3-l2*d^3*v-l3*(d^3*v^2+B*d^2));
155     endfunction
156
157     function y=f_MEF(l)
158         y1 = 0;
159         y2 = 0;
160         y3 = 0;
161         y4 = 0;
162         for i = d_min:dd:d_max
163             for j = v_min:dv:v_max
164                 y1 = y1 + f_dist(i,j,l(1),l(2),l(3),l(4));
165                 y2 = y2 + f_dist(i,j,l(1),l(2),l(3),l(4))*i^3;
166                 y3 = y3 + f_dist(i,j,l(1),l(2),l(3),l(4))*i^3*j;
167                 y4 = y4 + f_dist(i,j,l(1),l(2),l(3),l(4))*(i^3*j^2+B*i^2);
168             end
169         end
170         y1 = y1 - 1;
171         y2 = y2 - 1 - Smv;
172         y3 = y3 - 1 - Se;
173         y4 = y4 - 1;
174
175         y = [y1;y2;y3;y4];
176     endfunction
177
178
179
180     x0 = [0 0 0 0];
181
182     [x,u]=fsolve(x0,f_MEF);
183
184     deff('p=f(d,v)', 'p=f_dist(d,v,x(1),x(2),x(3),x(4))')
185
186     d=[d_min:dd:d_max];
187     v=[v_min:dv:v_max];
188
189     fField = zeros(sd,sv)

```

Appendix

```
190     maxFField = 0;
191     for i = 1:1:sd
192         for j = 1:1:sv
193             fField(i,j)=f(d(i),v(j))
194             if fField(i,j) > maxFField then
195                 maxFField = fField(i,j)
196                 D_Peak = i*dd+d_min;
197                 U_Peak = j*dv+v_min;
198             end
199         end
200     end
201
202     fpeak=maxFField;
203     kPeak = k(D_Peak);
204     omegaPeak = omega(D_Peak);
205     mprintf('d_peak = %.2f, U_Peak = %.2f, k = %.2f, f = %.4f, omega = %.4f\n', D_Peak, U_Peak, kPeak,
206             maxFField, omegaPeak);
207
208     // get variances around maxPos
209     dVar = stdev(D30*fField((D_Peak+d_min)/dd,:));
210     vVar = stdev(U_0*fField(:,(D_Peak+d_min)/dd));
211
212
213     fileName = sprintf('/home/hp-notebook/ownCloud/Simulation_public/Kersch1_Mustafa/NozzlesAndDroplets/
214                     NozzleModels/%s_p_%1.1f_d0_%1.1fmm.csv', NozzleName, P_inj, 2*r0*1000);
215
216     msprintf('/home/tkerschl/ownCloud/Simulation_public/Kersch1_Mustafa/NozzlesAndDroplets/NozzleModels/%s_p_%1.1
217             f_d0_%1.1fmm.csv', NozzleName, P_inj, 2*r0*1000);
218
219     fd = mopen(fileName, 'wt');
220     mfprintf(fd, 't_s [m], %3.3e\n', t_s);
221     mfprintf(fd, 'theta [deg], %3.3e\n', theta_deg);
222     mfprintf(fd, 'U_0 [m/s], %3.3e\n', U_0);
223     mfprintf(fd, 'Outer nozzle diameter [m], %3.3e\n', 2*r0);
224     mfprintf(fd, 'Inner cone diameter [m], %3.3e\n', 2*(r0-t_s));
225     mfprintf(fd, 'E, %3.3e\n', E);
226     mfprintf(fd, 'Lb [m], %3.3e\n', Lb);
227     mfprintf(fd, 'C_d, %3.3e\n', C_d);
228     mfprintf(fd, 'D32 [m], %3.3e\n', D32);
229     mfprintf(fd, 'D30 [m], %3.3e\n', D30);
230     mfprintf(fd, 'deltaP [Pa], %3.3e\n', deltaP);
231     mfprintf(fd, 'stdev(D) [m], %3.3e\n', dVar);
232     mfprintf(fd, 'stdev(U) [m/s], %3.3e\n', vVar);
233     mfprintf(fd, 'We, %3.3e\n', We);
234     mfprintf(fd, 'Re, %3.3e\n', Re);
235     mfprintf(fd, 'Dc, %3.3e\n', D_c);
236     mfprintf(fd, 'b, %3.3e\n', b);
237     mfprintf(fd, 'B, %3.3e\n', B);
238     mfprintf(fd, 'lambda0, %3.3e\n', x(1));
239     mfprintf(fd, 'lambda1, %3.3e\n', x(2));
240     mfprintf(fd, 'lambda2, %3.3e\n', x(3));
241     mfprintf(fd, 'lambda3, %3.3e\n', x(4));
242     mfprintf(fd, 'D_Peak, %3.3e\n', D_Peak);
243     mfprintf(fd, 'U_Peak, %3.3e\n', U_Peak);
244     mfprintf(fd, 'fpeak, %3.3e\n', fpeak);
245     mfprintf(fd, 'DropsPerSecond, %3.3e\n', DropsPerSecond);
246
247     for i = 1:1:sd
248         mfprintf(fd, '%3.3e, %3.3e\n', d(i)*D30, sum(fField(i,:)));
249     end
250
251     mclose(fd);
252
253     d=[d_min:dd:2];
254     v=[v_min:dv:2]';
255     sd=1+(2-d_min)/dd;
256     sv=1+(2-v_min)/dv;
257     fField = zeros(sd,sv)
258     for i = 1:1:sd
```

```

259     //di = di + dd;
260     for j= 1:1:sv
261         //vi = vi + dv
262         fField(i,j)=f(d(i),v(j))
263     end
264 end
265
266 fg = scf()
267 //plot3d1(d,v,fField/scaleFactor, -130, 60);
268 plot3d1(d,v,fField, -144, 89.852);
269 fg.color_map = summercolormap(32);
270
271 a=get("current_axes");
272
273
274 a.x_label
275 a.y_label
276 a.z_label
277
278
279 x_label=a.x_label;
280 x_label.text="D"
281 x_label.font_style= 5;
282 y_label=a.y_label;
283 y_label.text="U"
284 y_label.font_style= 5;
285 z_label=a.z_label;
286 z_label.text="f(D,U)"
287 z_label.font_style= 5;
288
289 fileName = sprintf('/home/hp-notebook/ownCloud/Simulation_public/Kersch1_Mustafa/NozzlesAndDroplets/
                NozzleModels/%s_p_%1.1f_d0_%1.1fmm_surf.jpg', NozzleName, P_inj, 2*r0*10);
290 xs2jpg(fg, fileName)
291 end

```


C. Results of Simulated Scenarios

C.1. Scenario 1

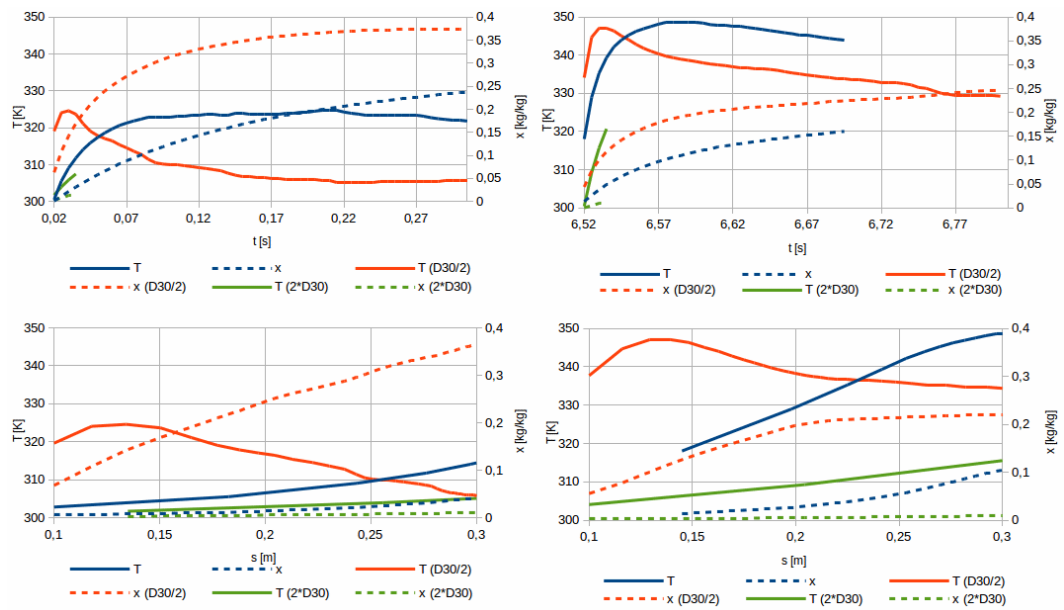


Fig. C.1.: Scenario 1: Ammonia concentration and drop temperature for three individual drops at the beginning of the simulation (left column) and at the end (right column), plotted against time (upper row) and distance (lower row).

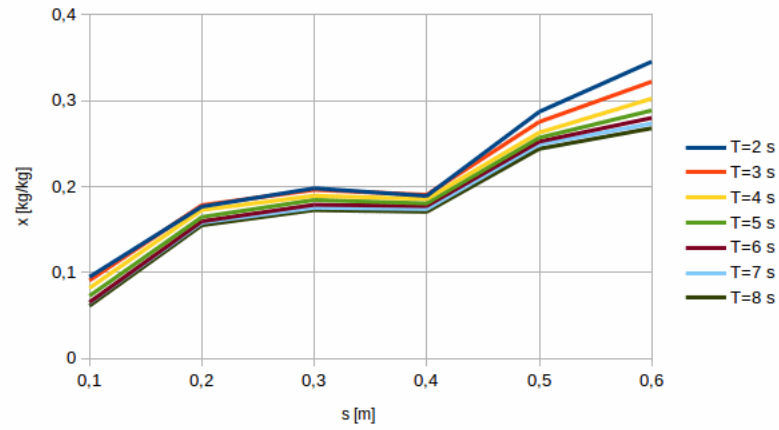


Fig. C.2.: *Scenario 1: Ammonia concentration of all drops as a function of their distance from the nozzle, evaluated at different times.*

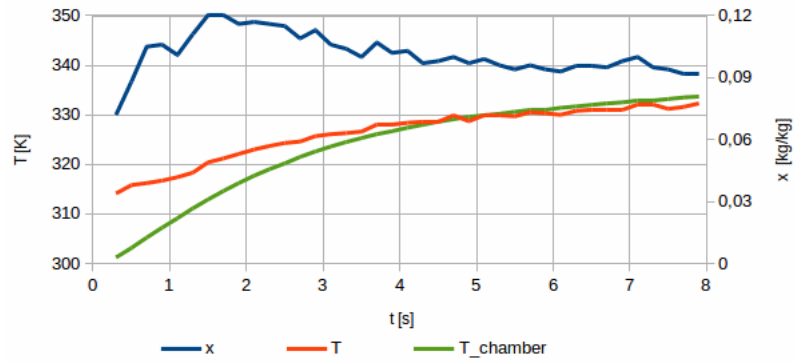


Fig. C.3.: *Scenario 1: Average ammonia concentration and average temperature of all impinging drops, average chamber temperature as a function of time.*

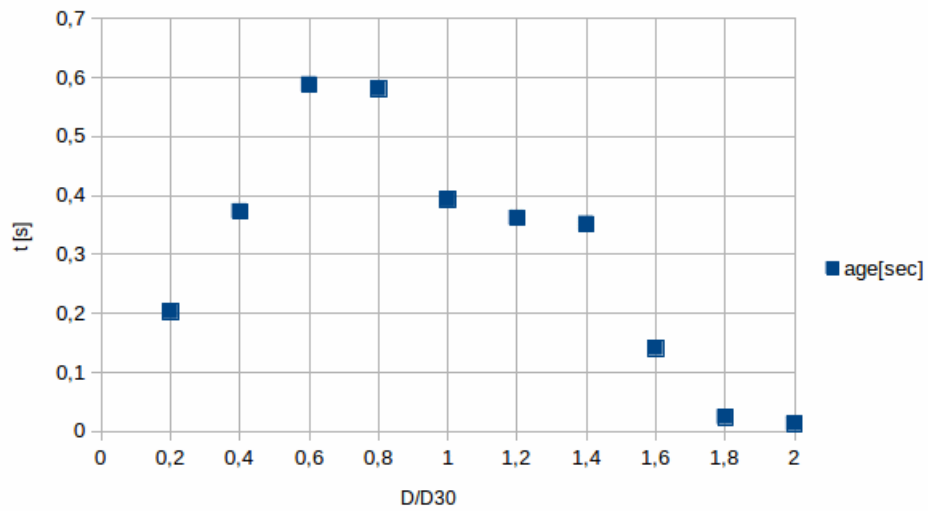


Fig. C.4.: Scenario 1: Average lifetime of drops as a function of their diameter.

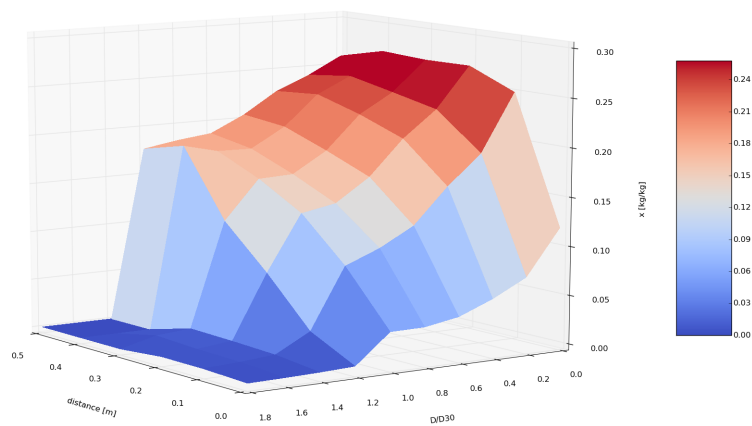


Fig. C.5.: Scenario 1: Ammonia mass fraction as a function of distance from the nozzle and of drop diameter $x(D, s)$.

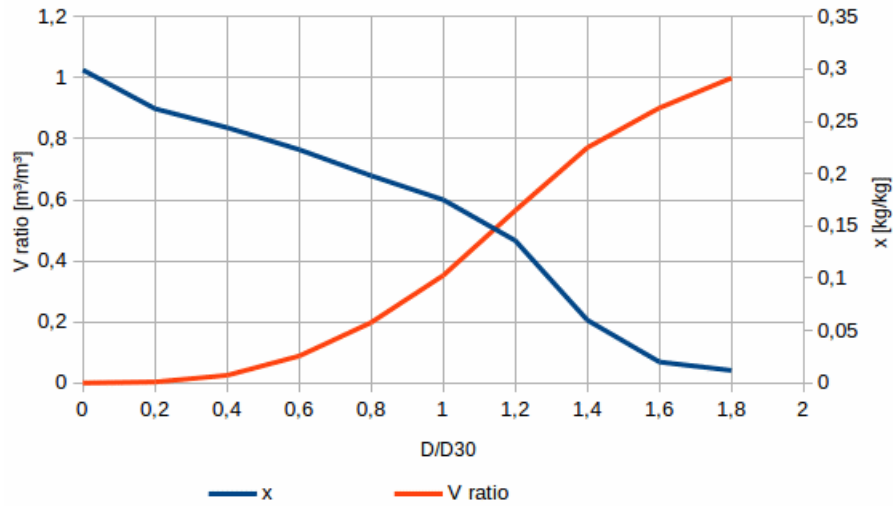


Fig. C.6.: Scenario 1: Red: Fraction of total volume formed by drops of diameter smaller than $\bar{D} = \frac{D}{D_{30}}$. Blue: Ammonia mass fraction of amount of liquid formed by drops of diameter smaller than \bar{D} .

C.2. Scenario 2

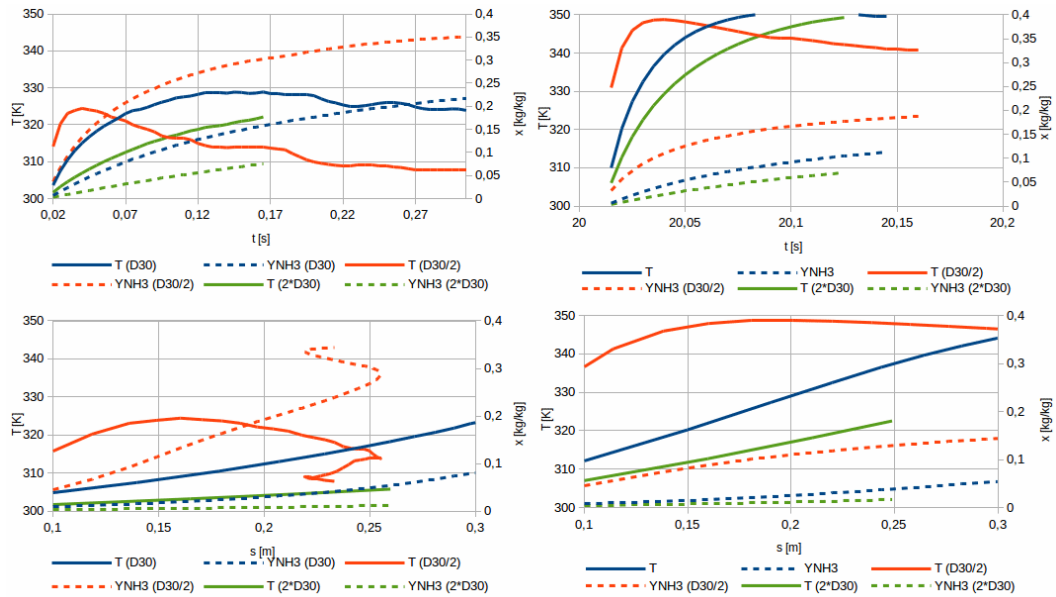


Fig. C.7.: Scenario 2: Ammonia concentration and drop temperature for three individual drops at the beginning of the simulation (left column) and at the end (right column), plotted against time (upper row) and distance (lower row).

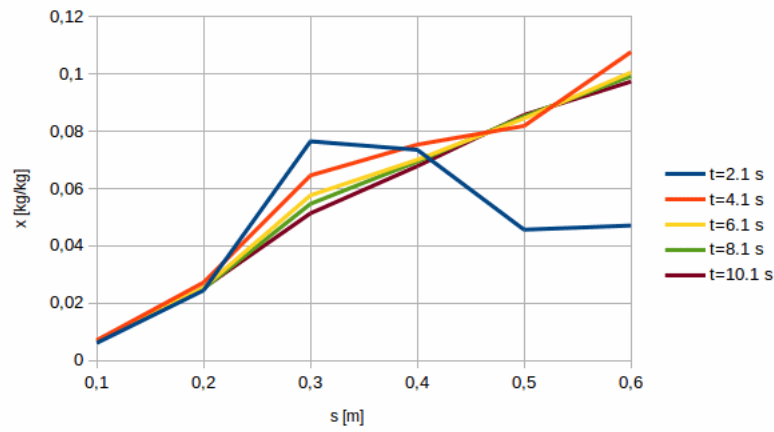


Fig. C.8.: *Scenario 2: Ammonia concentration of all drops as a function of their distance from the nozzle, evaluated at different times.*

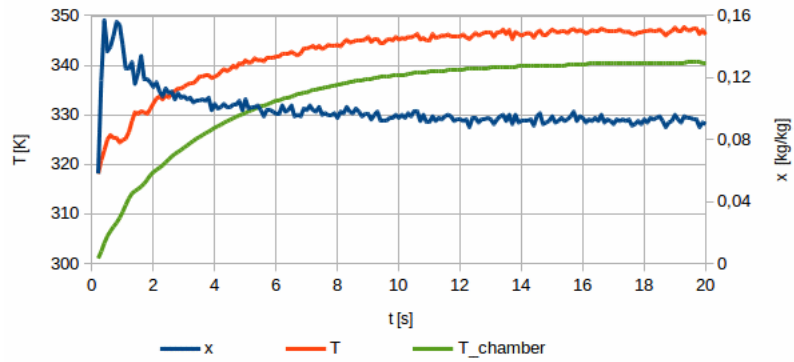


Fig. C.9.: *Scenario 2: Average ammonia concentration and average temperature of all impinging drops, average chamber temperature as a function of time.*

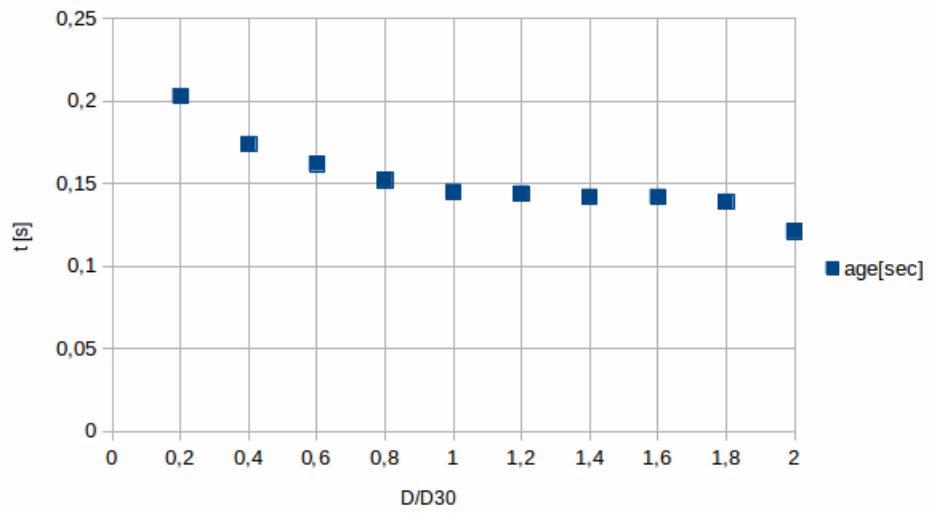


Fig. C.10.: *Scenario 2: Average lifetime of drops as a function of their diameter.*

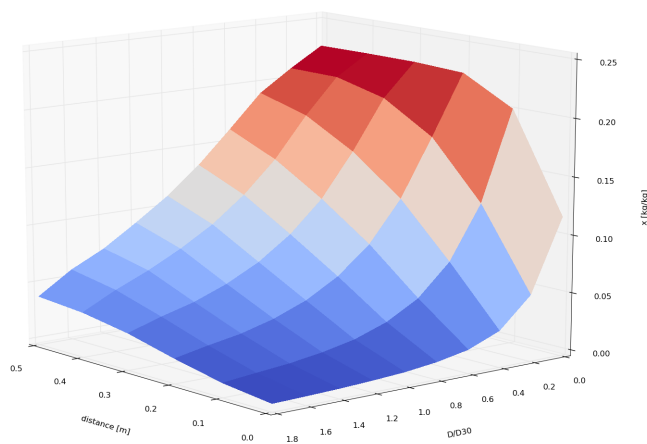


Fig. C.11.: *Scenario 2: Ammonia mass fraction as a function of distance from the nozzle and of drop diameter $x(D, s)$.*

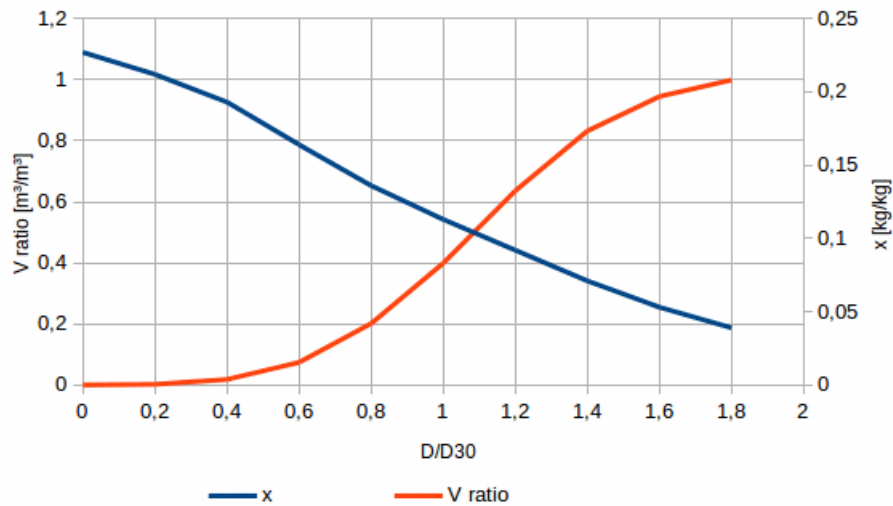


Fig. C.12.: Scenario 2: Red: Fraction of total volume formed by drops of diameter smaller than $\bar{D} = \frac{D}{D_{30}}$. Blue: Ammonia mass fraction of amount of liquid formed by drops of diameter smaller than \bar{D} .

C.3. Scenario 3

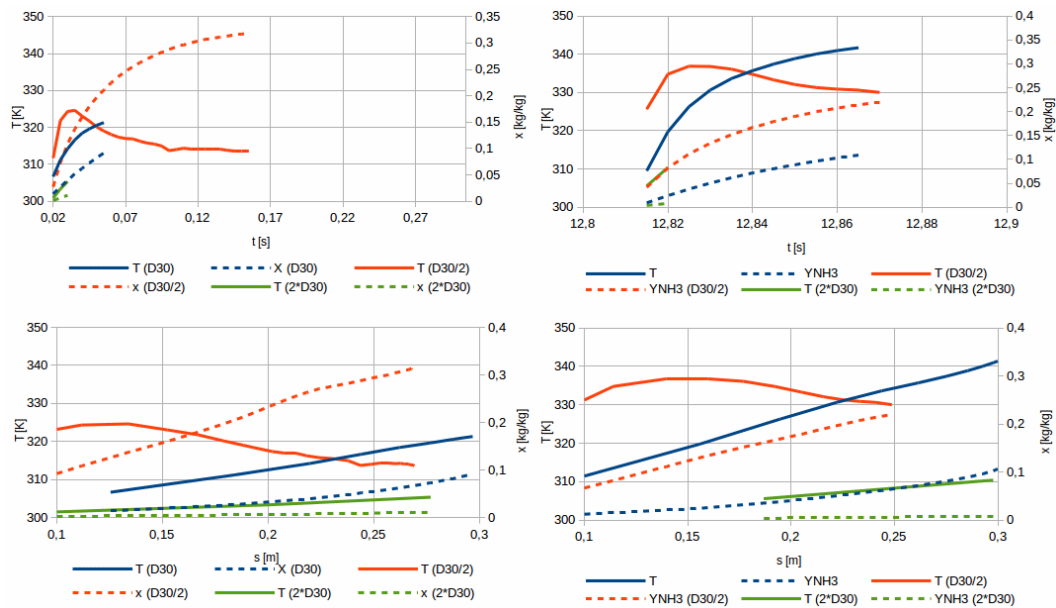


Fig. C.13.: Scenario 3: Ammonia concentration and drop temperature for three individual drops at the beginning of the simulation (left column) and at the end (right column), plotted against time (upper row) and distance (lower row).

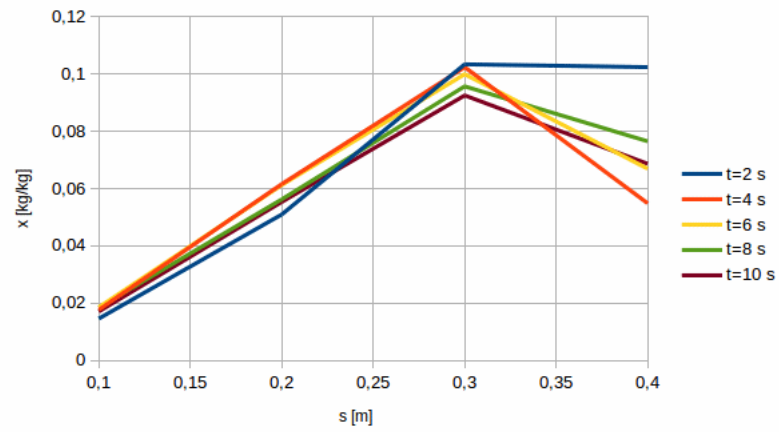


Fig. C.14.: *Scenario 3: Ammonia concentration of all drops as a function of their distance from the nozzle, evaluated at different times.*

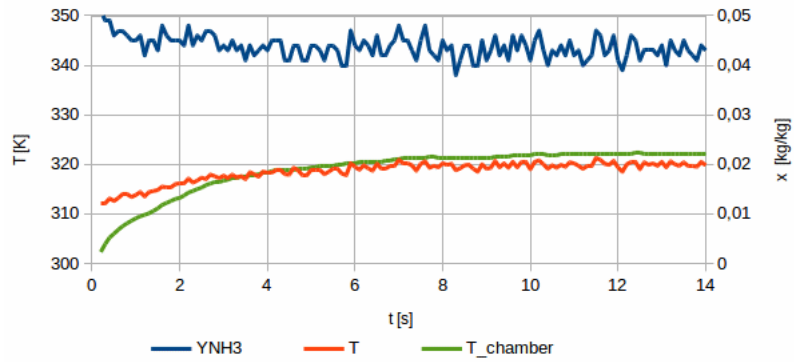


Fig. C.15.: *Scenario 3: Average ammonia concentration and average temperature of all impinging drops, average chamber temperature as a function of time.*

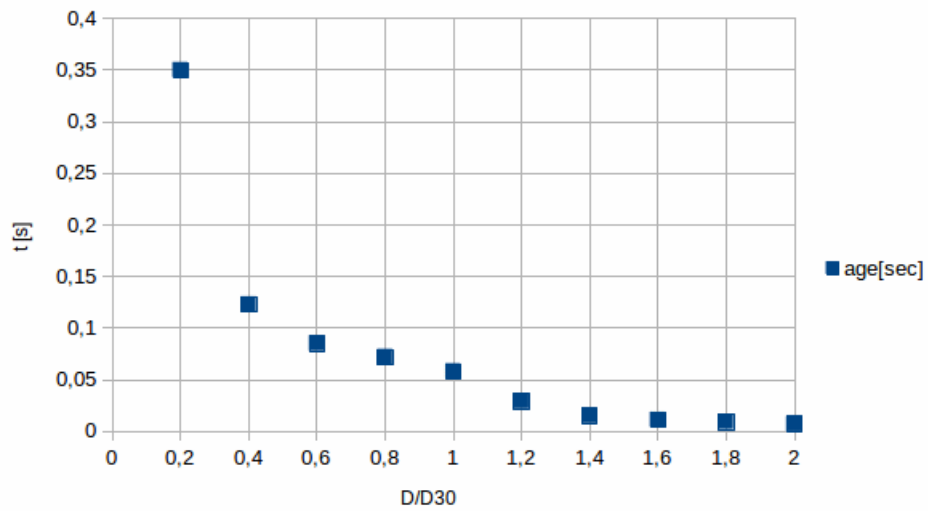


Fig. C.16.: Scenario 3: Average lifetime of drops as a function of their diameter.

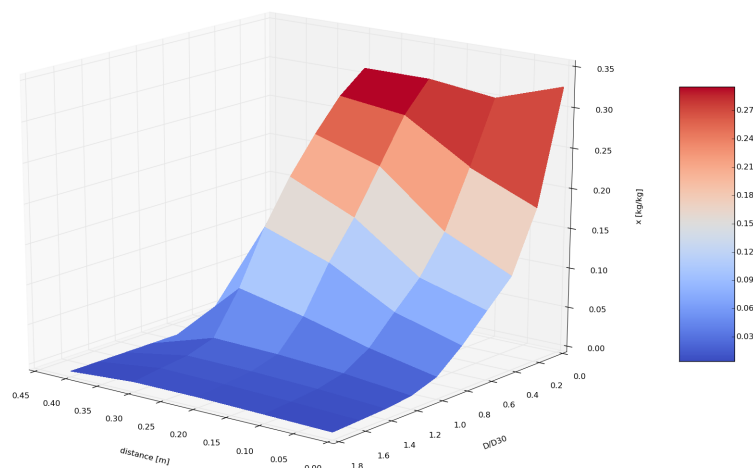


Fig. C.17.: Scenario 3: Ammonia mass fraction as a function of distance from the nozzle and of drop diameter $x(D, s)$.

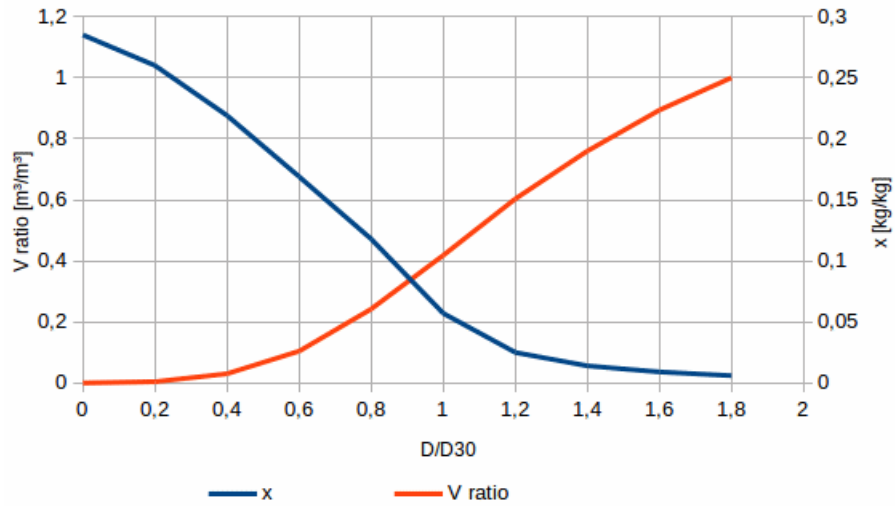


Fig. C.18.: Scenario 3: Red: Fraction of total volume formed by drops of diameter smaller than $\bar{D} = \frac{D}{D_{30}}$. Blue: Ammonia mass fraction of amount of liquid formed by drops of diameter smaller than \bar{D} .

C.4. Scenario 4

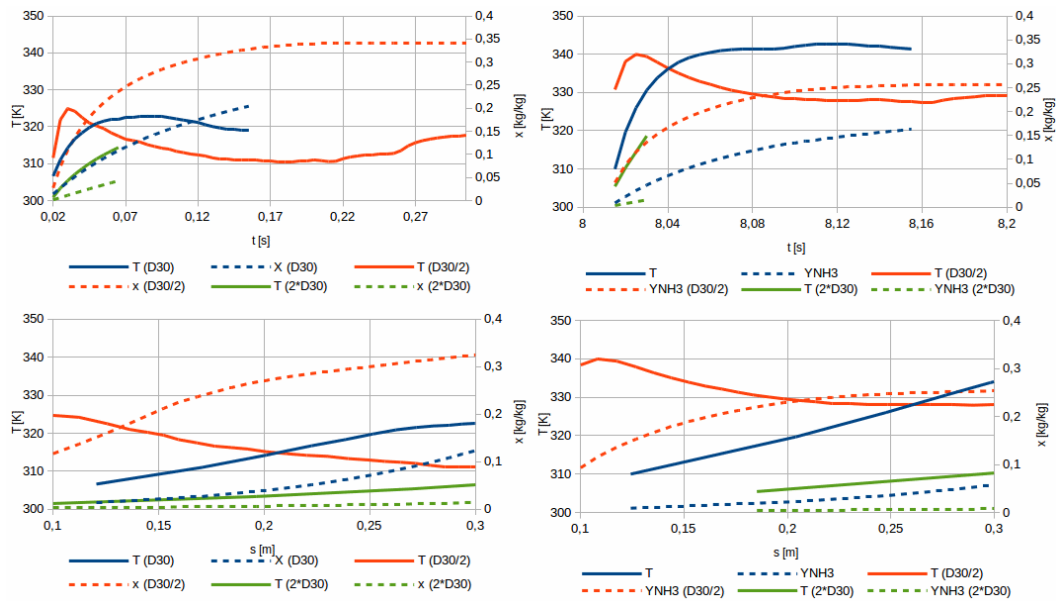


Fig. C.19.: Scenario 4: Ammonia concentration and drop temperature for three individual drops at the beginning of the simulation (left column) and at the end (right column), plotted against time (upper row) and distance (lower row).

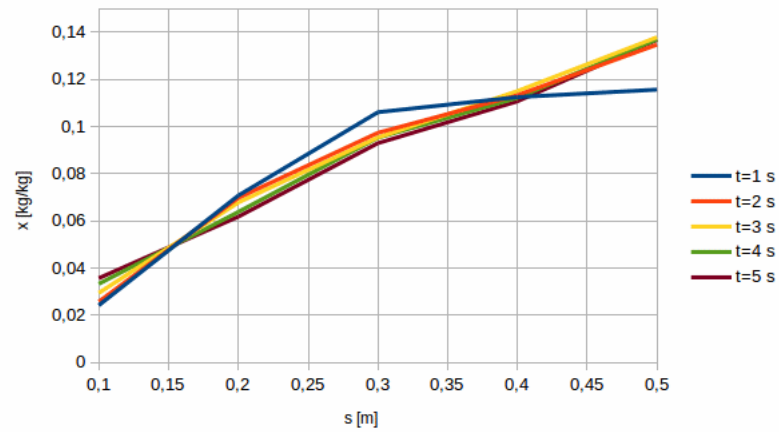


Fig. C.20.: Scenario 4: Ammonia concentration of all drops as a function of their distance from the nozzle, evaluated at different times.

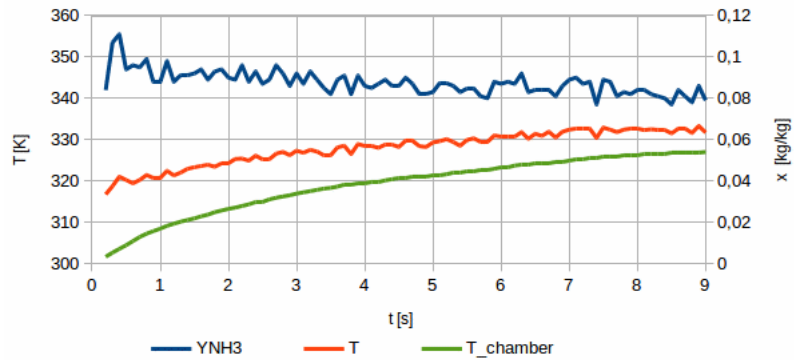


Fig. C.21.: Scenario 4: Average ammonia concentration and average temperature of all impinging drops, average chamber temperature as a function of time.

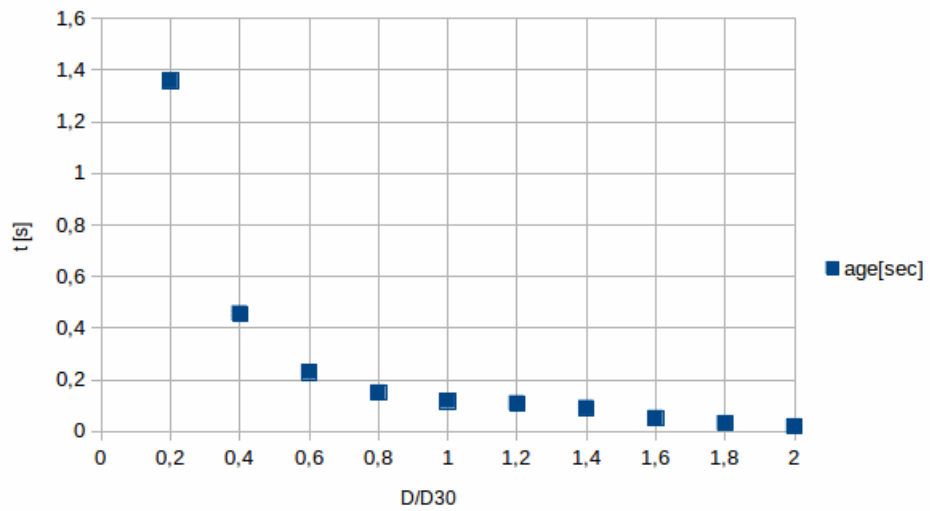


Fig. C.22.: *Scenario 4: Average lifetime of drops as a function of their diameter.*

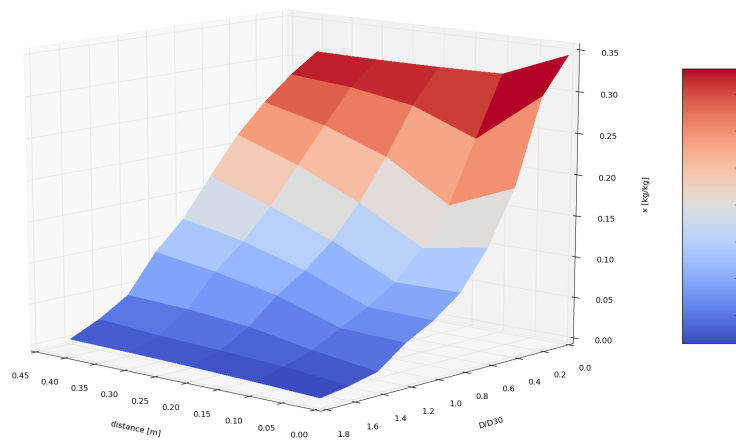


Fig. C.23.: *Scenario 4: Ammonia mass fraction as a function of distance from the nozzle and of drop diameter $x(D, s)$.*

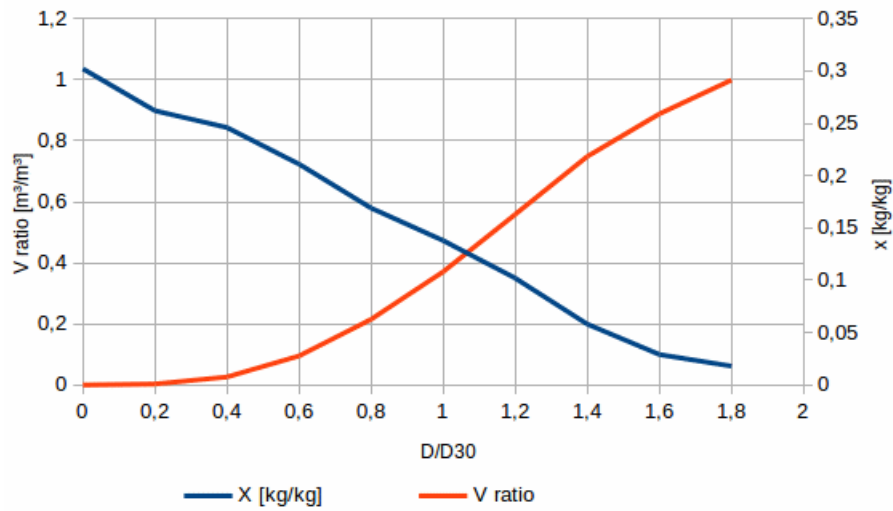


Fig. C.24.: Scenario 4: Red: Fraction of total volume formed by drops of diameter smaller than $\bar{D} = \frac{D}{D_{30}}$. Blue: Ammonia mass fraction of amount of liquid formed by drops of diameter smaller than \bar{D} .

C.5. Scenario 5

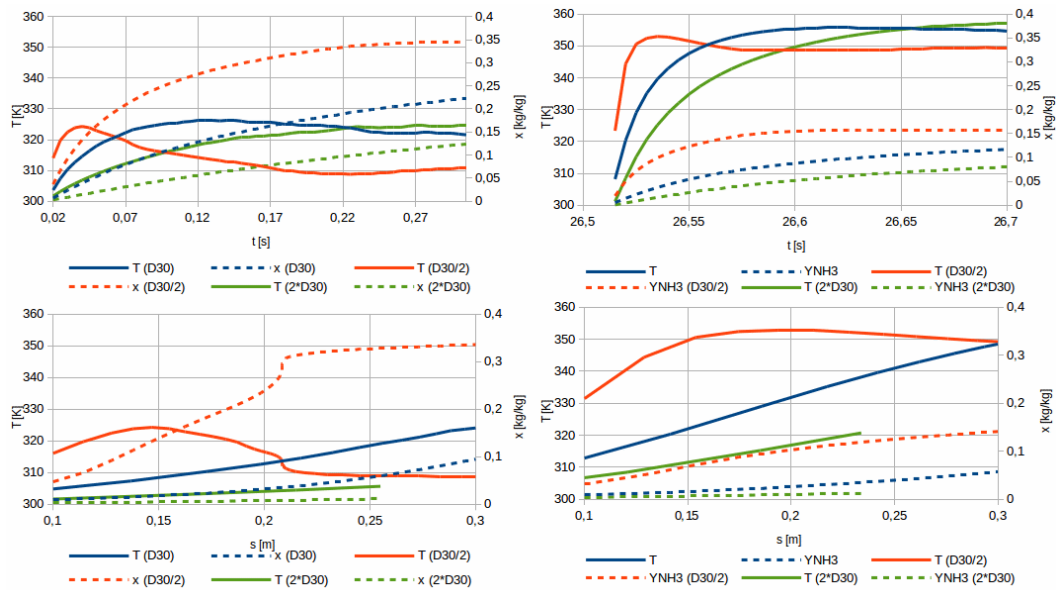


Fig. C.25.: Scenario 5: Ammonia concentration and drop temperature for three individual drops at the beginning of the simulation (left column) and at the end (right column), plotted against time (upper row) and distance (lower row).

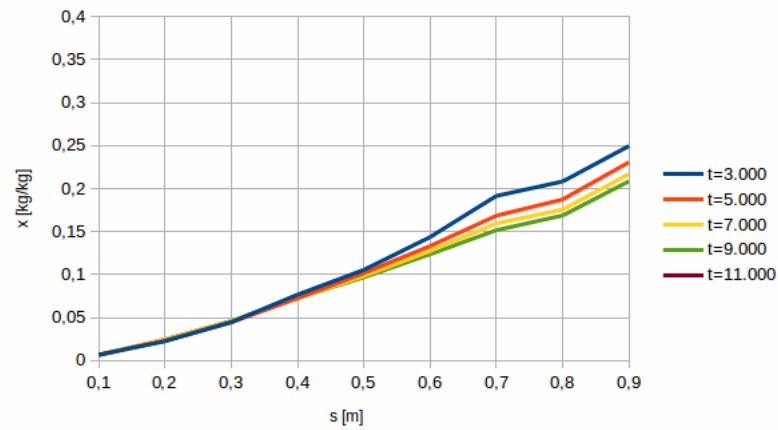


Fig. C.26.: *Scenario 5: Ammonia concentration of all drops as a function of their distance from the nozzle, evaluated at different times.*

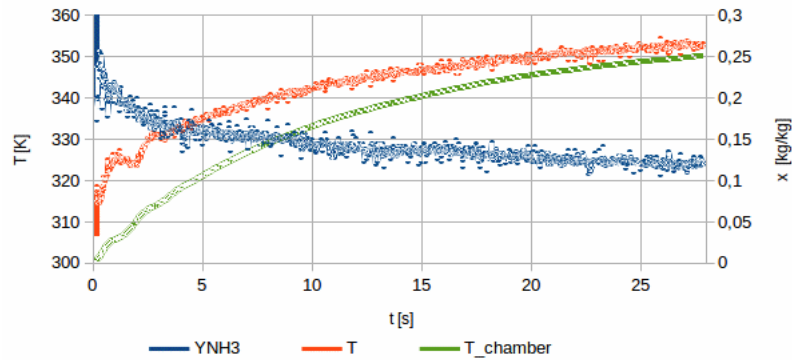


Fig. C.27.: *Scenario 5: Average ammonia concentration and average temperature of all impinging drops, average chamber temperature as a function of time.*

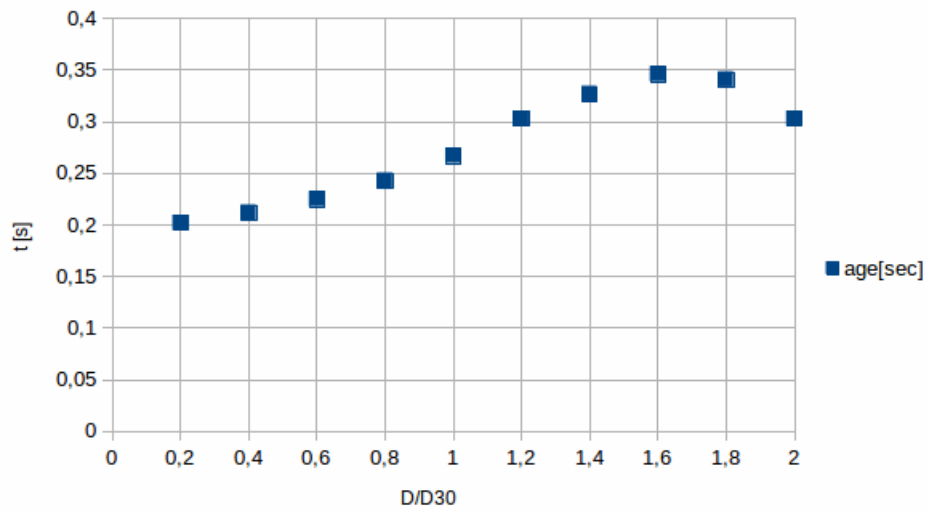


Fig. C.28.: Scenario 5: Average lifetime of drops as a function of their diameter.

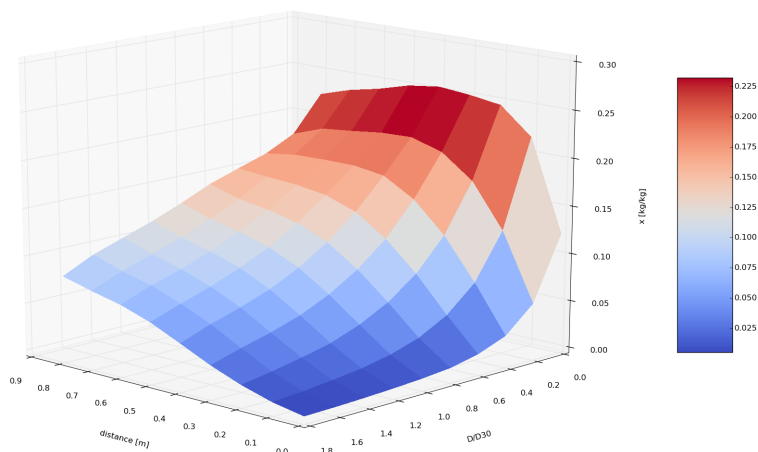


Fig. C.29.: Scenario 5: Ammonia mass fraction as a function of distance from the nozzle and of drop diameter $x(D, s)$.

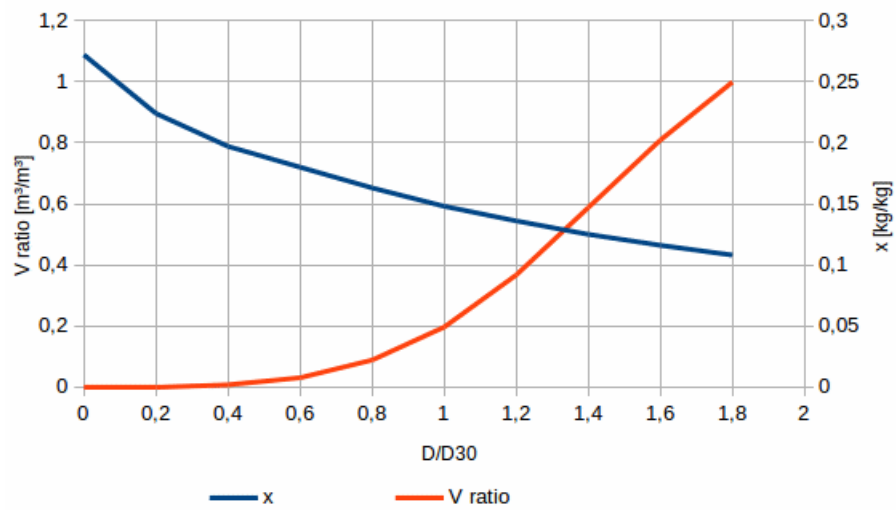


Fig. C.30.: Scenario 5: Red: Fraction of total volume formed by drops of diameter smaller than $\bar{D} = \frac{D}{D_{30}}$. Blue: Ammonia mass fraction of amount of liquid formed by drops of diameter smaller than \bar{D} .

Bibliography

- [1] Spraying Systems Co. <http://www.spray.com/cat75/hydraulic/offline/download.pdf>
Last change: 2013. Download: 16 March 2016.
- [2] Ghobad Amini. Liquid flow in a simplex swirl nozzle. *International Journal of Multiphase Flow*, 79:225–235, March 2016.
- [3] Sigma-Aldrich. Ammonium Hydroxide Product Information. https://www.sigmaaldrich.com/content/dam/sigmaaldrich/docs/Sigma/Product_information_sheet/a6899pis.pdf. Last change: 3 Feb 2003. Download: 15 April 2016.
- [4] Nasser Ashgriz, editor. *Handbook of atomization and sprays: theory and applications*. Springer, New York, NY, 2011.
- [5] E. Babinsky and P.E. Sojka. Modeling drop size distributions. *Progress in Energy and Combustion Science*, 28(4):303–329, January 2002.
- [6] Hans Dieter Baehr and Karl Stephan. *Waerme- und Stoffuebertragung*. Springer Berlin Heidelberg, Berlin, Heidelberg, 2013.
- [7] R. Byron Bird, Warren E. Stewart, and Edwin N. Lightfoot. *Transport phenomena*. J. Wiley, New York, 2nd, wiley international ed edition, 2002.
- [8] Wikipedia contributors. <https://en.wikipedia.org/wiki/OpenFOAM>. Last change: 9 August 2015. Download: 26 March 2016 07:41 UTC.
- [9] A. Datta and S.K. Som. Numerical prediction of air core diameter, coefficient of discharge and spray cone angle of a swirl spray pressure nozzle. *International Journal of Heat and Fluid Flow*, 21(4):412–419, August 2000.
- [10] Christophe Dumouchel. The Maximum Entropy Formalism and the Prediction of Liquid Spray Drop-Size Distribution. *Entropy*, 11(4):713–747, November 2009.

- [11] T. Elperin, A. Fominykh, and Z. Orenbakh. Coupled heat and mass transfer during nonisothermal absorption by falling droplet with internal circulation. *International Journal of Refrigeration*, 30(2):274–281, March 2007.
- [12] Donald Fenton, Amy Noeth, and Robert Groton. Absorption of Ammonia into Water. *ASHRAE Transactions Research*, 97(1), 1991.
- [13] Bundesministerium fuer Wirtschaft und Energie. Gesetz zur Foerderung Erneuerbarer Energien im Waermebereich <http://www.bmwi.de/DE/Service/gesetze,did=588536.html>. Last change: 21 July 2014. Download: 9 May 2016.
- [14] Christian Gerthsen, Dieter Meschede, and Helmut Vogel. *Gerthsen Physik*. Springer, Berlin, 2006.
- [15] G. Grosche, Ilja N. Bronstejn, and Konstantin A. Semendjaev, editors. *Taschenbuch der Mathematik. [Hauptbd.]*. Verl. Nauka, Moskau, 25. aufl edition, 1991.
- [16] William M. Haynes and David R. Lide, editors. *CRC handbook of chemistry and physics: a ready-reference book of chemical and physical data*. CRC Press, Boca Raton, Fla., 96. ed., 2015-2016 edition, 2015.
- [17] Jonathan Ibarra-Bahena and Rosenberg Romero. Performance of Different Experimental Absorber Designs in Absorption Heat Pump Cycle Technologies: A Review. *Energies*, 7(2):751–766, February 2014.
- [18] Gerd Junge. *Einfuehrung in die Technische Stroemungslehre*. Carl Hanser Verlag GmbH & Co. KG, Muenchen, 2 edition, June 2015.
- [19] J. M. Kay and R. M. Nedderman. *Fluid mechanics and transfer processes*. Cambridge University Press, Cambridge [Cambridgeshire] ; New York, N.Y, 1985.
- [20] Woo-Tae Kim, Sushanta K. Mitra, Xianguo Li, L. A. Prociw, and T. C. J. Hu. A Predictive Model for the Initial Droplet Size and Velocity Distributions in Sprays and Comparison with Experiments. *Particle & Particle Systems Characterization*, 20(2):135–149, May 2003.
- [21] Norbert Kuhn and Thomas M. Klapoetke. *Allgemeine und Anorganische Chemie*. Springer Berlin Heidelberg, Berlin, Heidelberg, 2014.
- [22] Arthur H. Lefebvre. *Atomization and sprays*. Combustion. Hemisphere Pub. Corp, New York, 1989.

- [23] Xianguo Li and Meishen Li. Droplet Size Distribution in Sprays Based on Maximization of Entropy Generation. *Entropy*, 5(5):417–431, December 2003.
- [24] Sushanta K. Mitra. *Breakup process of plane liquid sheets and prediction of initial droplet size and velocity distributions in sprays*. PhD Thesis, University of Waterloo, Ontario, Canada, 2001.
- [25] Badie I. Morsi and Omar M. Basha. Mass Transfer in Multiphase Systems. In Marek Solecki, editor, *Mass Transfer - Advancement in Process Modelling*. InTech, October 2015.
- [26] Ehsan Movahednejad, Fathollah Ommi, and S. Mostafa Hosseinalipour. Prediction of Droplet Size and Velocity Distribution in Droplet Formation Region of Liquid Spray. *Entropy*, 12(6):1484–1498, June 2010.
- [27] Thomas Mueller-Gronbach, Erich Novak, and Klaus Ritter. *Monte Carlo-Algorithmen*. Springer-Lehrbuch. Springer Berlin Heidelberg, Berlin, Heidelberg, 2012.
- [28] R. A. Mugele and H. D. Evans. Droplet Size Distribution in Sprays. *Industrial & Engineering Chemistry*, 43(6):1317–1324, June 1951.
- [29] OpenFOAMWiki. http://openfoamwiki.net/index.php/OpenFOAM_guide/UML/lagrangian Last change: 1 Dec 2014 . Download: 29 June 2016.
- [30] William Partlow. <http://www.civilengineeringhandbook.tk/coal-liquefaction/combustion-of-liquid-fuels.html> Last change: 28 March 2016. Download: 17 June 2016.
- [31] Robert H. Perry, Don W. Green, and James O. Maloney, editors. *Perry's chemical engineers' handbook*. McGraw-Hill, New York, 7th ed edition, 1997.
- [32] Sylvia Cristina Porras Seyler. *Thermodynamic Simulation of the Absorption Process for Residential Gas Heat Pumps*. Dipl. Thesis, Universitaet Stuttgart & Robert Bosch GmbH, Stuttgart, 2013.
- [33] W. A. Sowa. Interpreting Mean Drop Diameters Using Distribution Moments. *Atomization and Sprays*, 2(1):1–15, 1992.
- [34] M. Venegas, P. Rodriguez, A. Lecuona, and M. Izquierdo. Spray absorbers in absorption systems using lithium nitrate ammonia solution. *International Journal of Refrigeration*, 28(4):554–564, June 2005.

- [35] Brian Wallheimer. Pesticide additives cause drifting droplets, but can be controlled <http://phys.org/news/2012-03-pesticide-additives-drifting-droplets.html> Last change: 20 March 2012. Download: 26 April 2016.
- [36] F.S.K. Warnakulasuriya and W.M. Worek. Adiabatic water absorption properties of an aqueous absorbent at very low pressures in a spray absorber. *International Journal of Heat and Mass Transfer*, 49(9-10):1592–1602, May 2006.
- [37] Holger Watter. *Regenerative Energiesysteme*. Springer Fachmedien Wiesbaden, Wiesbaden, 2015.
- [38] Guenter Wozniak. *Zerstaeubungstechnik: Prinzipien, Verfahren, Geraete*. VDI-Buch. Springer, Berlin, 2003.
- [39] Kai Yan, Milind A. Jog, and Zhi Ning. Nonlinear spatial instability of an annular swirling viscous liquid sheet. *Acta Mechanica*, 224(12):3071–3090, December 2013.
- [40] Kai Yan, Zhi Ning, Ming Lu, and Chunhua Sun. Study on Droplet Size and Velocity Distributions of a Pressure Swirl Atomizer Based on the Maximum Entropy Formalism. *Entropy*, 17(2):580–593, January 2015.

Acknowledgements

I would like to express my sincere gratitude to my supervisors, Prof. Dr. Alfred Kersch and Mustafa Yusufi for their patience in explaining many complex interrelations to me, and for their continuous interest, support and guidance during this study. I also like to thank Prof. Dr-Ing. Datong Wu for providing valuable information about his research on absorber heat pumps at Bosch. Thanks also to Christopher Künne for his help in Linux matters, to Waleri Eberhardt for his support on mesh generation and to all the post- and graduate- and undergraduate students in the laboratory for modeling and simulation for the pleasant atmosphere (in spite of the shortage of space). Furthermore, I owe a debt of gratitude to Vera Theilmann for proofreading this work. Last but not least I would like to thank my wife and my kids for allowing me so much time for writing this thesis.

Name: Thomas Kerschl
geb.: 14.07.1972
Matr. Nr.: 12482713
06 MNT im WS 2016/2017

Erklärung

gemäß § 13 Abs. 5 RaPO

Hiermit erkläre ich gemäß der Rahmenprüfungsordnung der Hochschule München, dass ich die vorliegende Arbeit mit dem Titel "Simulation Based Optimization Of Spray Absorption Process Parameters Using OpenFOAM" selbständig verfasst, noch nicht anderweitig für Prüfungszwecke vorgelegt, keine anderen als die angegebenen Quellen oder Hilfsmittel benutzt sowie wörtliche und sinngemäße Zitate als solche gekennzeichnet habe.

Ort, Datum

Unterschrift